SANDIA REPORT
SAND2020-13876
Printed September 2020

Sandia National Laboratories

Developing inductively driven diagnostic X-ray sources to enable transformative radiography and diffraction capabilities on Z

Clayton E. Myers, Matthew R. Gomez, Derek C. Lamppa, Timothy J. Webb, David A. Yager-Elorriaga, Brian T. Hutsel, Christopher A. Jennings, Patrick F. Knapp, Michael Kossow, Larry M. Lucero, Robert J. Obregon, Adam M. Steiner, David J. Ampleford, and Daniel B. Sinars

Prepared by
Sandia National Laboratories
Albuquerque, New Mexico 87185
Livermore, California 94550

Issued by Sandia National Laboratories, operated for the United States Department of Energy by National Technology & Engineering Solutions of Sandia, LLC.

Available to DOE and DOE contractors from

U.S. Department of Energy
Office of Scientific and Technical Information
P.O. Box 62
Oak Ridge, TN 37831

Telephone: (865) 576-8401
Facsimile: (865) 576-5728
E-Mail: reports@osti.gov
Online ordering: http://www.osti.gov/scitech

Available to the public from

U.S. Department of Commerce
National Technical Information Service
5301 Shawnee Road
Alexandria, VA 22312

Telephone: (800) 553-6847
Facsimile: (703) 605-6900
E-Mail: orders@ntis.gov
Online order: https://classic.ntis.gov/help/order-methods

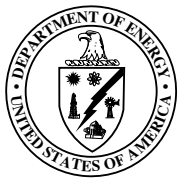

ABSTRACT

Penetrating X-rays are one of the most effective tools for diagnosing high energy density experiments, whether through radiographic imaging or X-ray diffraction. To expand the X-ray diagnostic capabilities at the 26-MA Z Pulsed Power Facility, we have developed a new diagnostic X-ray source called the inductively driven X-pinch (IDXP). This X-ray source is powered by a miniature transmission line that is inductively coupled to fringe magnetic fields in the final power feed. The transmission line redirects a small amount of Z's magnetic energy into a secondary cavity where 150+ kA of current is delivered to a hybrid X-pinch. In this report, we describe the multi-stage development of the IDXP concept through experiments both on Z and in a surrogate setup on the 1 MA Mykonos facility. Initial short-circuit experiments to verify power flow on Z are followed by short-circuit and X-ray source development experiments on Mykonos. The creation of a radiography-quality X-pinch hot spot is verified through a combination of X-ray diode traces, laser shadowgraphy, and source radiography. The success of the IDXP experiments on Mykonos has resulted in the design and fabrication of an IDXP for an upcoming Z experiment that will be the first-ever X-pinch fielded on Z.

We have also pursued the development of two additional technologies. First, the extended convolute post (XCP) has been developed as an alternate method for powering diagnostic X-pinches on Z. This concept, which directly couples the current flowing in one of the twelve Z convolute posts to an X-pinch, greatly increases the amount of available current relative to an IDXP (900 kA versus 150 kA). Initial short-circuit XCP experiments have demonstrated the efficacy of power flow in this geometry. The second technology pursued here is the inductively driven transmission line (IDTL) current monitor. These low-current IDTLs seek to measure the current in the final power feed with high fidelity. After three generations of development, IDTL current monitors frequently return cleaner current measurements than the standard B-dot sensors that are fielded on Z. This is especially true on high-inductance experiments where the harshest conditions are created in the final power feed.

ACKNOWLEDGMENT

The authors thank the numerous Z Principal Experimenters who have fielded inductively driven transmission lines (IDTLs) on their experiments over the past three years. We would also like to thank the Mykonos technologist staff for ensuring that the machine was running smoothly throughout our campaigns. We thank Tom Awe for the use of his electro-thermal instability Mykonos platform as a test bed for the initial scoping of hybrid X-pinches on Mykonos. We thank Hannah Hasson and Maren Hatch for their contributions to the Mykonos shadowgraphy system, and we also thank Hannah for her contributions to B-dot signal processing. We thank Jim Moore, Trevor Hutchinson, and Gabe Shipley for experimental assistance at Mykonos. Finally, we thank the Laboratory Directed Research & Development (LDRD) program at Sandia National Laboratories for supporting this work.

CONTENTS

NOMENCLATURE

Abbreviation	Definition
A-K	Anode-Cathode
ASAP	Assured Survivability and Agility for Pulsed Power
AWG	American Wire Gauge
COBRA	Cornell Beam Research Accelerator
COTS	Commercial Off-The-Shelf
CVR	Current Viewing Resistor
DMP	Dynamic Materials Program
ESF	Edge Spread Function
ETI	Electro-Thermal Instability
FWHM	Full-Width, Half-Maximum
HED	High Energy Density
ICF	Inertial Confinement Fusion
IDTL	Inductively Driven Transmission Line
IDXP	Inductively Driven X-Pinch
LDRD	Laboratory Directed Research & Development
lp/mm	Line pairs per millimeter
LSF	Line Spread Function
LTD	Linear Transformer Driver
MagLIF	Magnetized Liner Inertial Fusion
MITL	Magnetically Insulated Transmission Line
MTS	Midwest Tungsten Service
PCD	Photoconducting Diode
SDD	Source-Detector Distance
SiD	Silicon Diode
SOD	Source-Object Distance
TRL	Technology Readiness Level
USAF	United States Air Force
XCP	Extended Convolute Post
ZBL	Z Beamlet Laser

1. INTRODUCTION

Diagnostic X-ray sources constitute a powerful tool for probing the high energy density (HED) conditions that are routinely created on the Z Pulsed Power Facility. Their applications span two of the major science programs on Z: inertial confinement fusion (ICF) and dynamic materials properties (DMP). Diagnostic X-ray sources provide radiography capabilities to the ICF program and X-ray diffraction capabilities to the DMP program. At present, the Z-beamlet laser (ZBL) is used to generate line-emission X-ray sources in the 1.8–7.2 keV range [Sinars et al., 2004, Schollmeier et al., 2017]. As shown in Figure 1-1, these laser-generated sources are routinely used in a spherically bent crystal imaging configuration to backlight liner implosions and other HED experiments. The resulting monochromatic radiographs have been used, for example, to identify the formation of a helical instability in magnetized liner implosions [Awe et al., 2013] and to assess the hydrodynamic confinement time of liquid-filled liners [Knapp et al., 2017]. More recently, ZBL-generated X-ray sources have also been used to probe the structure of compressed materials via spherical crystal X-ray diffraction [Ao et al., 2020].

While the laser-driven X-ray sources used on Z have become a workhorse HED diagnostic, they have several key limitations. First, the ZBL backlighter system is limited to a maximum of two

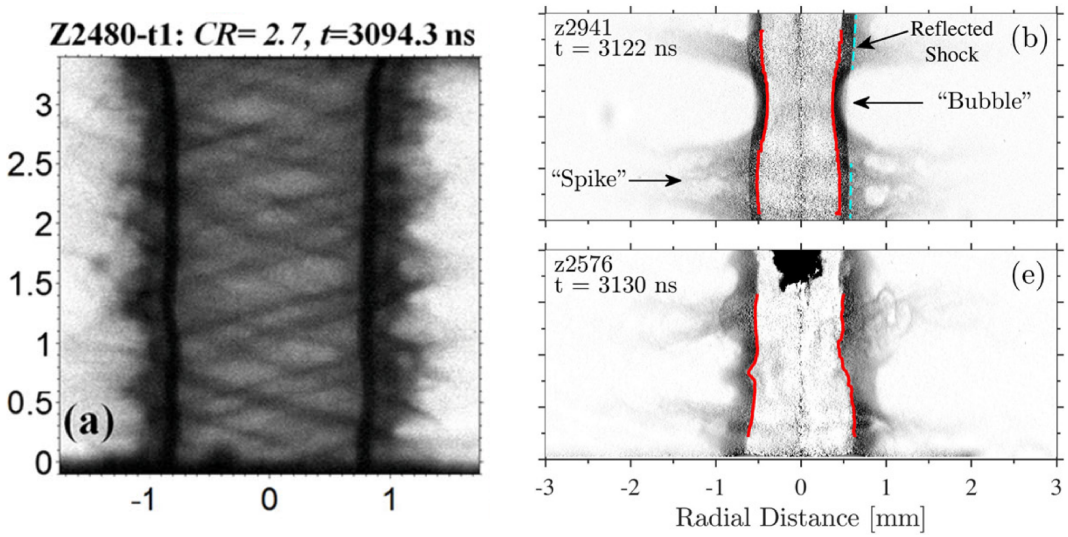

Figure 1-1. *Monochromatic radiographic images obtained with laser-generated diagnostic X-ray sources on Z. The radiograph on the left is used to identify the formation of helical instability in magnetized liner implosions (Adapted from Awe et al. [2013] with the permission of the American Physical Society). The radiograph on the right is used to assess the hydrodynamic confinement time of liquid-filled liners (Adapted from Knapp et al. [2017] with the permission of AIP Publishing).*

radiographic frames per shot. Second, ZBL-based radiography is altogether unavailable when the ZBL laser is being used for other purposes (namely to preheat the fusion fuel in Magnetized Liner Inertial Fusion experiments [Gomez et al., 2014]) or when its optical path is obstructed by other diagnostics. The MagLIF case is particularly impactful because it means that no radiograph has ever been taken of the liner implosion on an integrated (neutron-producing) MagLIF experiment. Given the various limitations on ZBL-generated X-ray sources, additional diagnostic X-ray sources for radiography and diffraction would be of great utility for Z experiments.

A well-known alternative to the laser-driven X-ray source is a pulsed-power-driven source called an X-pinch [Zakharov et al., 1982, Pikuz et al., 1994, Shelkovenko et al., 1999, Sinars et al., 2001, 2003, Beg et al., 2003, Sinars et al., 2008, 2012, Collins et al., 2014, Pikuz et al., 2015a,b]. X-pinches generate an ultra-short, highly compact burst of X-rays that has long been recognized as a powerful radiography tool [Kalantar and Hammer, 1993, Pikuz et al., 1997, Lebedev et al., 2001, Beg et al., 2006, Shelkovenko et al., 2016a]. Figure 1-2 shows the two most prominent X-pinch geometries. The first is the multi-wire X-pinch where two or more fine wires are crossed in an X configuration between two widely separated electrodes. The X-pinch is typically driven with a 100+ kA current pulse that rises in 100 ns or less. This is due to an empirically established X-pinch rate-of-rise drive condition of 1 kA/ns [Shelkovenko et al., 2006]. The X-pinch geometry concentrates current and magnetic field at the wire X point, creating strong pinch conditions that lead to the formation of an X-ray-generating hot spot. For a given current pulse, the timing of the X-ray burst can be controlled by changing the amount of mass at the wire X point. Figure 1-2 also shows that a mini-diode is often formed after the initial X-ray burst as the wire mass is ejected from the pinch point. This mini-diode creates a secondary X-ray source that is broader and harder than the original hot spot.

The second X-pinch geometry shown in Figure 1-2 is that of a hybrid X-pinch, which mocks up the multi-wire X-pinch geometry using conical electrodes rather than discrete wires [Shelkovenko et al., 2010]. The gap between the conical electrodes is spanned by a single fine wire that is pinched by the current and magnetic field concentrated in the A-K gap. The hybrid configuration has two advantages over the multi-wire geometry: (1) it is easier to assemble since it only contains one fine wire; and (2) it tends to generate a less aggressive mini-diode due to the large mass of the conical electrodes. That being said, hybrid X-pinches can be optimized to generate hard X-rays in addition to the traditional X-pinch hot spot [Shelkovenko et al., 2016b].

The X-ray spectrum that is generated from an X-pinch hot spot is a function both of the wire material and of the available driver energy. Figure 1-3 shows spectra for typical few-100 kA-scale titanium and molybdenum X-pinches. The Ti pinch produces both continuum and line emission, while the Mo pinch produces a 3–8 keV continuum of X-rays. Figure 1-4 shows how Mo X-pinches have been used to great effect on the 1 MA COBRA facility at Cornell University to obtain a radiographic time sequence of the ablation of material from a tungsten wire array Z-pinch [Douglass and Hammer, 2008]. A similar Mo X-pinch source could provide Z experiments with a ZBL-independent radiography capability or with a Laue (continuum) diffraction capability [Suggit et al., 2010], both of which would greatly expand our HED diagnostic suite.

Despite their substantial promise, diagnostic X-pinches have never been fielded on Z. The primary reason is that the typical X-pinch backlighter configuration that is used on 1 MA facilities where the X-pinches are fielded in a return current post cannot be used on Z. This is due to the

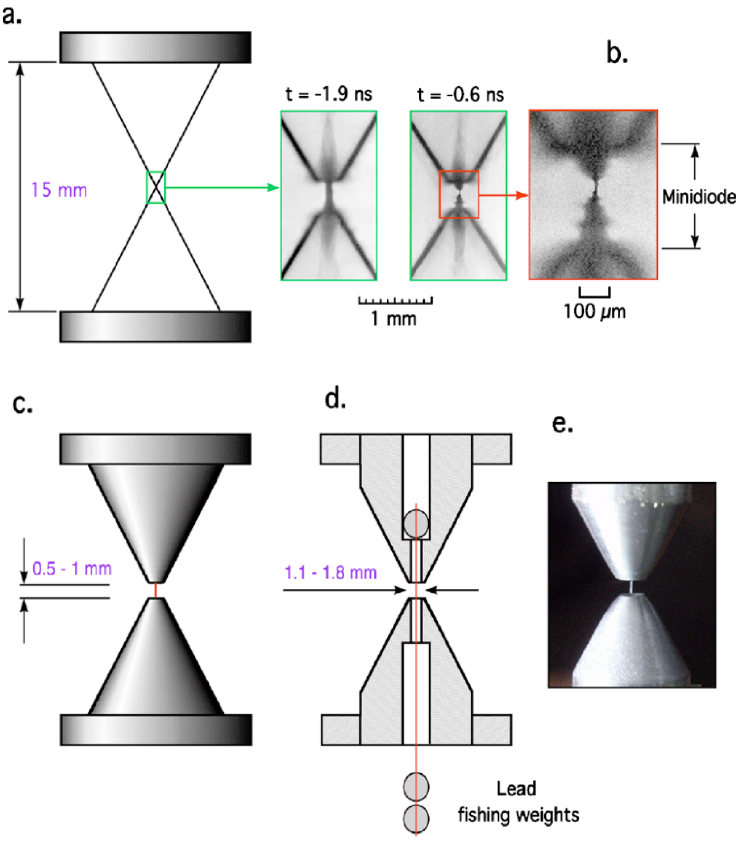

Figure 1-2. *Two common X-pinch geometries: the multi-wire X-pinch (top) and the hybrid X-pinch (bottom). Reproduced from Shelkovenko et al. [2010] with the permission of AIP Publishing.*

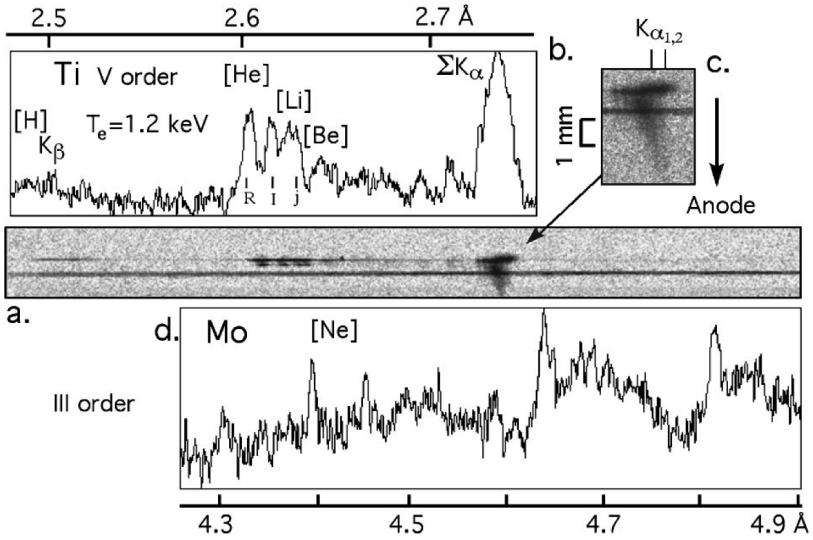

Figure 1-3. *Typical titanium and molybdenum X-pinch spectra. Note that the titanium spectrum is dominated by line emission while the molybdenum spectrum is dominated by continuum emission in the* 3–8 keV *range. Reproduced from Shelkovenko et al. [2001] with the permission of AIP Publishing.*

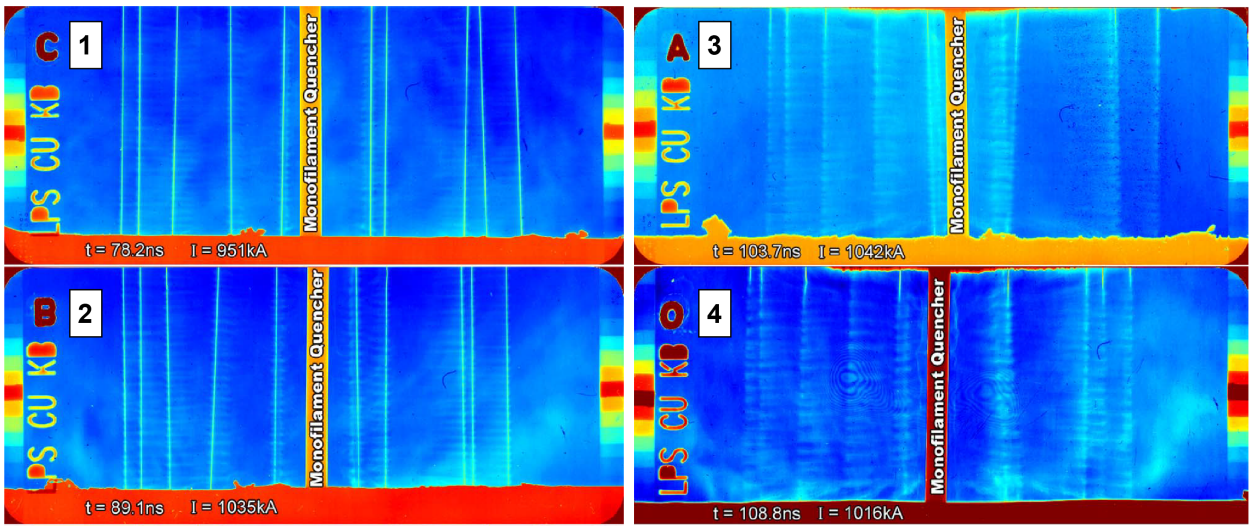

Figure 1-4. *Four-frame sequence of the ablation of material from a tungsten wire array Z-pinch. Each frame is backlit by a different four-wire Mo X-pinch. The timing of each X-pinch is controlled by changing the mass of the Mo wires. Adapted from Douglass and Hammer [2008] with the permission of AIP Publishing.*

fact that the load architecture and impedance constraints on Z are too restrictive to accommodate a return-post X-pinch. In this project, we investigate a new idea for non-perturbatively coupling a small amount of Z's magnetic energy to an X-pinch. This idea, which we call the inductively driven transmission line (IDTL), uses a carefully designed conductor geometry to passively extract energy from the fringe magnetic fields that are present in Z's innermost magnetically insulated transmission line (MITL). If IDTLs can non-perturbatively deliver 100+ kA of current to a secondary, parallel transmission line, they could provide the first-ever diagnostic X-pinch capability on Z.

Figure 1-5 shows a sketch of the inductively driven X-pinch (IDXP) concept on a MagLIF experiment. In this experimental geometry, a conical final feed delivers the Z current to an elevated load region that is sketched in blue. The top anode on each Z experiment typically contains several azimuthally localized B-dot cavities that are used to measure the magnetic field and therefore the current in the inner MITL (see the left side of Figure 1-5). To accommodate an IDXP, the B-dot cavity is elongated into a slot as shown on the right side of Figure 1-5. The IDXP itself contains a 'drive loop' that protrudes into the slotted cavity in the anode where it accesses Z's fringe magnetic fields. These fringe fields increase rapidly in amplitude as the Z current ramps to $\sim$20 MA in $\sim$100 ns. With this massive swing in magnetic flux, 100+ kA of current is induced on the IDXP drive loop. Since the IDXP only samples the fringe fields, the hypothesis is that it will not interfere with the power flow to the primary experimental load. The ultimate goal is to couple this induced current to an X-pinch load that sits atop the IDXP housing.

During this project, we have developed the IDXP concept using a combination of ride-along experiments on Z and dedicated Z-surrogate experiments on the 1 MA Mykonos facility [Mazarakis et al., 2010]. The dedicated Mykonos experiments allowed us to accelerate the IDXP timeline substantially relative to the progress that could have been made using only Z ride-along

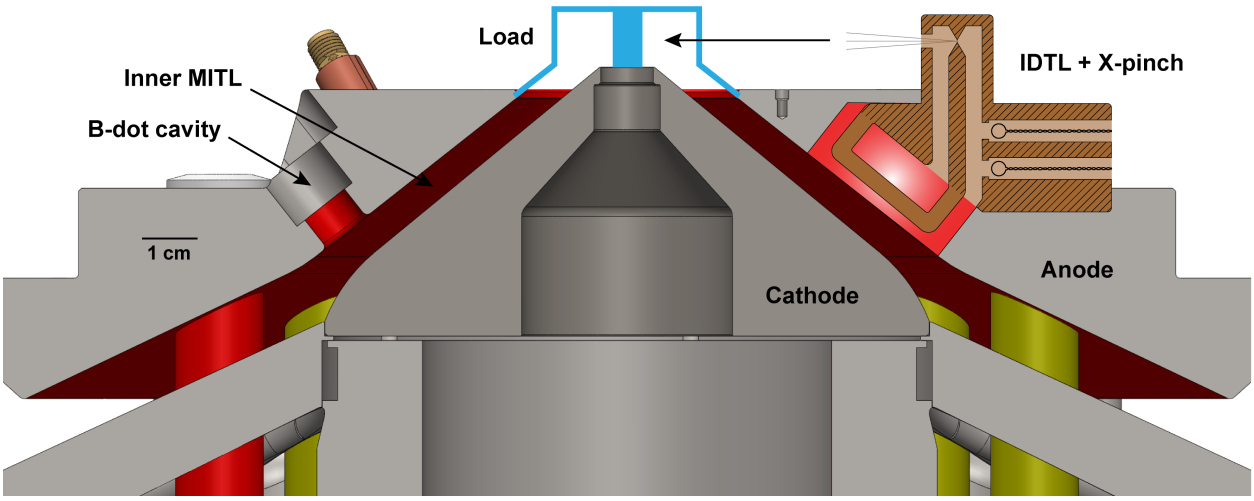

Figure 1-5. *A typical load hardware assembly on the Z accelerator (based on MagLIF Integration 18b). The top anode is separated from the cathode by an A-K gap that forms the inner magnetically insulated transmission line (MITL). The nominally azimuthally symmetric inner MITL delivers* ∼20 MA *of current in* ∼100 ns *to an axisymmetric load, which is depicted here in blue. A cylindrical B-dot cavity (left) is cut into the top anode to facilitate magnetic measurements of the current flowing in the inner MITL. To allow for the extraction of* 100+ kA *of current from the inner MITL, we expand these* ∼1 cm *cylindrical B-dot cavities into* ∼3 cm *slots (right), which increases the accessible magnetic energy in the cavity. The slotted cavity provides enough flux to drive an inductively drive X-pinch (IDXP, top right). The X-pinch resides in a periscope at the top of the IDTL so that is has a direct line-of-sight to the Z load.*

experiments. To determine whether inductively driven X-pinches are a viable concept, four key questions need to be answered:

1. Can 100+ kA of current be reproducibly driven in short-circuit IDTLs on Z without perturbing the power flow to the primary experiment? The IDXP concept is only viable if it operates non-perturbatively.
2. Can the same 100+ kA of current be driven in Z-surrogate short-circuit IDTLs on Mykonos? Experimental opportunities on Z are limited and the development cycle is long (∼6 months), so it is crucial to establish a surrogate offline testing capability that offers more rapid turn around.
3. Can the Z-surrogate IDTLs on Mykonos drive X-pinches that generate radiography-quality X-ray bursts? This is *the* key question for the IDXP concept given that the IDTL is a unique, low-impedance driver that we are attempting to couple to an X-pinch.
4. Are IDXP sources sufficiently reproducible and do they generate enough X-ray fluence to achieve acceptable signal-to-noise on Z?

Over the course of this project we successfully addressed each of the first three questions. To answer Question 1, Chapter 2 presents a series of Z experiments that demonstrate that 200+ kA of current can be driven in a short-circuit IDTL without perturbing the primary load. Then, to answer Question 2, Chapter 3 presents the design and implementation of a Z-surrogate IDTL platform for Mykonos as well as short-circuit IDTL experimental results that demonstrate the

successful coupling of $\sim$150 kA of IDTL current on Mykonos. Next, to answer Question 3, Chapter 4 presents the development and successful demonstration of radiography-quality IDXPs on Mykonos. Finally, we also present the design of an IDXP for Z that will begin to test various aspects of Question 4 (see Chapter 7). This IDXP has been fully designed and fabricated and will be fielded in the near future. Overall, this project succeeded in its primary objective of substantially advancing the technical readiness of the inductively driven X-pinch concept. More specifically, we believe that we have advanced the IDXP technology readiness level (TRL) [Mitchell, 2007] from TRL 2 (concept formulated) to TRL 4 (key elements demonstrated in laboratory environment).

In addition to the IDXP concept, we also pursued the development two additional technologies during this project. The first is the extended convolute post (XCP) concept, which is an alternate pathway to fielding diagnostic X-pinches on Z. Unlike the IDXP, which is driven in parallel with the primary load, the XCP is driven in series with one of the twelve convolute posts in the Z double post-hole convolute [Pointon, 2008]. This means that the XCP can deliver up to 1 MA of current to an X-pinch load (nearly 10 times that of IDXPs), which greatly increases the possibilities for how the X-pinch is fielded. We have successfully demonstrated current coupling to a prototype short-circuit XCP (see Chapter 5), so the technology readiness has been advanced from TRL 0 (idea) to TRL 3 (concepts demonstrated analytically or experimentally).

The second additional technology pursued during this project is the IDTL current monitor. Here we use lower-current IDTLs than those developed for the IDXP to measure the Z inner-MITL current with high fidelity. While this development work began under a previous project [Myers et al., 2018], we iterated and refined the IDTL current monitor design during this project. We have converged on a streamlined design that is now being tested across a wide range of Z experiments (see Chapter 6). As such, the technology readiness of the IDTL current monitor has been advanced from TRL 4 (key elements demonstrated in laboratory environment) to TRL 5 (key elements demonstrated in relevant environments).

2. SHORT-CIRCUIT INDUCTIVELY DRIVEN TRANSMISSION LINE EXPERIMENTS ON Z

Short-circuit inductively driven transmission line (IDTL) experiments are a key stepping stone in the development of inductively driven X-pinches (IDXPs). Short-circuit experiments demonstrate that the hundreds of kiloamperes of current that are required to drive an X-pinch can be coupled to an IDTL without incurring catastrophic current loss in the IDTL or in the primary experiment. If short-circuit IDTLs cannot operate non-perturbatively, then the IDXP concept would not be viable. In this chapter we present the design of high-current, short-circuit IDTLs for Z. We then present the results from ride-along experiments on Z which show that the non-perturbative coupling of 200+ kA of current to the IDTLs is achieved.

2.1. SHORT-CIRCUIT IDTL DESIGN

The IDTL is a single-turn transformer that is coupled to the large magnetic fields that are present in the final feeds of 100 ns pulsed power generators. The single-turn winding of the IDTL, which we refer to as the drive loop, extracts a small amount of magnetic energy from the final feed and couples it into a coaxial transmission line that is embedded in the body of the IDTL. This coaxial transmission line functions as an inductively isolated secondary path to ground through which hundreds of kiloamperes of current can be driven. If this amount of current can be coupled through the IDTL without incurring catastrophic current loss in the primary experiment or in the IDTL, then IDTLs can be used to drive diagnostic X-ray sources such as X-pinches in parallel with the primary load.

The general characteristics of the high-current or 'slotted' IDTLs fielded on Z are shown in Figure 2-1. A copper IDTL body mounts to a $\sim$3 cm-long custom slot in the top anode of the final feed or inner MITL (magnetically insulated transmission line). This anode slot is located only a few centimeters radially outward from the load region. Inside the IDTL body, a 2.9 mm diameter (AWG #9) copper drive loop runs the length of a vertical cavity forming a coaxial transmission line. The lower portion of the drive loop protrudes into the anode slot, loops around, and terminates on the other end of the IDTL body. This geometry links the drive loop to the fringe magnetic flux that is generated in the anode slot by the primary Z current. As noted in Figure 2-1, the minimum A-K gap in the vertical transmission line of this IDTL is 3 mm and the standoff between the bottom of the drive loop and the power flow in the inner MITL is 2 mm (i.e., the drive

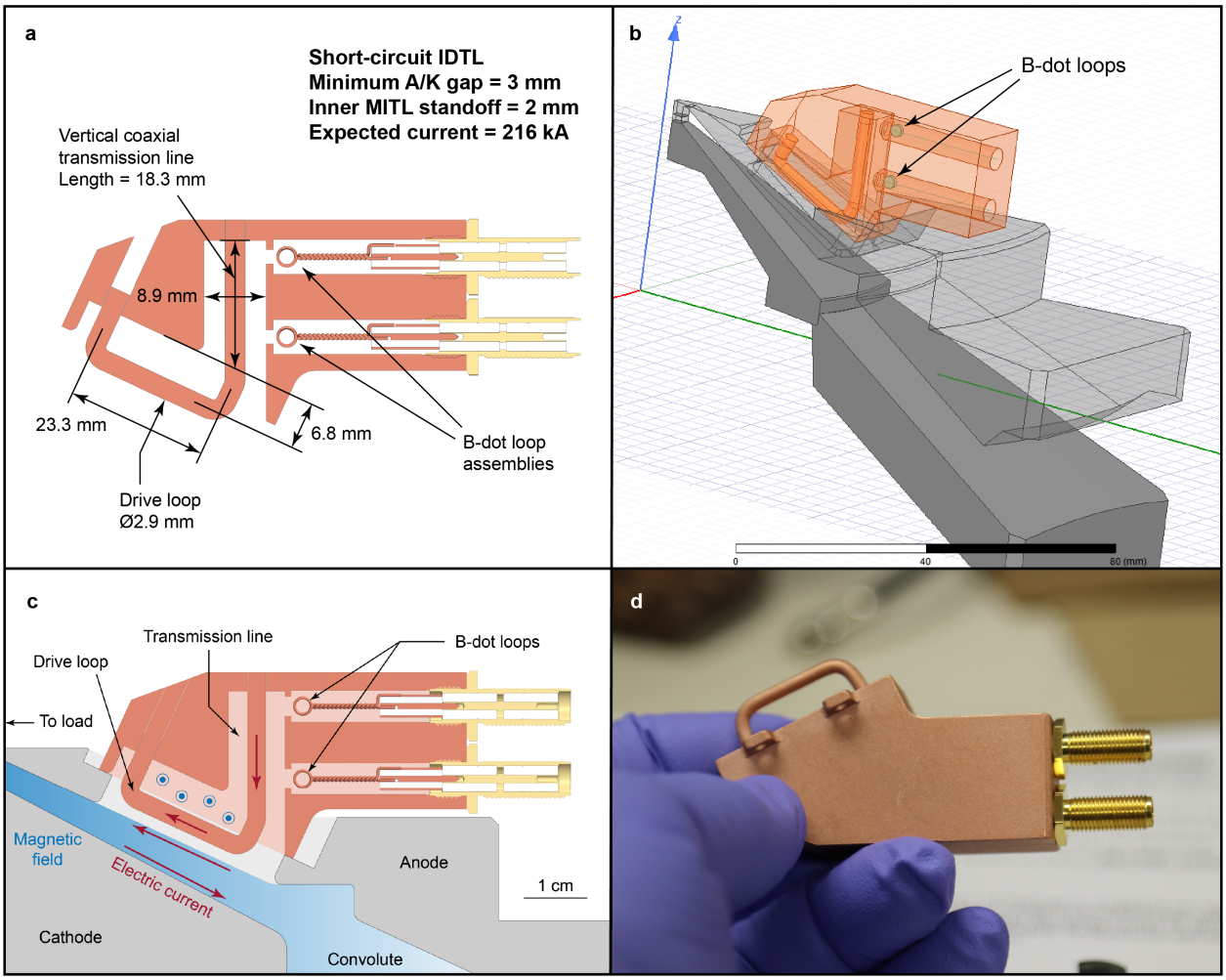

Figure 2-1. *Short-circuit IDTL design, modeling, and fabrication. (a) Schematic of the IDTL showing the IDTL body, the drive loop, the embedded vertical coaxial transmission line, and the two B-dot loop assemblies. (b)* ANSYS MAXWELL *visualization of the IDTL mounted to the A-K hardware. This model is used to calculate both the current that is expected to be driven in the IDTL (*$\sim$*216* kA*) and the voltages that are expected to be generated on the two B-doot sensor loops (*$\sim$*20* V *for* 20 MA *of primary current on Z). (c) Schematic showing the proximity of the IDTL drive loop to the inner-MITL power flow. (d) Image of a fully fabricated high-current IDTL.*

loop is recessed 2 mm back into the anode slot). The IDTL body also houses two B-dot loop assemblies that are used to measure the magnetic fields generated in the vertical transmission line portion of the IDTL. The two B-dot loop assemblies are fielded in opposite polarity to facilitate common mode rejection of cable drive that is often present on Z.

A key aspect of IDTL operation on 100 ns generators is that the currents that are driven in the IDTL are nearly in-phase with the primary generator current. This means that the IDTLs are operating close to the perfectly conducting limit where $\omega\tau \gg 1$. Here, $\omega = 2\pi f$ is the angular drive frequency and $\tau = L/R$ is the resistive decay time of the IDTL currents. On a 100 ns generator, the fundamental drive frequency is $f = 2.5$ MHz. For the slotted IDTL design shown in Figure 2-1, the calculated self inductance is $L \simeq 12.8$ nH. Assuming that the IDTL current travels

within the skin depth of the surface of the copper, the approximate total resistance of the IDTL is $L \simeq 3.3\,\mathrm{m}\Omega$, which gives $\tau \simeq 3.9\,\mu\mathrm{s}$ and $\omega\tau \simeq 61 \gg 1$. At these parameters, the phase of the IDTL current differs from the generator current by less than 1 ns.

A fundamental question for any IDTL design is how much current is induced on the drive loop. Unfortunately, this quantity cannot be easily measured experimentally. This is because, while the IDTL B-dot signals are dominated by the magnetic fields that are generated by the IDTL, the IDTL fields are in-phase with the primary fields generated by Z. The standard B-dot calibration process is therefore unable to distinguish between the secondary IDTL-generated fields and the primary Z-generated fields. In order to assess the current driven in the IDTL, we must therefore rely on 3D electromagnetic modeling of the IDTL and the Z inner MITL.

Figure 2-1b shows an ANSYS MAXWELL visualization of $1/12^{\mathrm{th}}$ of the Z A-K hardware with a high-current IDTL mounted to the top anode. The system is excited at a fundamental drive frequency of 2.5 MHz (100 ns quarter wave) to determine the expected IDTL current and B-dot loop voltages given 20 MA of input current. For this IDTL design, the simulations expect $\sim$216 kA of induced current and B-dot voltages of $\sim$20 V. This 200+ kA of IDTL current is more than enough to meet the standard $\sim$1 kA/ns X-pinch drive requirement [Shelkovenko et al., 2006]. Additionally, as we will show in the next section, the predicted B-dot voltages can be compared to the voltages recorded during bench calibrations in order to instill confidence in the numerical modeling of the IDTL currents.

2.2. SHORT-CIRCUIT IDTL EXPERIMENTAL RESULTS

Prior to being fielded on Z, the various B-dot sensors mounted to the top anode are calibrated using a 10 kA, 100 ns tabletop pulser. This procedure is designed to replicate the magnetic field topology that is generated on Z at a non-destructive $1/2000^{\mathrm{th}}$ scale (10 kA vs. 20 MA). Signals at the 10 mV level are generated on each B-dot sensor, providing sufficient information to calibrate the B-dots with respect to a known current flowing through the inner MITL. This current is monitored using an absolutely calibrated current-viewing resistor (CVR).

Figure 2-2 shows the signals generated during the calibration of two high-current IDTLs. The top panel shows the average inner-MITL calibration current as measured by the CVR. The bottom panel compares the ANSYS MAXWELL prediction to the voltages measured on the IDTL B-dot sensors during calibration. The predicted voltage waveform is obtained by combining the results of the ANSYS MAXWELL IDTL simulations with the derivative of the CVR current. Note that the B-dot voltages have each been scaled to 20 MA on Z. From this comparison we see that the measured and predicted voltages agree to better than 25%. Given the spatial tolerances of the drive loops and the B-dot loop assemblies, this qualifies as good agreement between modeling and calibration. As such, we have confidence in the accuracy of the 200+ kA prediction for the IDTL currents. More details on the B-dot calibration procedure and the comparison to ANSYS MAXWELL modeling are available in Myers et al. [2018].

With the raw B-dot calibration data in hand, the remaining task is to determine how to integrate the raw B-dot signals to obtain a measurement of the inner MITL current. Once this is known, we

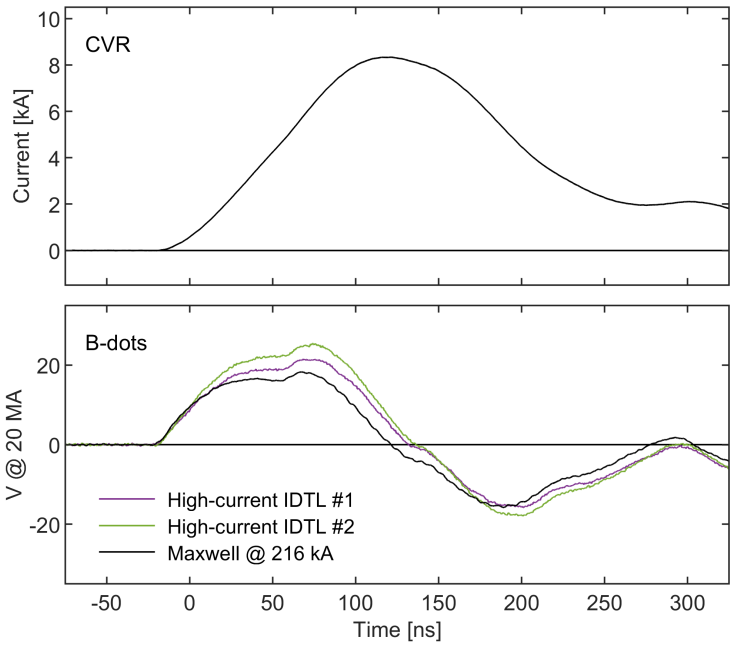

Figure 2-2. *Comparison of short-circuit IDTL calibration data to predictions from* ANSYS MAXWELL *modeling. Top: Inner-MITL (magnetically insulated transmission line) calibration current as measured by a current-viewing resistor (CVR). Bottom: Comparison of measured B-dot voltages to the modeled B-dot voltage (each scaled to* 20 MA *on Z). Given that the measured and predicted curves agree to better than 25% in a system that is sensitive to as-built variations, we have confidence that full current delivery at* 20 MA *on Z corresponds to* 200+ kA *of current in the IDTL.*

can determine whether good current coupling to the IDTL is achieved at 20 MA on Z. More specifically, if the integrated IDTL B-dots match the Z current pulse as measured by the standard inner-MITL B-dots, then full current coupling to the IDTL is observed. To relate the measured B-dot voltages to the inner-MITL current, we must solve the following differential equation:

$$V_{\mathrm{B}} = -\frac{d\Phi_{\mathrm{Z}}}{dt} = -\frac{d}{dt}\left(M_{\mathrm{Z}} I_{\mathrm{Z}}\right) = -M_{\mathrm{Z}}\frac{dI_{\mathrm{Z}}}{dt} - \frac{dM_{\mathrm{Z}}}{dt} I_{\mathrm{Z}}, \tag{2.1}$$

where V_{B} is the B-dot voltage, Φ_{Z} is the flux coupled to the B-dot, M_{Z} is the mutual inductance between the B-dot and Z, and I_{Z} is the primary Z current. It is well known in 100 ns pulsed power systems that it is necessary to account for a time-varying mutual inductance between the B-dot and the generator $M_{\mathrm{Z}}(t)$. This is because induced currents in conductors near the B-dot loop initially shield the B-dot from the magnetic field. As such, the mutual inductance grows with time. The standard approach to solving Equation 2.1 is to approximate the decay of these induced currents with a characteristic flux penetration time τ_{f} [Wagoner et al., 2008]:

$$V_{\mathrm{B}} \simeq -M_{\mathrm{Z}}\frac{dI_{\mathrm{Z}}}{dt} - \frac{M_{\mathrm{Z}}}{\tau_{\mathrm{f}}} I_{\mathrm{Z}} \tag{2.2}$$

This differential equation has a Green's function solution that can be written as

$$I_{\mathrm{Z}}(t) = \int_{-\infty}^{t} dt' V_{\mathrm{B}}(t')\, g(t-t'), \tag{2.3}$$

where

$$g(t-t') = \frac{e^{-(t-t')/\tau_f}}{M_Z}. \tag{2.4}$$

In practice, a nonlinear fit to the calibration data is performed to determine experimental values for M_Z and τ_f for each B-dot sensor loop. These calibration-derived values are then applied to the voltage signals measured on the actual Z experiment.

Figure 2-3 shows the raw (top) and integrated (bottom) B-dot signals from five similar Z experiments that each fielded IDTLs. The left column shows the results from standard inner-MITL B-dot sensors while the right column shows the results from the IDTL B-dot sensors. The three shots shown in blue fielded a low-current IDTL design that is described in Myers et al. [2018]. The two shots shown in red fielded the high-current slotted IDTLs shown in Figure 2-1. We first note that the raw IDTL B-dot signals are much cleaner than the raw signals from the standard B-dots. This an inherent, desirable feature of IDTL B-dot sensors, which are better protected from the harsh inner-MITL environment (see Chapter 6 for more details). More importantly for the present discussion, the integrated current measured by each of the high-current IDTLs tracks the integrated current from the standard B-dots to better than 10% (see the gray shaded region in Figure 2-3). This indicates that the IDTLs are coupling nearly all of the predicted current. Additionally, the experiments on which the high-current IDTLs were fielded

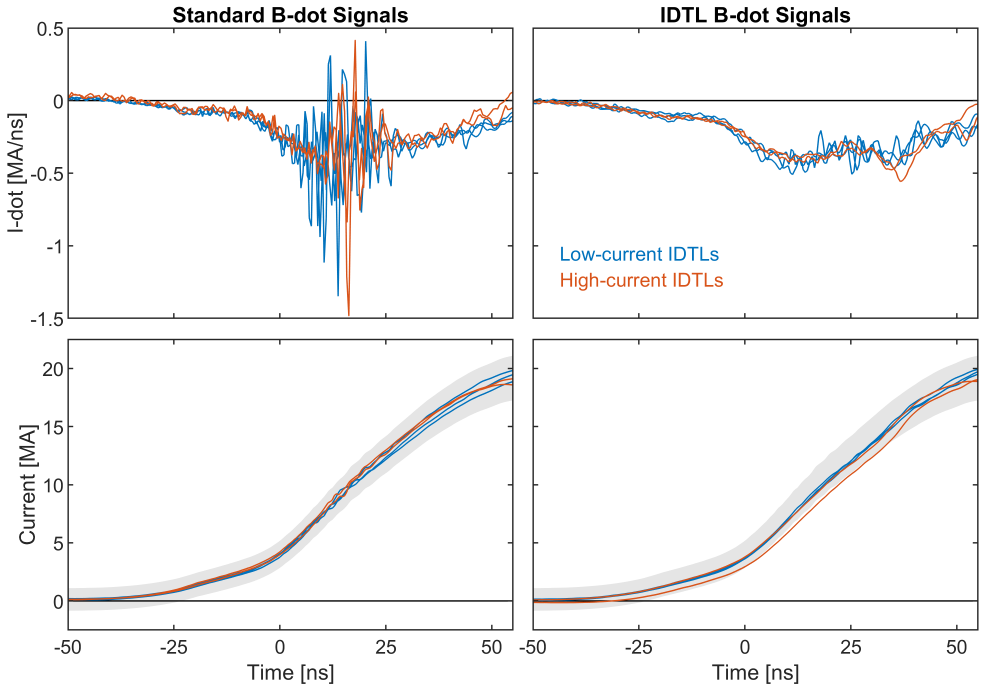

Figure 2-3. *Short-circuit IDTL results from five similar experiments on Z. The left column shows raw signals and integrated currents from standard inner-MITL B-dots, while the left column shows the same signals from the IDTL B-dots. The data in blue is from three experiments that fielded low-current IDTLs, while the data in red is from two experiments that fielded high-current IDTLs. The fact that the IDTL currents match the standard B-dot currents to better than 10% (the gray shaded region) indicates that nearly all of the expected current is coupled to the IDTLs. See the text for further details.*

performed nominally according to both driver-target coupling diagnostics and other metrics. This is a key result in that it demonstrates that we can non-perturbatively generate 200+ kA of IDTL current at 20 MA on Z.

As mentioned at the beginning of this chapter, the minimum A-K gap inside the high-current IDTLs shown in Figure 2-1 is 3 mm. Several Z experiments that fielded high-current IDTLs with smaller minimum A-K gaps (2.3 mm) were inconclusive as to whether the IDTLs were able to couple the desired amount of current. Given this possible evidence that the minimum A-K gap could be an issue, we decided to expand the minimum gap to 3.3 mm for most of the Mykonos IDTL experiments covered in Chapters 3 and 4 and for future high-current IDTL experiments on Z such as the IDXP described in Chapter 7.

We also note that due to long design cycles and rare shot opportunities, the two high-current IDTL shots presented in this section took nearly a year to field from conception to data return. Given that this entire LDRD project was two years in length, year-long turnaround times are prohibitive for developing new diagnostics like the inductively driven X-pinch (IDXP). As such, it was necessary to establish an offline IDXP test bed to speed up the development cycle. For this we turned to the 1 MA Mykonos facility that is located adjacent to Z.

3. SHORT-CIRCUIT INDUCTIVELY DRIVEN TRANSMISSION LINE EXPERIMENTS ON MYKONOS

Following the successful demonstration of the non-perturbative coupling of 200+ kA of current to short-circuit IDTLs on Z, the next step in this project was to develop a surrogate offline IDTL testing capability to enable the rapid exploration of the inductively driven X-pinch (IDXP) concept. The availability of a such an offline testing capability provided us with substantially more testing opportunities than would have been available solely through ride-along experiments on Z.

3.1. A Z-SURROGATE IDTL PLATFORM FOR MYKONOS

The Mykonos LTD [Mazarakis et al., 2010] is a five-cavity linear transformer driver that delivers a nominal 1 MA, 500 kV current pulse to a variety of loads [see, e.g., Hutsel et al., 2015, Hutchinson et al., 2020]. The 10–90% current rise time for physics loads on Mykonos is $\sim$85 ns [Hutchinson et al., 2020], which is well-matched to the short-pulse rise time on Z [Savage et al., 2011]. The central requirement of a Z-surrogate IDTL platform is that it generate spatial and temporal magnetic field profiles that are similar to those experienced by the IDTL when it is recessed in an anode slot on Z. The pulse-shape surrogacy between Mykonos and Z ensures that the temporal magnetic field profiles are well-matched. The question, then, is whether the requisite magnetic field amplitudes and spatial profiles can be generated on Mykonos.

To demonstrate that Mykonos can, in fact, replicate the magnetic field amplitudes and spatial profiles experienced by an IDTL on Z, Figure 3-1 compares the fields generated in an anode slot on the MagLIF low-inductance final feed on Z [Gomez et al., 2020] to the fields generated in the load region of a notional Z-surrogate Mykonos platform. Figure 3-1a shows the placement of the anode slot and IDTL relative to the MagLIF inner MITL (magnetically insulated transmission line). As with the slotted IDTLs introduced in Chapter 2, the IDTL drive loop is 2.9 mm in diameter (AWG #9) and the standoff distance between the anode surface and the bottom of the drive loop is 2 mm. Figure 3-1b shows an *R-Z* cross section of the calculated fringe magnetic fields that are generated in the anode slot at a Z current of 20 MA. This 3D magnetostatic calculation was conducted using ANSYS MAXWELL.

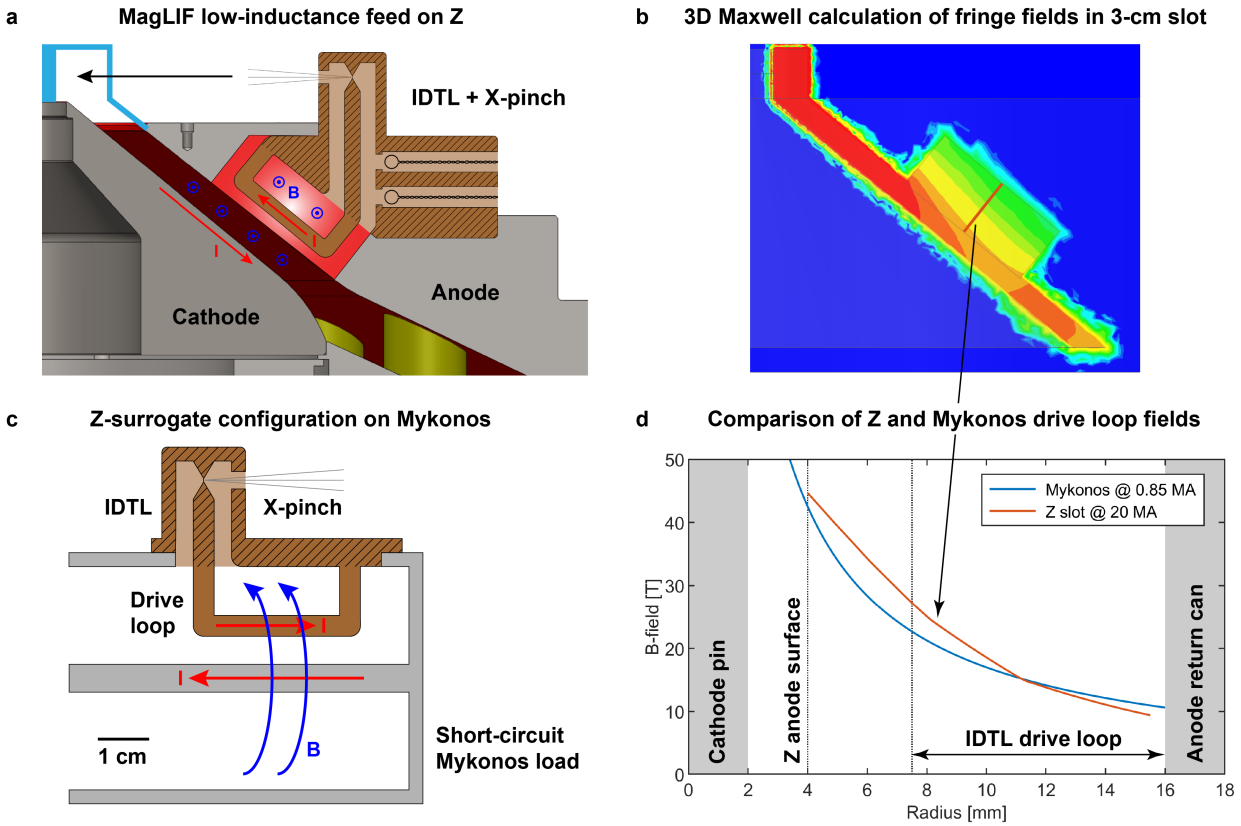

Figure 3-1. *Scoping of a Z-surrogate IDTL configuration on Mykonos. (a) Positioning of the anode slot and IDTL in the MagLIF low-inductance feed on Z. (b) 3D* ANSYS MAXWELL *calculation of the fields generated in the anode slot at* 20 MA *on Z. (c) Load region of a notional Z-surrogate Mykonos IDTL platform. (d) Comparison of the anode slot and Mykonos surrogate magnetic field amplitudes and spatial profiles. See the text for more details.*

Figure 3-1c shows the load region of a notional Z-surrogate Mykonos platform where a 4 mm diameter cathode pin is surrounded by a 32 mm diameter anode return can. The IDTL is mounted to one side of the return can. Instead of being recessed into an anode slot as on Z, however, the IDTL drive loop protrudes into the primary power flow on Mykonos. This is necessary for the 1 MA Mykonos current pulse to be able to replicate the field amplitudes that are generated in an anode slot at 20 MA on Z. In the Mykonos design, the IDTL drive loop is again 2.9 mm in diameter while the standoff distance between bottom of the drive loop and the cathode pin is 4 mm. Finally, Figure 3-1d compares a lineout of the simulated anode-slot fringe fields on Z to the $1/R$ load-region fields on Mykonos. At the expected Mykonos peak current of 0.85 MA, the Mykonos fields are a close match for the fringe fields generated at 20 MA on Z. A more rigorous accounting of the flux coupled to an IDTL on Mykonos as compared to Z can be found in Section 3.2. In summary, if the notional Z-surrogate Mykonos platform shown here delivers full current to the IDTL, it can serve as a suitable proxy for IDTLs on Z.

The laboratory implementation of the Z-surrogate Mykonos IDTL platform is shown in Figure 3-2. The annotated cross-section in Figure 3-2a shows the Mykonos IDTL vacuum chamber and final transmission line geometry from the insulator inward. The transmission line

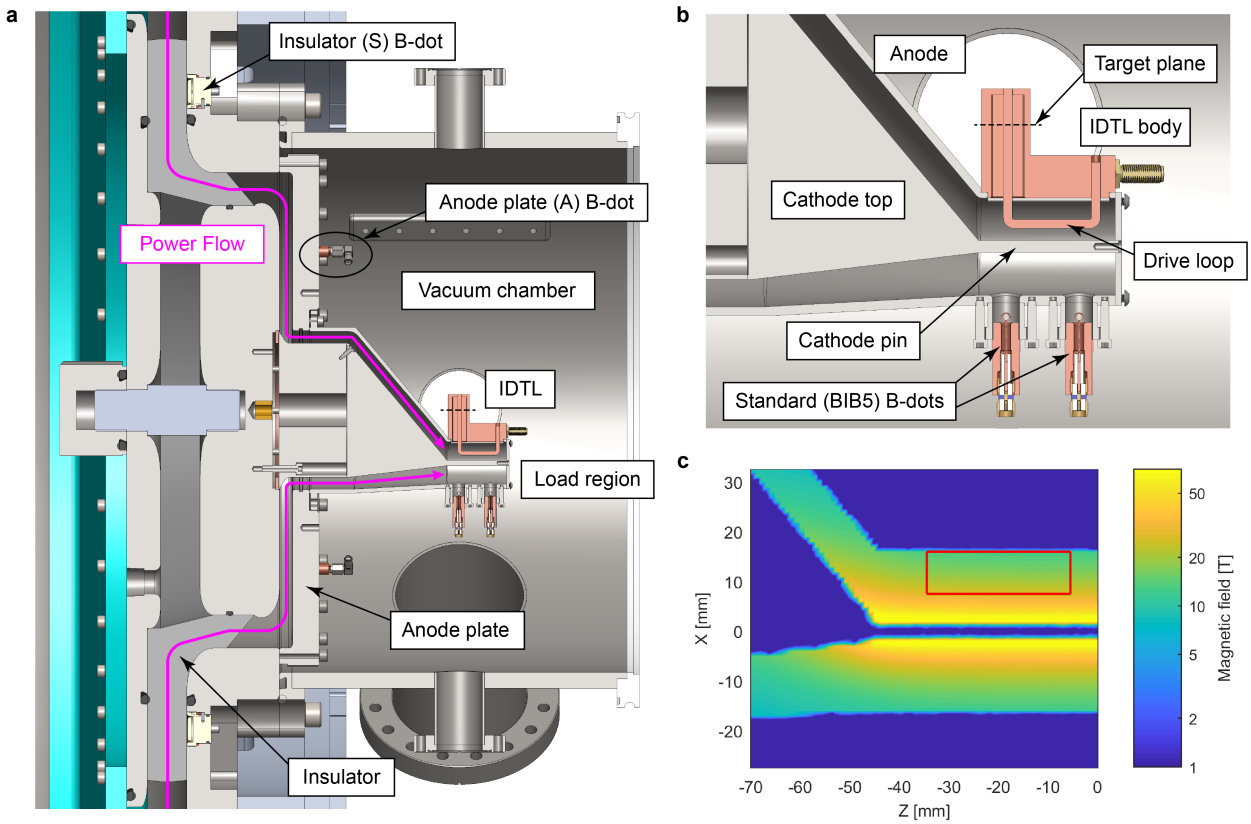

Figure 3-2. *Cross-sections of the Z-surrogate IDTL platform implemented on Mykonos. (a) Annotated cross-section of the Mykonos IDTL vacuum chamber including the final transmission line geometry from the insulator inward. The asymmetric (downward-skewed) conical feed designed for these experiments allows the IDTL target plane to sit at chamber center. (b) Detailed cross-section of the Mykonos IDTL load region. (c) 3D* ANSYS MAXWELL *calculation of the azimuthal magnetic fields in the load region in the absence of an IDTL. These calculations indicate that field symmetry is not an issue despite the downward skew of the final feed. For reference, the IDTL drive loop cross-section is outlined in red.*

configuration used here is standard until it reaches the downward-skewed conical feed just before the load region. This downward-skewed design was developed to allow the target plane of the IDTL (where the X-pinch will eventually be located) to sit at chamber center. This allows for maximum diagnostic access to the X-pinch (see Chapter 4). A detailed cross-section of the Mykonos IDTL load region is shown in Figure 3-2b. The IDTL shown here is a short-circuit IDTL with an extended vertical transmission line that is included to mock up the additional static inductance added by including an X-pinch in the IDTL. As with the short-circuit IDTLs fielded on Z, each Mykonos IDTL contains two B-dot loops that quantify the current coupled to the IDTL. Two standard (BIB5) B-dots are used to diagnose the current delivered to the load region. Finally, Figure 3-2c shows an ANSYS MAXWELL calculation of the azimuthal magnetic field generated in the load region in the absence of an IDTL. The calculations confirm that field symmetry is not an issue despite the downward skew of the final feed.

A total of 32 Mykonos IDTL shots were executed during this project, nine with short-circuit IDTLs similar to one shown in Figure 3-2b and 23 with inductively driven X-pinches (IDXPs).

80 kV test shot	40 kV cal shot	IDTL S/N	IDTL A-K gap	IDTL polarity	Drive loop	Coupling
10367	10366	95	3.3 mm	Negative	Yes	99.6%
10369	10368	100	3.3 mm	Negative	Yes	94.8%
10372	10371	94	2.3 mm	Negative	Yes	98.2%
10374	10373	95	3.3 mm	Negative	Yes	91.8%
10377	10376	100	3.3 mm	Negative	No	—
10379	10378	100	3.3 mm	Negative	Yes	98.2%
10804†	10801	94	2.3 mm	Negative	Yes	88.4%
10845	10844	119	2.3 mm	Positive	Yes	95.3%
10860	10859	119	2.3 mm	Positive	Yes	96.8%

Table 3-1. *Short-circuit IDTL shots on Mykonos. Shot 10377 was null test with no drive loop in the IDTL, and Shot 10804 (marked with a dagger†) experienced an insulator flash that compromised the current delivery to the load region.*

All 32 shots delivered current to the load region. Since nearly 10 kJ of magnetic energy is injected into the load region in ∼100 ns, the cathode pin and the IDTL drive loop are destroyed on each shot. The resulting debris requires that the skewed conical anode and the IDTL body be refurbished by a machinist after each shot. Fortunately they can be reused numerous times.

The nine short-circuit IDTL experiments that were executed on Mykonos are summarized in Table 3-1. The objectives of these experiments were to demonstrate X-pinch-relevant current coupling on the Z-surrogate IDTL platform that is described in Section 3.1 and to explore the effect of parameters such as the IDTL minimum A-K gap and the IDTL current polarity. Three different IDTL designs were fielded during these nine experiments (see Figure 3-3). These designs differ only in their minimum A-K gap and/or their current polarity. As with the high-current IDTLs fielded on Z, it is necessary to conduct electromagnetic modeling of the Mykonos IDTLs to understand the expected current coupling and IDTL B-dot voltages.

3.2. SHORT-CIRCUIT IDTL MODELING

Two of the three IDTL designs shown in Figure 3-3 have been modeled in 3D using ANSYS MAXWELL and ANSYS HFSS. These are the top and middle designs in Figure 3-3, which respectively have 3.3 mm and 2.3 mm minimum A-K gaps. The third design is simply a reversed polarity version of the second design. It should therefore have identical calculated current coupling, but the B-dot signal amplitudes are expected to change because the B-dots had to be moved to the side in this reversed polarity design so that they did not interfere with the downward-skewed Mykonos anode.

The magnetic field calculated from one of the ANSYS HFSS simulations is shown in left half of Figure 3-4. This image shows how the IDTL drive loop depletes the magnetic energy in the load region and extrudes it upward into the coaxial transmission line in the IDTL body. The right half of Figure 3-4 shows a detailed visualization of the IDTL mounted to the Mykonos A-K hardware.

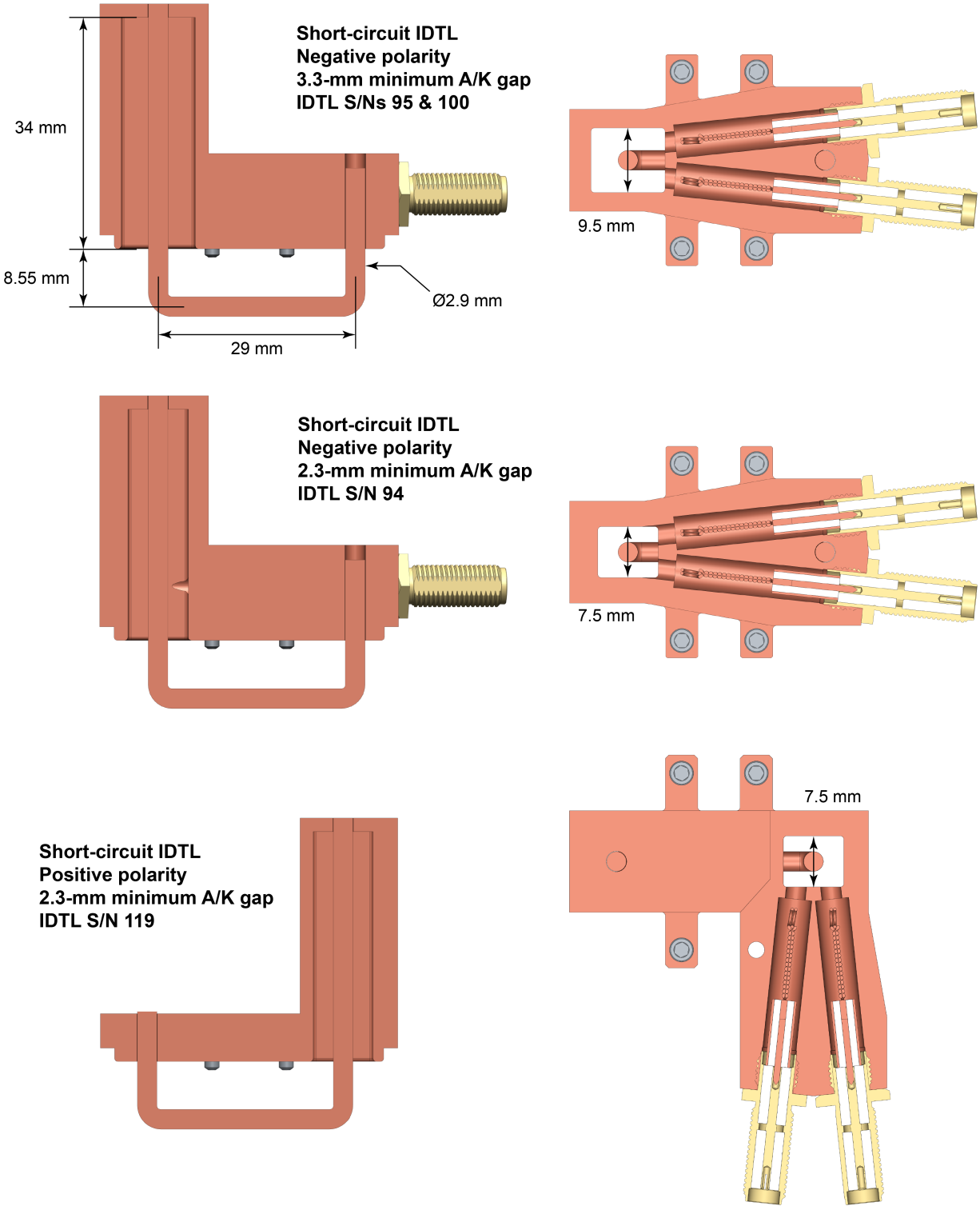

Figure 3-3. *Side and top cross-sections of the three different types of short-circuit IDTLs fielded on Mykonos. In all cases, the downward-skewed Mykonos anode is located to the left of the IDTL. The polarity of the IDTL current is reversed by flipping the IDTL orientation as in the bottom design. This requires moving the B-dots off to the side so that they do not interfere with anode upon rotation.*

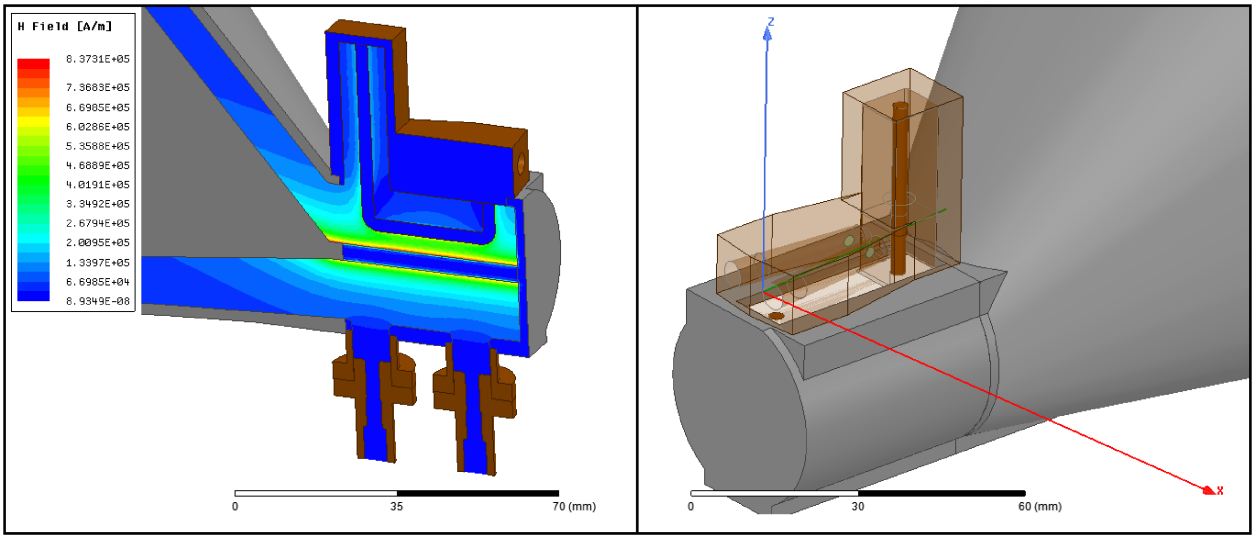

Figure 3-4. *Three-dimensional* ANSYS HFSS *modeling of the magnetic field distribution inside the Mykonos IDTL hardware (left) and at the B-dot locations within the IDTL body (right).*

In this image, the two IDTL B-dot loops are visible inside their respective channels. As we will show, the voltage generated on the B-dots is highly sensitive to their precise depth within these channels (this is the y-direction in the right half of Figure 3-4).

The quantitative results of the ANSYS HFSS modeling of the Mykonos IDTLs are shown in Figures 3-5 and 3-6. First, Figure 3-5 shows that the induced IDTL currents are expected to be $\sim$17.4% of the total Mykonos current. This gives $\sim$150 kA of IDTL current for 850 kA of Mykonos current delivered to the load region, which is meaningfully lower than the 200+ kA that was modeled for the high-current IDTLs on Z. The reasons can be understood by evaluating the various magnetic fluxes in the IDTL. For a perfectly conducting system, the self flux $\Phi_{\mathrm{IDTL}} \equiv L I_{\mathrm{IDTL}}$ will exactly equal the drive flux $\Phi_{\mathrm{drive}} \equiv M I_{\mathrm{drive}}$. Thus, the change in the expected IDTL current from Z to Mykonos is due to some combination of changes to the self inductance and/or the drive flux:

$$I_{\mathrm{IDTL}} = \frac{\Phi_{\mathrm{drive}}}{L} \tag{3.1}$$

For the 216 kA IDTL on Z, the calculated self inductance is 12.8 nH such that the drive flux is 2.8 mWb. On Mykonos, the self inductance of the IDTL rises substantially to 25.9 nH (for the IDTL with a 3.3 mm minimum A-K gap). This increase in the self inductance is due to both the exposed nature of the IDTL drive loop on Mykonos as well as to the extended height of the coaxial transmission line. The extension in the transmission line, which will ultimately accommodate an X-pinch, is responsible for $\sim$4.5 nH of the 13.1 nH inductance increase. With $L \simeq 25.9$ nH and 150 kA of IDTL current, the drive flux in the Mykonos IDTL is 3.9 mWb. Interestingly both IDTL designs couple roughly the same amount of magnetic energy, $W_{\mathrm{m}} = \frac{1}{2} L I_{\mathrm{IDTL}} \sim 300$ J. In summary, we are coupling 40% more drive flux on Mykonos to an IDTL that is roughly twice as inductive as the ones fielded on Z, which results in a 30% drop in the induced IDTL current. In spite of this drop, 150 kA of IDTL current is still more than sufficient to drive an X-pinch.

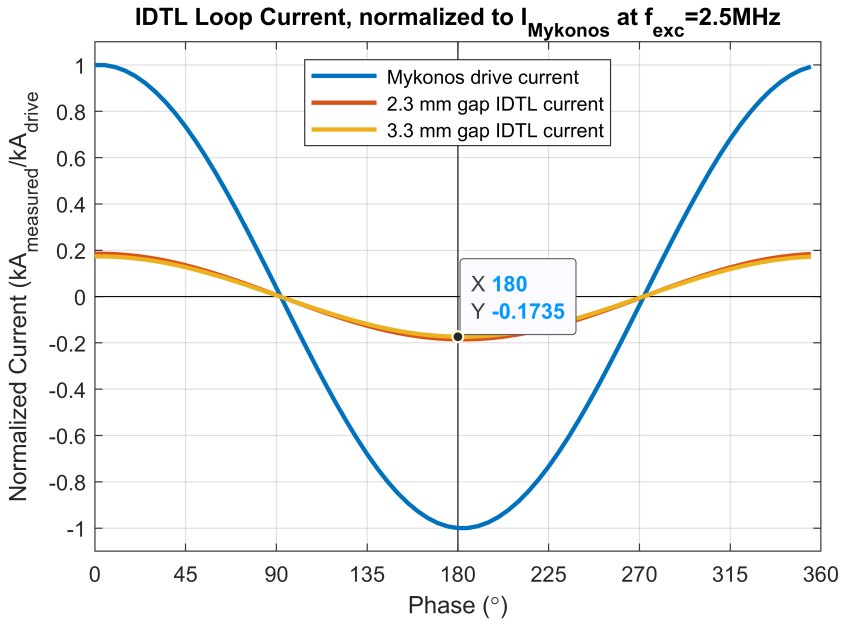

Figure 3-5. *Modeled IDTL currents indicating ~150 kA of in-phase IDTL current given 850 kA of Mykonos drive current (17.4% coupling). The IDTL with the 2.3 mm minimum A-K gap pulls slightly more current because of the slightly reduced inductance in its coaxial transmission line.*

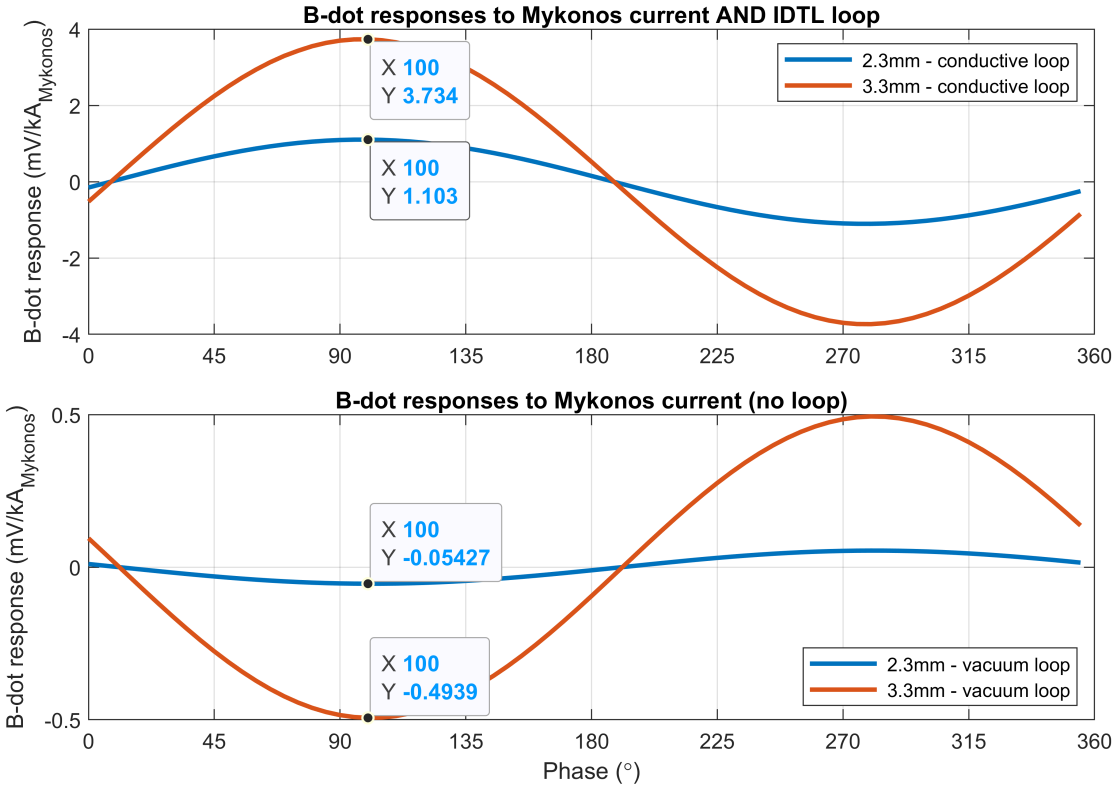

Figure 3-6. *Modeled B-dot voltages for the two different minimum A-K gap cases with (top) and without (bottom) the drive loop installed in the IDTL. The calculation without the drive loop assesses the non-negligible direct coupling between Mykonos and the IDTL B-dots.*

Figure 3-6 shows the expected B-dot voltages on the Mykonos IDTL (in mV/kA$_{\text{Mykonos}}$). The top panel shows the voltages generated in both the 3.3 mm and 2.3 mm minimum A-K gap IDTLs. For 850 kA of Mykonos current, this gives approximate signal strengths of 3.2 V and 0.9 V, respectively. The two cases differ by more than a factor of three because the B-dots in the 2.3 mm case are recessed substantially further from the IDTL power flow than in the 3.3 mm case (see Figure 3-3). Note that the calculated B-dot voltages in the top plot contain magnetic field contributions from both the IDTL currents and from direct coupling to Mykonos. The bottom plot in Figure 3-6 isolates the direct coupling to Mykonos by removing the IDTL drive loop from the calculation. It is notable that the direct coupling is both non-negligible ($\sim$13% in the 3.3 mm case) and oppositely directed from the IDTL coupling. In the next section, we will show that we tested this direct coupling by executing a no-drive-loop short-circuit IDTL experiment on Mykonos.

3.3. SHORT-CIRCUIT IDTL EXPERIMENTAL RESULTS

In this section, we present the data from the various short-circuit IDTL shots summarized in Table 3-1. Each 80 kV, 850 kA shot was preceded by a non-destructive 40 kV, 400 kA shot that serves as an *in situ* calibration shot. To calibrate the IDTL B-dots, we use the Green's function formalism in Equations 2.3 and 2.4 to identify a mutual inductance M and a flux penetration time τ_{f} for each B-dot sensor. Initially we had hoped to fit both M and τ_{f} to the 40 kV shot data and then apply the results to the corresponding 80 kV shot data to assess IDTL current coupling at full voltage and current. What we discovered, however, is that the τ_{f} values are not directly transferable from the 40 kV to the 80 kV cases.

The reason for this is that the 40 kV and 80 kV current pulses have different rise times ($\sim$135 ns in the 80 kV case versus $\sim$150 ns in the 40 kV case). This difference in rise time means that the two current pulses have different spectral content, giving rise to different fitted flux penetration times. More specifically, the mean fitted flux penetration time in the 40 kV cases is $\tau_{\text{f}} = 820$ ns, while the mean in the 80 kV cases is $\tau_{\text{f}} = 640$ ns. Using the longer 40 kV τ_{f} values on 80 kV data gives a poor fit. As such, we adopt the following calibration procedure: Rather than fitting τ_{f} to each data set, we fix it at the mean 80 kV value of $\tau_{\text{f}} = 640$ ns. We then use the 40 kV reference data to find the best-fit M value for $\tau_{\text{f}} = 640$ ns and then apply that M value and $\tau_{\text{f}} = 640$ ns to the 80 kV data. The results for six of the nine short-circuit Mykonos IDTL results are shown in Figure 3-7.

Each panel in Figure 3-7 shows at pair of Mykonos short-circuit IDTL shots, one 40 kV and one 80 kV. The Mykonos anode plate current for each shot is shown in blue, while the calibrated, integrated IDTL B-dot data are shown in red. Note that the IDTL data represents a measurement of the Mykonos current from within the IDTL. If current loss occurs in or near the IDTL, this will appear as an undershoot in the IDTL data relative to the Mykonos anode plate current. As the plots in Figure 3-7 show, nearly full current coupling is achieved in each case (between 90–100%). Furthermore, there are no sharp features in the IDTL waveforms that might indicate the onset of current loss mechanisms. As such, we conclude that we can reproducibly couple 150 kA of current to IDTLs on Mykonos, which is proof that we have successfully created a Z-surrogate IDTL platform on a 1 MA device. Note that the coupling percentages for all nine of the short-circuit IDTL shots are recorded in Table 3-1.

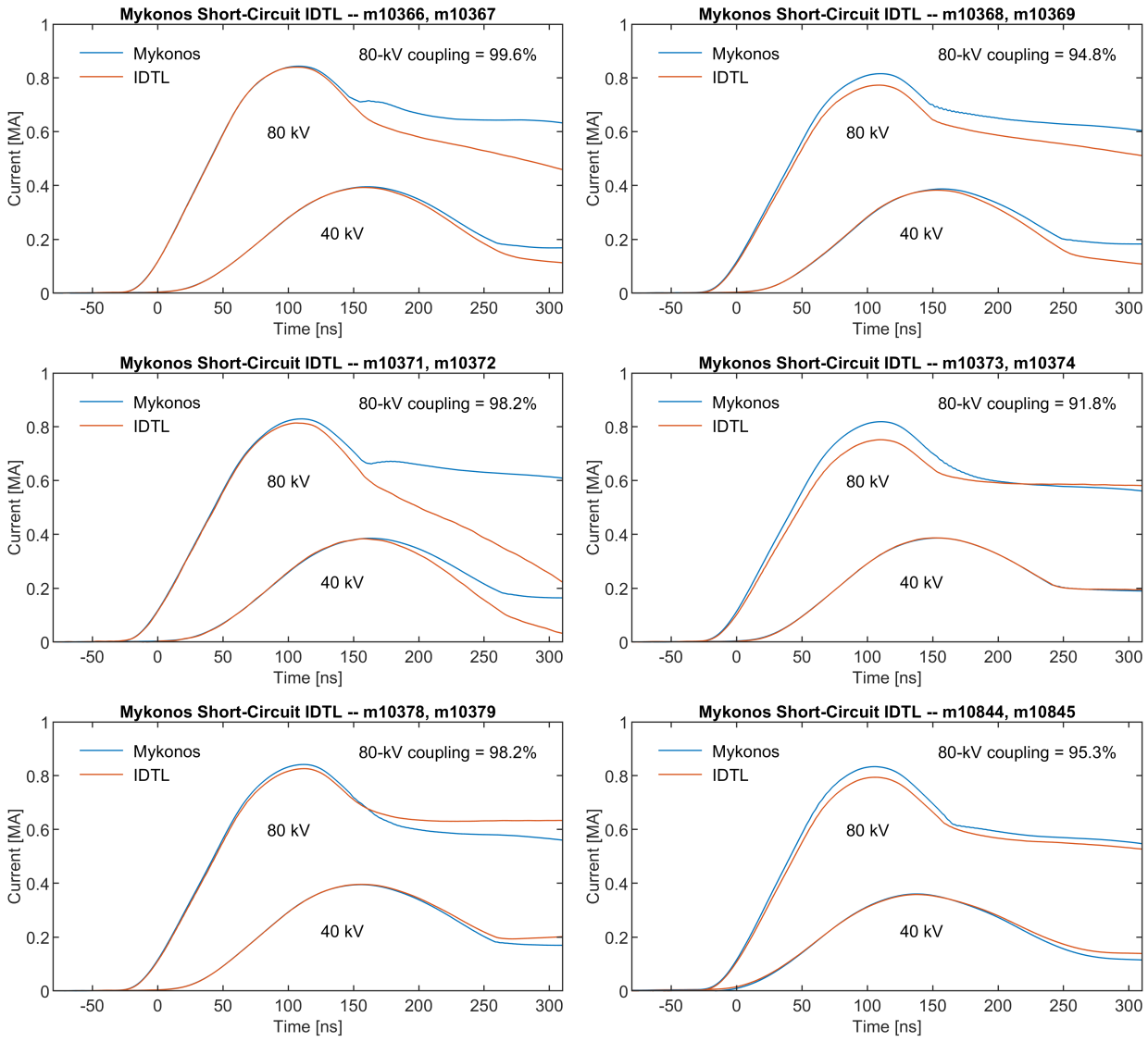

Figure 3-7. *Demonstration of 90–100% IDTL current coupling at* 80 kV *and* 850 kA *on Mykonos. The* 40 kV *shot data is used to calibrated the IDTL B-dots prior to each* 80 kV *shot. See the text for details.*

One important thing to note about the short-circuit coupling data shown in Figure 3-7 is that all three IDTL designs shown in Figure 3-3 exhibited excellent current coupling. This means that, at least in the 80 kV and 850 kA environment of Mykonos, the gap size and current polarity of the IDTL do not impact the current coupling. While this says little about the effect that these parameters might have in the harsher environment in the inner MITL on Z, it at least indicates that we are not operating near a current loss threshold in the short-circuit IDTLs on Mykonos.

The final analysis that we present from the short-circuit IDTL shots on Mykonos is a comparison of the experimentally measured B-dot calibration factors determined from the 40 kV reference shots and the modeled values reported in Figure 3-6. We note that the modeled values are given in volts per amp, whereas the calibration factors are typically given as a mutual inductance (or

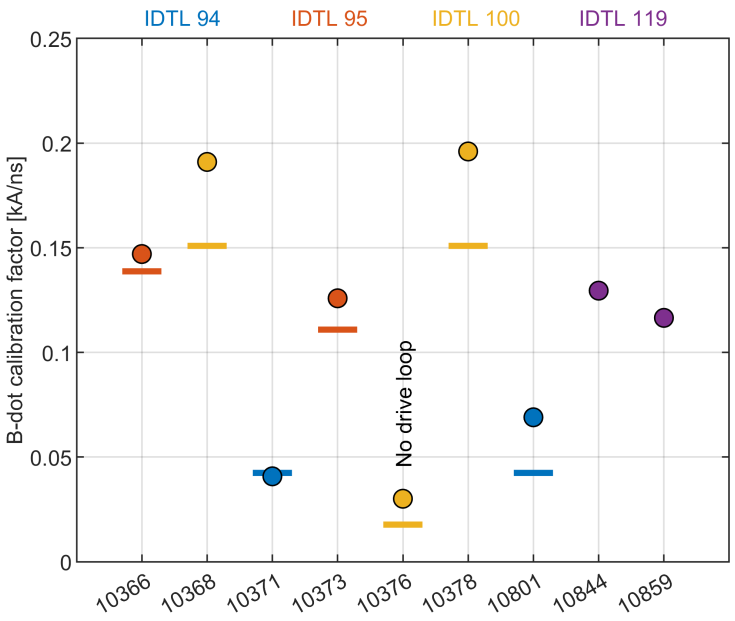

Figure 3-8. *Comparison of experimentally measured (circles) and modeled (lines) IDTL B-dot calibration factors. The experimental values are obtained from the common-mode-rejected average of the two B-dot sensors in the IDTL, and the modeled values incorporate the as-built dimensions of each B-dot loop. No modeled values are available for IDTL 119, which is of the reversed polarity design shown in Figure 3-3.*

equivalently in amps per second). To convert between the two, we use the relationship

$$V = -\frac{d\Phi}{dt} = -\omega M I \tag{3.2}$$

such that the reported V/I calibration factors can be related to the mutual inductance via $M = -(V/I)/\omega$. We report these M values here in units of kA/ns.

Figure 3-8 compares the experimentally measured calibration factors (circles) to the modeled values (horizontal lines). The experimental values are obtained from the common-mode-rejected average of the voltages measured by the two B-dot sensors in each IDTL. Additionally, the modeled values incorporate the as-built measurements of the depth of each B-dot loop in the IDTL body. This proves to be crucial for obtaining the 20% average agreement between experimental and modeled values that is shown in Figure 3-8. The average agreement degrades to nearly 50% without using the as-built measurements. The fact that modeled values capture the trends between the different types of short-circuit IDTL experiments builds confidence in the overall efficacy of the ANSYS HFSS approach to IDTL modeling.

One interesting shot in Figure 3-8 is 10376 on which we fielded IDTL #100 with no drive loop installed. This tests the direct coupling between Mykonos and the IDTL B-dots. The modeled ratio between the B-dot voltages generated in the shots without and with the drive loop is 12% (see Figure 3-6). While the B-dot calibration factors for IDTL #100 were found to consistently overshoot the modeled values, the experimentally observed no-loop/loop ratio is 16%, which is well in line with the modeled ratio.

4. INDUCTIVELY DRIVEN X-PINCH EXPERIMENTS ON MYKONOS

Having successfully demonstrated the coupling of 150 kA of current to short-circuit IDTLs on Mykonos, we now proceed to modify the Mykonos IDTL design to accommodate an inductively driven X-pinch (IDXP). For simplicity, we have chosen to pursue a hybrid X-pinch design [Shelkovenko et al., 2010]. Prior to commencing hybrid IDXP experiments, however, we conducted a series of hybrid X-pinch experiments in a more-traditional return-post X-pinch configuration (see Appendix A). These experiments provided preliminary experience with fielding both hybrid X-pinches and X-ray diagnostics on Mykonos without the added complexity of an IDXP. Once X-pinches had successfully been demonstrated in the return-post configuration, we proceeded to execute 21 hybrid IDXP experiments using the design shown in Figure 4-1.

The design principles for the IDXP shown in Figure 4-1 are as follows: First, we retain the bottom half of the geometry of the short-circuit Mykonos IDTLs presented in Chapter 3. This ensures maximum surrogacy with the tested design including the drive loop parameters and the B-dot sensitivities. The minimum drive loop standoff in the lower portion of the IDXP is set at 3.3 mm. Second, the upper portion of the IDXP chamber is expanded to accommodate two conical hybrid X-pinch electrodes while maintaining the same standoff distances. The total height of the cavity from the bottom face of the copper IDXP body to the base of the upper electrode is 29.75 mm. The electrodes are fabricated from a machinable tungsten alloy (ASTM-B-777,

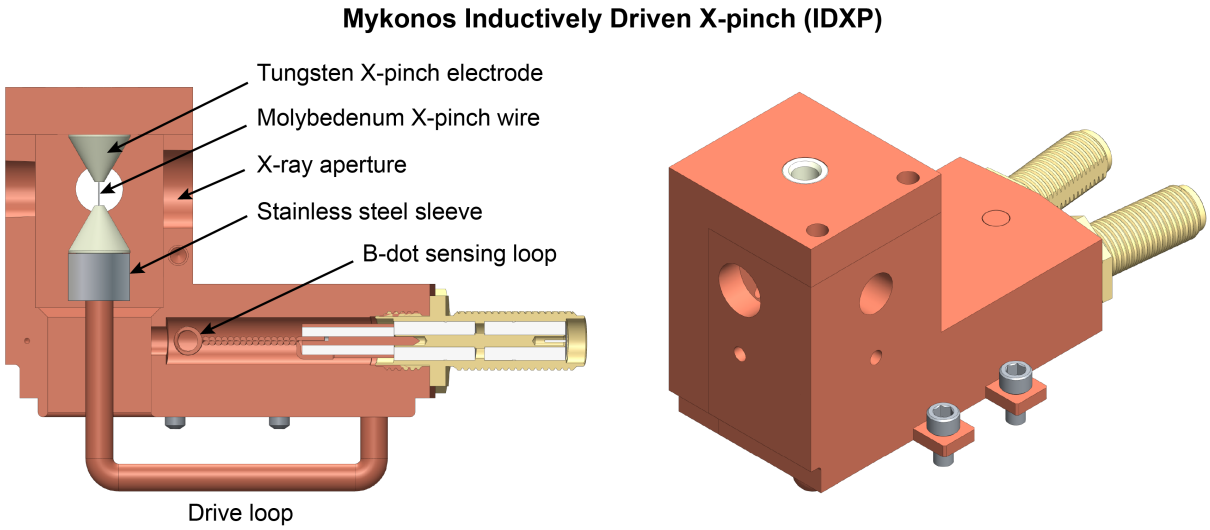

Figure 4-1. *The IDXP hybrid X-pinch assembly.*

Class 1). The power flow surface of each electrode is a 60° conical slope that converges to a 400 μm center hole through which the hybrid X-pinch wire is fed. The OD of the back side of each electrode is finished with an M6 thread, while the ID is counter-bored to slip fit onto the AWG #9 copper drive loop wire. The upper electrode screws into a removable L-shaped lid/side-panel that provides access for assembling the IDXP. Initially the lower electrode was held in place by an insulator that spanned the IDTL cavity, but we removed the insulator once it was discovered that the drive loop was able to hold the lower electrode in place without additional support. The threads of the lower electrode are covered with a stainless steel sleeve in the final design. For more information on hybrid X-pinch electrode testing see Appendix A.

The X-pinch wire material used in all of the IDXP experiments in this project is molybdenum. Molybdenum was chosen because it is a well-studied X-pinch material and the emission from Mo X-pinches has been shown to be continuum-dominated in the 3–8 keV energy range of interest (see Figure 1-3 and Shelkovenko et al. [2001]). While molybdenum wire diameters ranging from 13–50 μm were fielded during this project, most of the IDXPs used 15 μm wire. Note that the X-pinch A-K gap shown in Figure 4-1 is 2.5 mm. This is substantially larger than the 0.8 mm optimum gap published in the literature [Shelkovenko et al., 2010], but, as we will show, we could not generate quality X-pinch sources with gaps smaller than 2 mm.

The fabrication process developed for the IDXP hybrid X-pinches is as follows:

1. Prior to assembling the hybrid X-pinch, solder one end of the drive loop into the hole between the B-dot channels in the IDXP body. Select the A-K gap in the X-pinch by adjusting the amount that the other, free-floating end of the drive loop extends upward into the IDXP cavity. After soldering, bead blast the IDXP body and drive loop and install the B-dot sensing loops into their respective channels.
2. Separate from the IDXP body, feed a suitable length of molybdenum wire through the 400 μm hole in the lower electrode assembly, which includes both the tungsten electrode and the accompanying stainless steel sleeve.
3. Affix a small piece of copper tape to the portion of the Mo wire that is protruding from the back of the lower electrode. Then pull the tape into the pocket in the electrode until it catches to hold the wire in place.
4. Slide the lower electrode assembly with the fine Mo wire protruding from it onto the free-floating end of the IDXP drive loop. This compresses the small piece of copper tape between the tip of the drive loop and the interior of the lower electrode.
5. Feed the free-floating end of the Mo wire through the 400 μm hole in the upper electrode, which is already screwed into the L-shaped copper lid/side panel.
6. Attach temporary wire weights to the free-floating end of the Mo wire that is now protruding through the top of the L-shaped lid/side-panel.
7. Carefully slide the L-shaped lid/side-panel along the weighted wire until it mates to the IDXP body. Fasten the lid/side-panel into place with four screws.
8. Lift the completed IDXP assembly so that the wire weights pull the Mo wire tight in the A-K gap. Tape the taut wire to the outside of the IDXP body and cut away the wire weights.

Once the IDXP is assembled, it is ready to be installed onto the Mykonos IDTL A-K hardware that is described in Section 3.1. With practice, the time to assemble an IDXP as described above can be as little as 15 minutes (not including the refurbishment and preliminary assembly activities described in Step 1). Over the course of the experimental campaign, a total of five IDXP bodies (S/Ns 101 and 115–118) were kept in circulation to allow for parallelized refurbishment, assembly, and execution of experiments.

4.1. IDXP DIAGNOSTICS

A much more sophisticated diagnostic suite is required to characterize the X-ray-producing IDXP experiments than was required for the short-circuit IDTL experiments described in Chapters 2 and 3. The IDXP diagnostic suite developed for this project, which includes X-ray diodes, visible-light shadowgraphy, and three different radiography diagnostics, is summarized in Figure 4-2. The downward-skewed A-K hardware allows the hybrid X-pinch within the IDXP body to sit at chamber center. At this position, the X-pinch can be observed from five different vacuum ports, two on the sides of the chamber and three on a newly designed and procured aluminum lid. The five line-of-sight diagnostics shown in Figure 4-2 are as follows:

Four-frame visible shadowgraphy. A green visible shadowgraphy system ($\lambda = 532\,\text{nm}$) acquires four frames separated by 5 ns each. The four frames are captured by splitting the sub-nanosecond laser pulse into two optical paths and acquiring images in two polarizations on each optical path. The 5 ns interframe spacing is set by changing the physical path length of each leg and/or polarization. This system was primarily used to examine the gross morphology of the pinching wire and to characterize electrode plasma generation.

High-magnification penumbral imaging. A sharp-edged 0.125" molybdenum aperture is affixed directly to the outside of the IDXP body at a source-object distance (SOD) of 11.25 mm. An image plate at the chamber wall captures the projection of the aperture at a source-detector distance (SDD) of 197.5 mm. This gives a nominal magnification of $M = \text{SDD}/\text{SOD} \simeq 17.6$. The image plate sits behind 508 μm of Kapton filtration. This diagnostic provides the best means of estimating the size and location as well as the relative intensity of the X-ray sources that are produced by the IDXP.

Step wedge radiography. A step wedge with nine progressive aluminum steps in one direction and four progressive copper steps in the other is built on 508 μm of Kapton and mounted directly on top of an image plate located 240.4 mm from the source. The resulting contact radiograph provides coarse spectral information about the X-pinch sources.

Mag-2 imager. A mag-2 imaging setup was used either to acquire low-magnification penumbral imaging or to backlight a clear-optical-path 1951 USAF resolution target [Edmund Optics]. The data in the resolution target images extends down to a 35 μm spatial scale (14.25 lp/mm) and can be used to identify the highest quality pinches. The SOD of the setup is 96.7 mm and the SDD is 206.1 mm, which gives $M = \text{SDD}/\text{SOD} \simeq 2.1$. As with the other radiography systems, the image plate sits behind 508 μm of Kapton filtration.

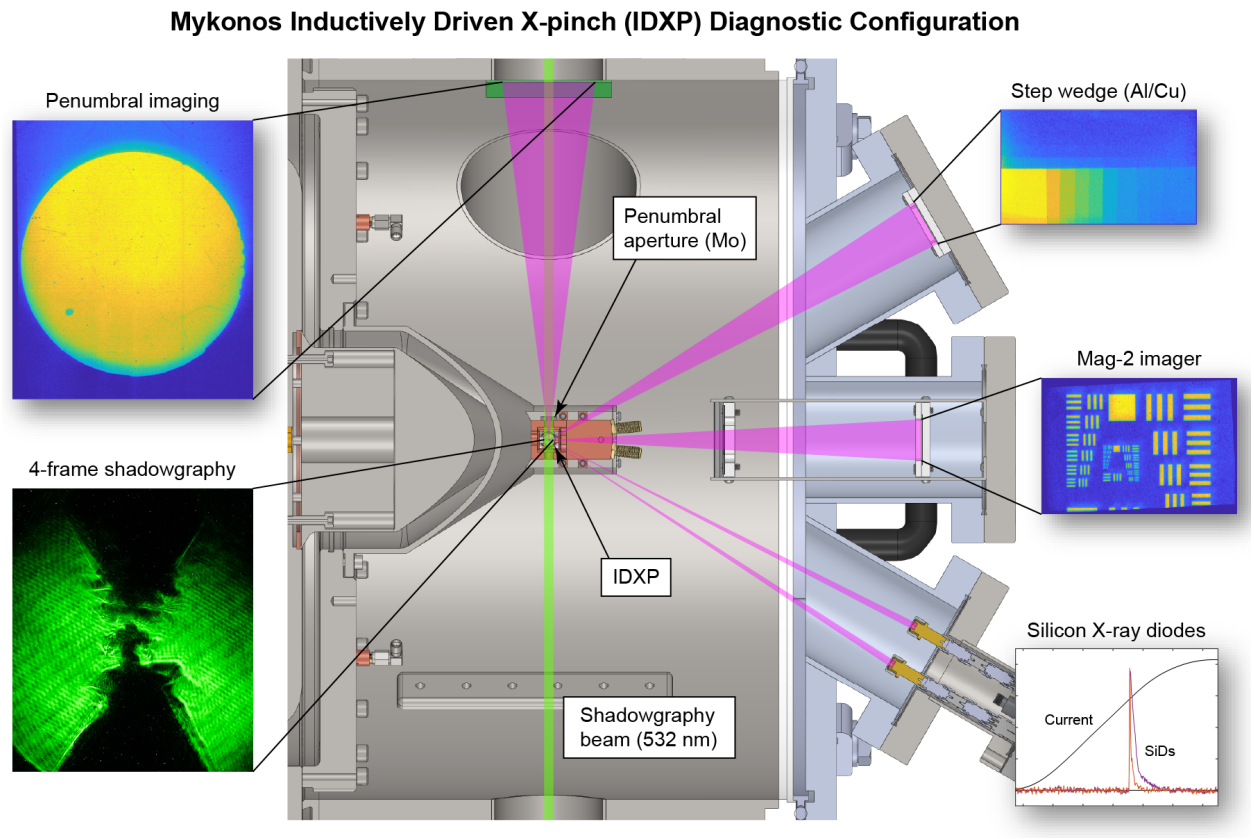

Figure 4-2. *The IDXP line-of-sight diagnostic configuration with representative data from each instrument. All of the X-ray data shown here was acquired simultaneously on Shot 10862. The shadowgraphy image was acquired separately on Shot 10881. See the text for further details*

Silicon X-ray diodes. Two silicon diodes were fielded at a distance of 227.6 mm on every experiment to capture the X-ray emission from the X-pinch. The filtration of one of the diodes (254 μm Kapton + 8.5 μm aluminized Kapton) was not changed throughout the campaign so as to serve as a reference for all of the IDXP experiments. Note that close-in PCD (photoconducting diode) measurements were also attempted on five shots. These diodes were mounted directly to the outside of the IDXP body. While these measurements returned valuable data, they also appear to have perturbed the experiment by creating spurious X-ray sources near the hybrid X-pinch.

In addition to the line-of-sight diagnostics described above, the standard B-dot configuration from the short-circuit IDTL experiments was retained. Comparing the signals from the B-dots embedded in the IDXP to the anode plate B-dot signals (see Figure 3-2) provides valuable information about current coupling to the X-pinch, which is an inductively evolving load.

A total of 21 hybrid IDXP experiments were conducted during this project. Table 4-1 summarizes these experiments by breaking them into three distinct groups. The first group (shots in the range 10380–10819) consists of experiments where the molybdenum wire diameter was larger than 15 μm. Note that this range of shot numbers is large because these shots spanned two different experimental campaigns. None of these four experiments generated an X-pinch source, which led

Shot	Mo wire	A-K gap	Blasted	Shadowgraphy	Mag-2 Imager	Penumbral	Step wedge	X-pinch
10380†	25 µm	—	—	Yes	USAF target	—	—	—
10812	30 µm	—	—	—	Mo aperture	—	—	—
10814	25 µm	—	—	—	Mo aperture	—	—	—
10819	25 µm	2.1 mm	—	Yes	Mo aperture	—	—	—
10830	15 µm	2.3 mm	—	Yes	Mo aperture	—	—	62.2 ns
10834	15 µm	1.9 mm	—	Yes	Mo aperture	—	—	68.0 ns
10837	15 µm	2.4 mm	—	Yes	—	—	Al only	65.5 ns
10840†	15 µm	2.3 mm	—	Alignment	—	—	Al+Cu	64.5 ns
10847†	15 µm	1.6 mm	—	Alignment	Mo aperture	—	Al+Cu	—
10849	15 µm	1.4 mm	—	Alignment	Mo aperture	—	Al+Cu	63.8 ns
10851	15 µm	2.5 mm	—	Alignment	Mo aperture	—	Al+Cu	72.7 ns
10853	15 µm	2.3 mm	—	Alignment	Mo aperture	Yes	Al+Cu	56.7 ns
10855	15 µm	2.3 mm	—	Alignment	Mo aperture	Yes	Al+Cu	—
10862	15 µm	2.4 mm	Yes	Alignment	USAF target	Yes	Al+Cu	50.6 ns
10864	15 µm	2.6 mm	Yes	Alignment	USAF target	Yes	Al+Cu	65.1 ns
10866	15 µm	2.6 mm	Yes	Alignment	USAF target	Yes	Al+Cu	61.4 ns
10868†	15 µm	∼1 mm	Yes	—	USAF target	Yes	Al+Cu	80.1 ns
10870†	15 µm	∼2 mm	Yes	—	USAF target	Yes	Al+Cu	59.4 ns
10876†	15 µm	2.1 mm	Yes	Alignment	USAF target	Yes	Al+Cu	72.2 ns
10879	15 µm	2.3 mm	Yes	Yes	USAF target	—	Al+Cu	88.2 ns
10881	15 µm	2.5 mm	Yes	Yes	USAF target	—	Al+Cu	58.5 ns

Table 4-1. *List of the 21 hybrid IDXP shots conducted on Mykonos. The A-K gap spacing is measured using pre-shot shadowgraphy images where available. The X-pinch timing is extracted from the rise of the reference silicon X-ray diode pulse. The three* ***bold*** *experiments generated the strongest pinching behavior as observed on the radiography diagnostics. The six experiments with a dagger† were polluted by spurious X-ray sources. See the text for further details.*

us first to drop the insulator from the inside of the IDXP (after shot 10814) and then to reduce the wire diameter and therefore the imploding mass (after shot 10819). The second group of experiments (shots in the range 10830–10855) all used 15 µm Mo wire and frequently generated X-pinch sources. However, a lack of X-pinch reliability in this second grouping led us to start bead blasting rather than sanding the electrodes after shot 10855. All of the shots in the third group (10862–10881) used 15 µm Mo wire and bead-blasted electrodes. Every shot in this group generated an X-pinch source, though the quality of the source still varied from shot to shot.

Table 4-1 also includes information about the line-of-sight diagnostic configuration for each shot. Silicon X-ray diodes (SiDs) were fielded on every shot so they are not tracked in the table. Additionally, shadowgraphy and penumbral imaging were not fielded simultaneously during this campaign,[1] but the shadowgraphy system was still used to take pre-shot alignment images on the

[1] Shadowgraphy and penumbral imaging could be fielded simultaneously in future campaigns by punching a hole in the penumbral image plate to allow the shadowgraphy beam to pass through and exit the chamber. The shadowgraphy beam would, however, be cropped by the penumbral aperture.

shots where penumbral imaging was fielded. These alignment images are valuable in that they provide an *in situ* measurement of the A-K gap between the conical electrodes. The measured gap distances are listed in Table 4-1. Finally, if an X-pinch source was generated, the pinch time is extracted from the silicon diode data and listed in the last column of Table 4-1.

At this juncture we note that two IDXP experiments were conducted with a more-traditional two-wire X-pinch configuration rather than a hybrid X-pinch configuration (see Figure 1-2). These two experiments (10872 and 10874) are not listed in Table 4-1, but they are discussed in some detail in Appendix B. The fact that we were able to assemble and field two-wire IDXPs demonstrates that the IDXP concept is not limited to the hybrid X-pinch design.

Over the course of the IDXP experiments, two major challenges were encountered with spurious X-ray sources polluting the X-ray diagnostics. The first was that the Mykonos insulator behind the anode plate (see Figure 3-2) would often flash over during IDXP shots. This behavior was rarely observed during short-circuit IDTL experiments, and it was initially ascribed to the harsher inductive voltage generated by the IDXP load. Not only do the insulator flashes break the symmetry of current delivery to the load region, the arc flash itself generates X-rays that can escape through slots in the Mykonos anode plate and pollute the X-ray diagnostics. After experiencing insulator flashes on three of the first nine IDXP shots, it was decided to install stainless steel shields over the anode plate slots so that the X-ray diagnostics wouldn't be polluted even if the insulator flashed. The anode plate with the insulator shields installed is shown in Figure 4-3. Interestingly, after the shields were installed (after Shot 10851), no insulator flashes occurred for the remaining 12 IDXP shots (as determined from the anode plate B-dots). As such, it is possible that the insulator flashes were caused by IDXP radiation impinging on the insulator,

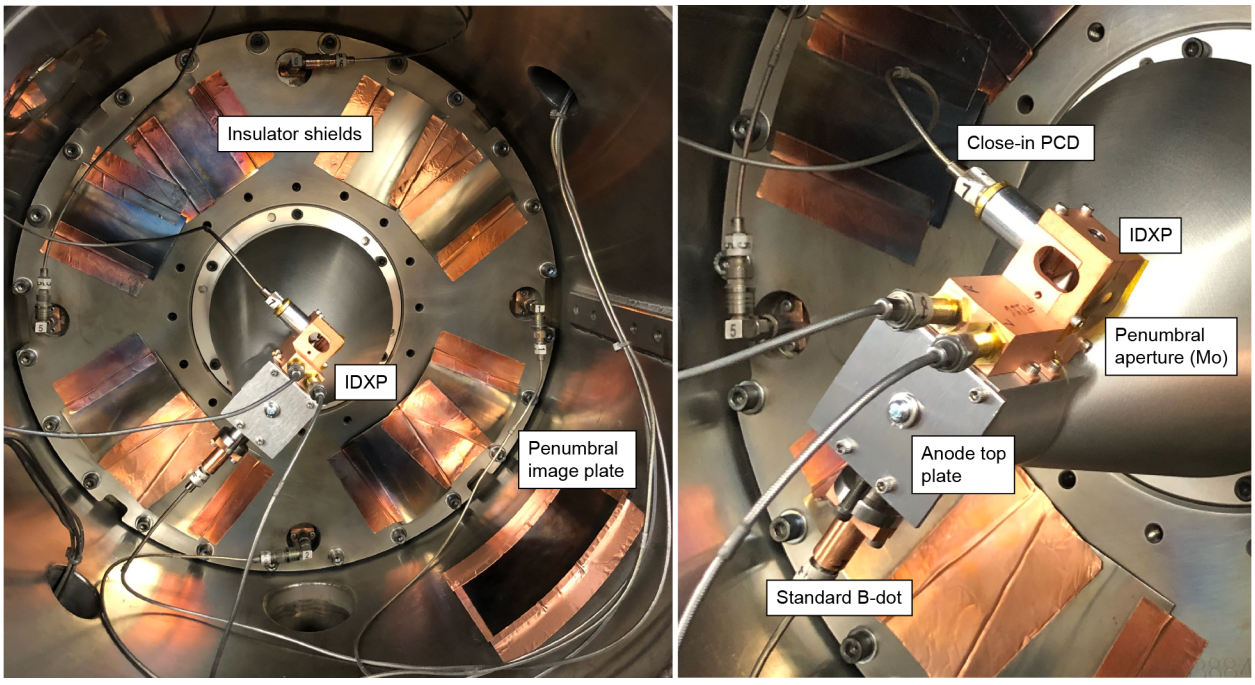

Figure 4-3. *The Mykonos chamber before Shot 10868. Both the stainless steel insulator shields, which are held in place by copper tape, and the close-in PCD configuration are shown.*

which would have been eliminated when the shields were installed. Regardless of the specific mechanism, the shields eliminated the impact of insulator flashes on the X-ray diagnostics.

The second major challenge with spurious X-ray sources occurred when a close-in PCD was attached to the exterior of the IDXP body (see Figure 4-3). Unlike the insulator flash X-rays, the PCD-induced X-rays appeared as a second X-ray source later in time than the X-pinch (anywhere from tens to hundreds of nanoseconds later). In total, the close-in PCD was fielded on five shots, two of which were the two two-wire X-pinch shots. On the first two of these five shots (10868 and 10870), the PCD filtration was exposed to the IDXP power flow and generated a strong X-ray source very late in time that swamped the radiographic diagnostics. On the remaining three shots (10872, 10874, and 10876), the filtration was better placed, but two of these three shots generated a second, diffuse X-ray source $\sim$20 ns after the X-pinch that again overwhelmed the X-pinch signatures on the radiographic diagnostics. The close-in PCD was removed for the final two shots (10879 and 10881) and no secondary sources were generated. While the evidence is not conclusive, these results indicate that the close-in PCD may have perturbed the IDXP source.

4.2. B-DOT AND X-RAY DIODE RESULTS

A quality X-pinch must be both spatially and temporally compact. The best X-pinches are therefore characterized by the combination of a sharp diode pulse (temporal compactness) and sharp radiographic features (spatial compactness). Figure 4-4 shows a sampling of B-dot and X-ray diode results from the hybrid IDXP experiments. Note that the time bases have been shifted relative to the time when the anode plate current reaches 100 kA. The three experiments with sharp diode pulses shown in the left column are the three most spatially compact IDXP sources (from a radiographic perspective) obtained during this project (see Section 4.3for more detail). Each X-pinch generates an inductive dip on the current waveform that is integrated from the IDXP B-dots. The sharpest inductive features, which are most visible in the raw IDXP B-dot traces shown at the bottom of each panel in Figure 4-4, correlate well with the timing of the X-ray pulse(s) on the X-ray diodes. Note that the middle shot in the left column (10866) exhibits a multi-pinch behavior that is observed on the diodes and the B-dots as well as on the penumbral imaging data (see Figure 4-13 in Section 4.3.1).

The three shots in the right column of Figure 4-4 show several different IDXP failure modes. The first (10819) is an over-massed X-pinch with a 25 μm rather than a 15 μm wire. The current detected in the IDXP does roll over after $t \sim 60$ ns, presumably from the inductive evolution of the Mo wire, but no X-pinch source is generated. The second shot in the right column (10868) has a narrow A-K gap (less than 2 mm) and fails to pinch sharply. Three such narrow-gap shots were attempted but none of the three produced a viable X-pinch source. It is clear that 10868 came very close to pinching in that it generated both an inductive dip and a weak X-ray pulse, but the sharp burst of X-rays associated with an X-pinch source is absent from the diode traces. The third shot in the right column (10876) fails due to the formation of a large secondary X-ray source after what appears to be a successful X-pinch. This secondary source ruins the radiography for this shot. Note that this shot was one of the five that were fielded with a close-in PCD (see Section 4.1).

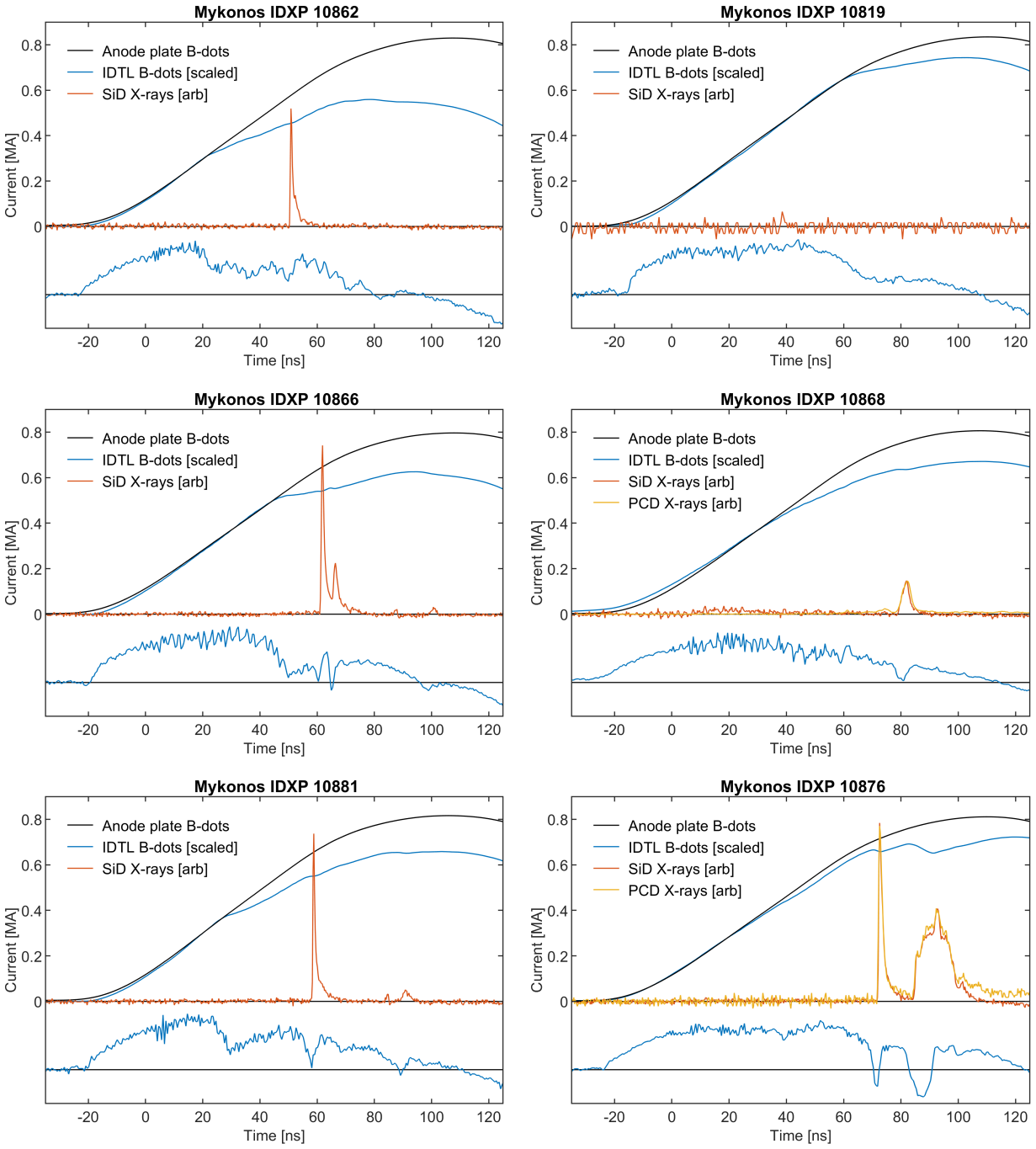

Figure 4-4. *A sampling of IDXP current coupling and X-ray diode results. The integrated IDXP current (blue) is scaled to compare with the Mykonos anode plate current (black) that serves as the input to the experiment. A raw IDTL B-dot trace (also in blue) is shown at the bottom of each panel to emphasize the inductive features associated with the pinching of the wire. The reference silicon diode (red) is shown for every experiment, and the close-in PCD (yellow) is shown where available. Note that all of the time bases have been shifted to the time when the anode plate current reaches* 100 kA.

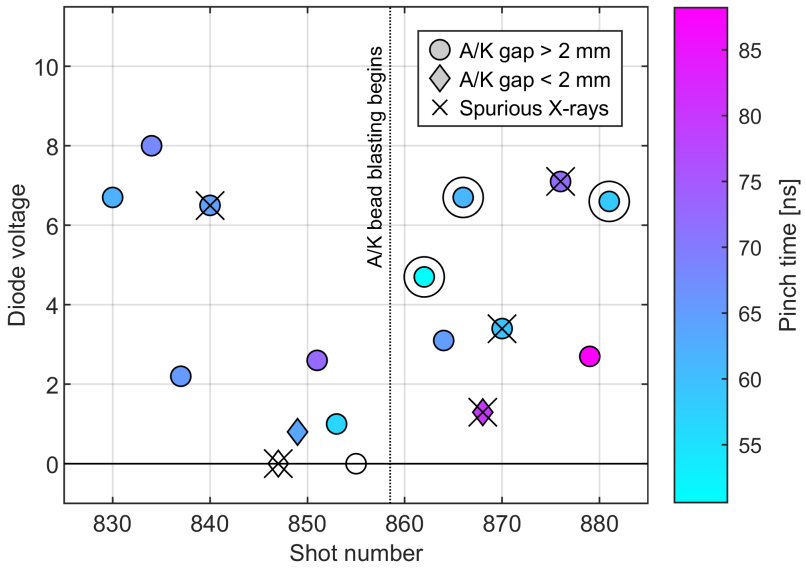

Figure 4-5. *Summary of X-pinch amplitude and timing as measured by the reference silicon diode. Shots with spurious X-ray sources either from insulator flashes or the close-in PCD are crossed out. The three circled shots are the three highest performing IDXPs from a radiographic perspective (see Table 4-1).*

Figure 4-5 aggregates the X-pinch amplitude and timing information from the reference silicon diode for all 17 of the 15 µm molybdenum wire shots. Of the nine shots executed before we started to bead blast the electrodes, three of the first four produced substantial X-rays, but none of the subsequent five shots were able to replicate this behavior. Note that two of those five shots fielded a narrow A-K gap, but three of them did not. The final shot in the grouping (10855) failed to pinch entirely without an obvious cause. We hypothesize that the observed degradation in X-ray production is due to insufficient electrode cleaning between shots. Roughly four sets of electrodes were in circulation for these shots, so it is conceivable that each one pinched well the first time but then required cleaning beyond sanding to be restored to its initial condition. We achieve this by bead blasting the electrodes starting on Shot 10862. Every shot thereafter generated X-rays, and all three of the highest-quality pinches from a radiographic perspective were obtained from the set of seven bead-blasted shots.

Figure 4-6 compares shadowgraphs from shots before and after bead blasting was implemented. For each shot, the shadowgraph taken at the time of the pinch is overlaid on the corresponding preshot image. This serves to highlight the electrode plasma generated during the shot. Qualitatively, there is less plasma expansion from the bead-blasted electrodes than from the sanded electrodes. This reduced plasma formation could explain the better performance seen from IDXPs with bead-blasted electrodes, though further statistical analysis would be necessary to quantitatively draw this conclusion. Unfortunately, the shadowgraphy system was unavailable for most of the IDXP shots such that there is not enough data to investigate the electrode conditioning hypothesis in more detail.

Returning to Figure 4-5, the timing of each X-pinch is displayed in color. The observed timing variability is rather high with the stronger sources general pinching in the 20 ns window between 50–70 ns after the 100 kA time. This high timing variability is a concern for eventual IDXP

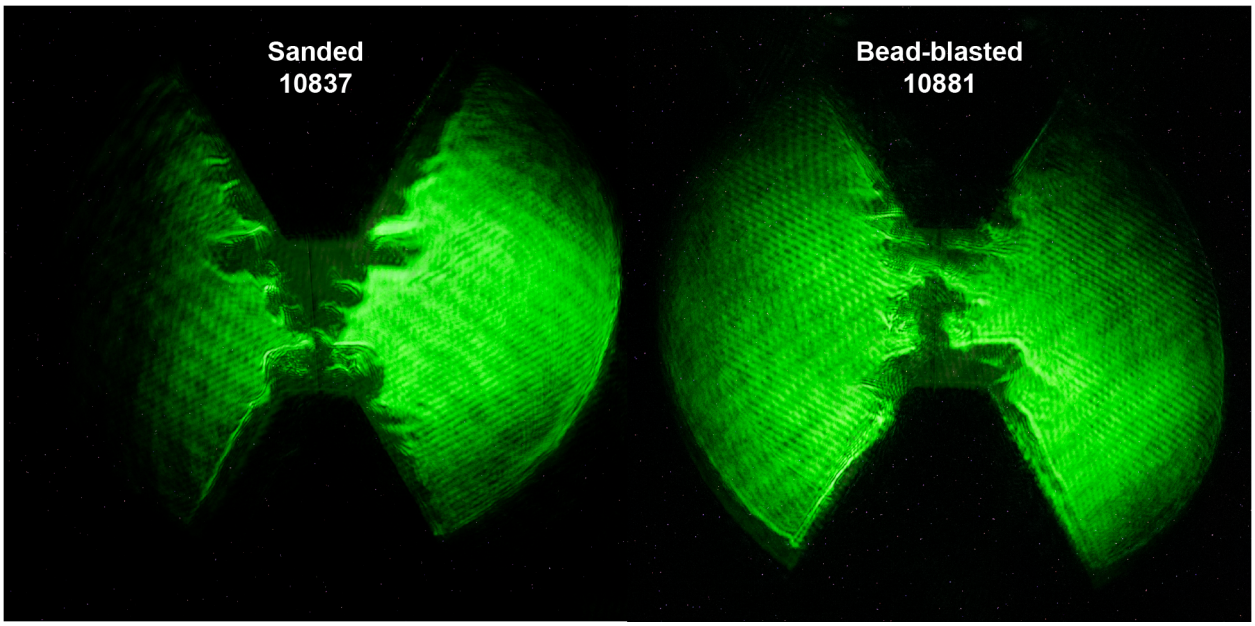

Figure 4-6. *Comparison of laser shadowgraphs from IDXP shots with sanded (10837) and bead-blasted (10881) electrodes. Each image is a composite of the shadowgraph taken exactly at the time of the pinch overlaid on the pre-shot image from the same channel. This technique highlights how the surface of each electrode has expanded during the experiment.*

backlighting experiments where timing control is highly desirable.

Finally, it is interesting to note that all three of the narrow-A-K-gap shots that were attempted failed to produce a usable X-pinch source (the diamonds in Figure 4-5). This is in spite of the published hybrid X-pinch literature where very narrow gaps (0.8 mm) are used [Shelkovenko et al., 2010]. While it is possible that the current and voltage characteristics of the IDXP are different enough from, say, the XP pulser at Cornell University to change the electrode plasma formation characteristics, it is not presently understood why the narrower A-K gaps failed to work here. This is unfortunate because the multi-pinch behavior observed on Shot 10866, for example, could likely be avoided if narrower A-K gaps could be used. Perhaps better electrode conditioning protocols beyond even bead blasting (e.g., plasma etching) would further reduce electrode plasma formation and enable the fielding of narrower-gap hybrid IDXPs.

4.3. RADIOGRAPHY RESULTS

Figure 4-7 plots the USAF resolution target point-projection radiographs from the Mag-2 imager obtained from the eight bead-blasted, 15 μm Mo wire shots. These resolution target images qualitatively agree with the source quality trends seen in the diode data in Fig. 4-5. The best single-pinch sources (10862 and 10881) clearly resolve the smallest elements in the resolution target, which are 35 μm in width (14.25 lp/mm). However, obtaining more quantitative information about the spatial scale of the X-pinch source requires the higher magnification of the penumbral imaging diagnostic.

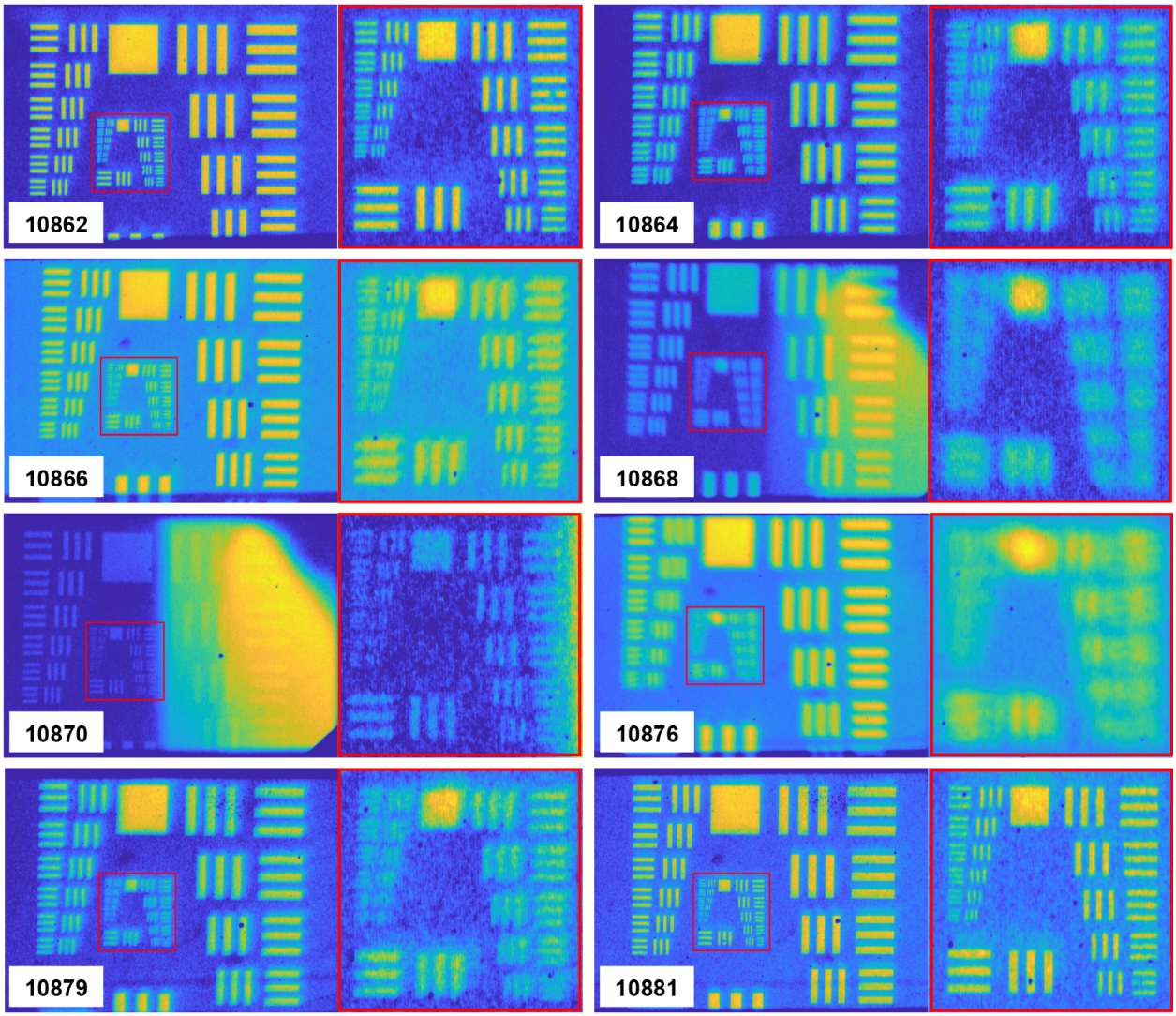

Figure 4-7. *USAF resolution target point-projection radiographs from the Mag-2 imager on eight different IDXP shots. The right-hand side of each image is a magnified inset of the smallest features on the resolution target (*35 μm*).*

4.3.1. Penumbral imaging

Theoretical background

There are several established methods for measuring the X-ray source size distribution, some more quantitative than others. Often test objects of various types are designed to produce radiographs with different features to analyze. These objects fall into the categories of resolution targets, edges, slits, or pinholes. One of the challenges of pinhole imaging—one of the most commonly used techniques—is that the pinhole size determines the resolution and the image intensity, and those effects cannot be easily separated from each other. Pinholes are only useful if they are much smaller than the object being imaged. Penumbral imaging is the opposite extreme of pinhole imaging—using very large “pinholes" where the size is much larger than the X-ray

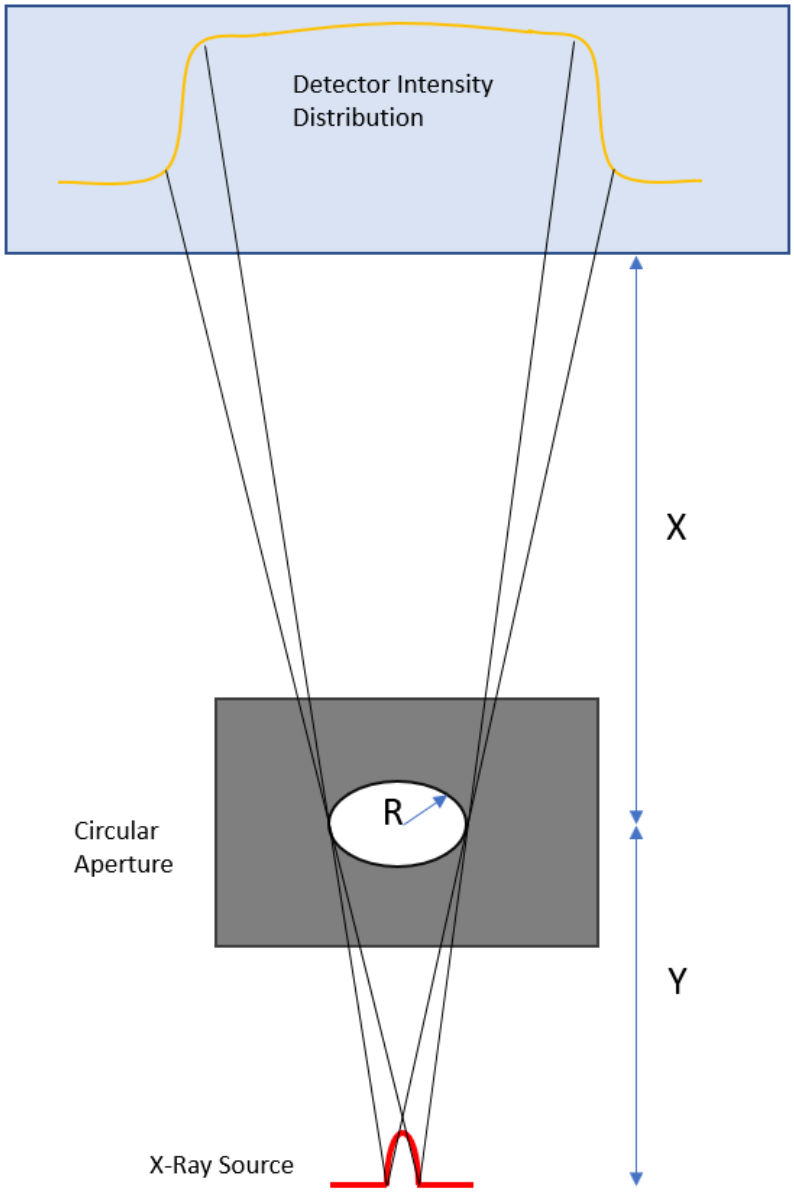

Figure 4-8. *Penumbral imaging geometry.*

Measurement	Formula	Mykonos value
Magnification	$M = (X+Y)/Y$	17.6
Detector plane	$\Delta x \equiv$ pixel size	100 µm
Object plane	$\Delta x/M$	5.7 µm
Source plane	$\Delta x/(M-1)$	6.0 µm

Table 4-2. *Spatial scaling of radiographs.*

source—and the resolution and intensity become separable even though the resulting image does not “look like" the source.

Penumbral imaging is also an extension of using edges [Ekdahl, 2011] to measure X-ray source sizes. From an edge (ideally a very long, straight one) the *edge spread function (ESF)* is obtained from which the *line spread function (LSF)* can easily be calculated (it’s just the derivative). The shapes of the edge profiles give specific information about the size in the direction perpendicular to the edge direction which is why edges in two or more directions give more information on the two-dimensional X-ray source than one. A generalized penumbral imaging geometry is sketched out in Figure 4-8 which also illustrates the ESF. When the source size is much smaller than the aperture radius, R, then the aperture essentially becomes a continuous edge in 2π and thus, in principle, all information about the source size and symmetry is obtainable by taking various lineouts at different angles. Note that a complete circle is not strictly required since the same information is obtained on one side of the circle and on the side directly opposite.

One simple metric to quantify the X-ray spot size is to examine the FWHM (full-width, half-maximum) of the LSF. When the spot size is small and has reasonable symmetry this is quite convenient. When the spot is large, on the other hand, the FWHM may not be well defined. We will see examples where both circumstances exist, even simultaneously.

There is a lower limit to the size of an X-ray spot that can be measured. This is due to the intrinsic “blur" of the detector which will always broaden the ESF or LSF. To overcome the detector blur—which should be quantified in order to measure this limit and also, as necessary, to remove the detector blur contribution—the aperture should be fielded at a large magnification. Of course, there is some limit to the magnification given physical constraints such as the detector size. One must be cognizant of the “measurement plane" and scale distances appropriately (see Table 1). For instance, to calculate the effect of detector blur on the spot size measurement, one measures the LSF FWHM of an aperture or an edge (the blur is usually fairly symmetric about the circle) at a magnification of 1.0 (i.e., a “contact" radiograph) and then divides the result by $(M-1)$, where M is the magnification. A spot size that is directly measurable should create a LSF FWHM greater than the rescaled detector blur. *For the purposes of this report and to be conservative we will put forth the convention that the resolution limit for the spot size is twice the detector blur, scaled to the source plane.* In principle, one could resolve somewhat better than that limit, but it would likely be less quantitative.

Experimental results

In the case of the penumbral imaging on the Mykonos IDXP experiments, we find from the various ESFs that the X-ray source often contains a complex distribution of source sizes. The ESF indicates that there can be a mixture of a small X-ray source (from the X-pinch hot spot) and one or more much broader sources. To illustrate this, Figure 4-9 shows a set of IDXP radiographs. A high-magnification penumbral image is shown in the larger, top-right image with a lineout at left. The magnification is 17.6 (measured directly by knowing the aperture size). The lineout is an ESF in a particular direction. One can visually discern a faint sharp circle in the image, but the ESF reveals that most of the energy is actually in a very broad source with a small “blip" at the edge

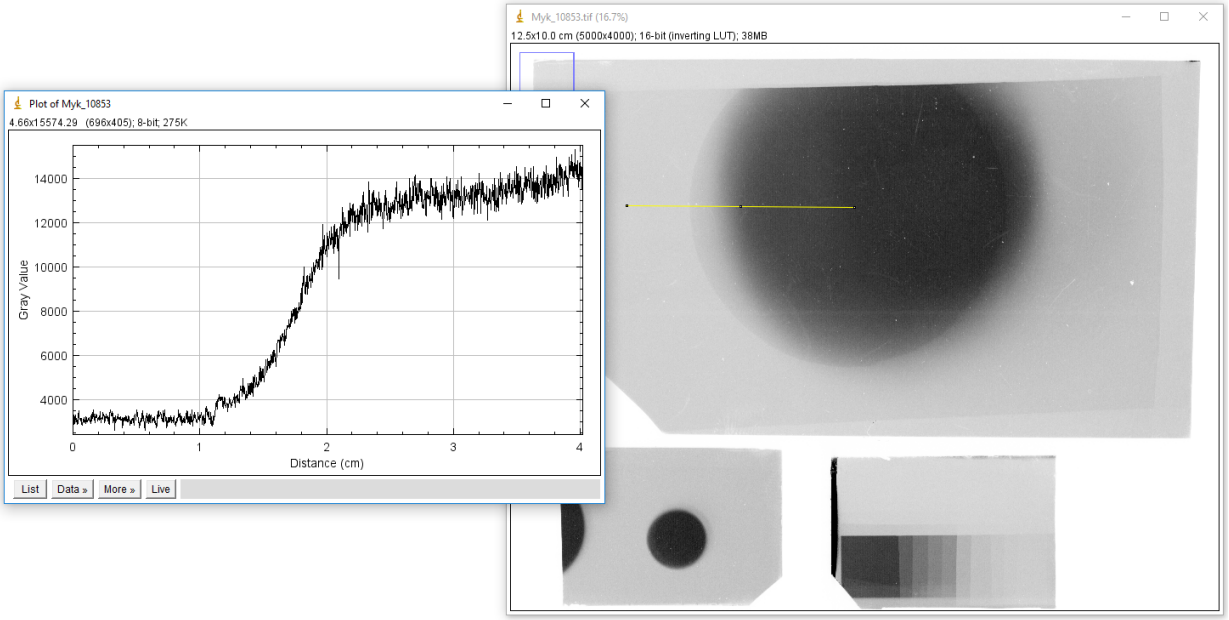

Figure 4-9. *Views of the image plate scans on Shot 10853. Upper-right is the high magnification penumbral image; Lower-center is the low magnification penumbral image; lower-right is the step wedge; left: a lineout across the high mag penumbral image (yellow line) indicating ESF.*

representing the sharp circle. The smaller image in the bottom-center is another penumbral image from a different aperture with a magnification of roughly unity. This second penumbral image gives similar shape to the high-mag image, but it is more difficult to discern the detailed ESF.

Recalling that we need a measurement of the detector blur, we can use the step wedge radiograph like the one seen in the lower-right of Figure 4-9 since it is in near-contact with the image plate and the steps form straight edges from which ESF and LSFs can be extracted. The easiest way to process LSF data from this images is to use a Sobel edge filter directly on the image [Gonzalez and Woods, 2008]. In practice, some pre-processing of the images is performed to reduce noise, banding, etc. [Topaz DeNoise] which are enhanced though the Sobel filter. The results are shown in Figure 4-10. The detector plane LSF FWHM is 100 μm, so the corresponding resolution at the source plane is 6 μm (see Table 4-2). Therefore the resolution limit for constraining the X-ray spot size in this analysis is ∼12 μm.

One of the shots, 10862, performed quite well in generating a small X-pinch hot spot that produced a large fraction of the X-ray yield. The raw and processed penumbral data for this shot are shown in Figure 4-11. The raw penumbral image is dominated by a sharp-edged projection of the penumbral aperture that is created by a strong, compact X-pinch. However, a secondary, diffuse circle shifted to the right is also visible. This rightward shift in the penumbral image corresponds to a shift along the wire in the IDXP. As such, it seems that an axially extended source is generated even in the best-performing IDXPs. If future experiments determine that smaller A-K gaps can be fielded in an IDXP (e.g., through improved electrode conditioning), it would be interesting to determine if the resulting shorter wires would reduce the prevalence of these axially extended, diffuse sources. Regardless, the X-ray diode data in Figure 4-4, the

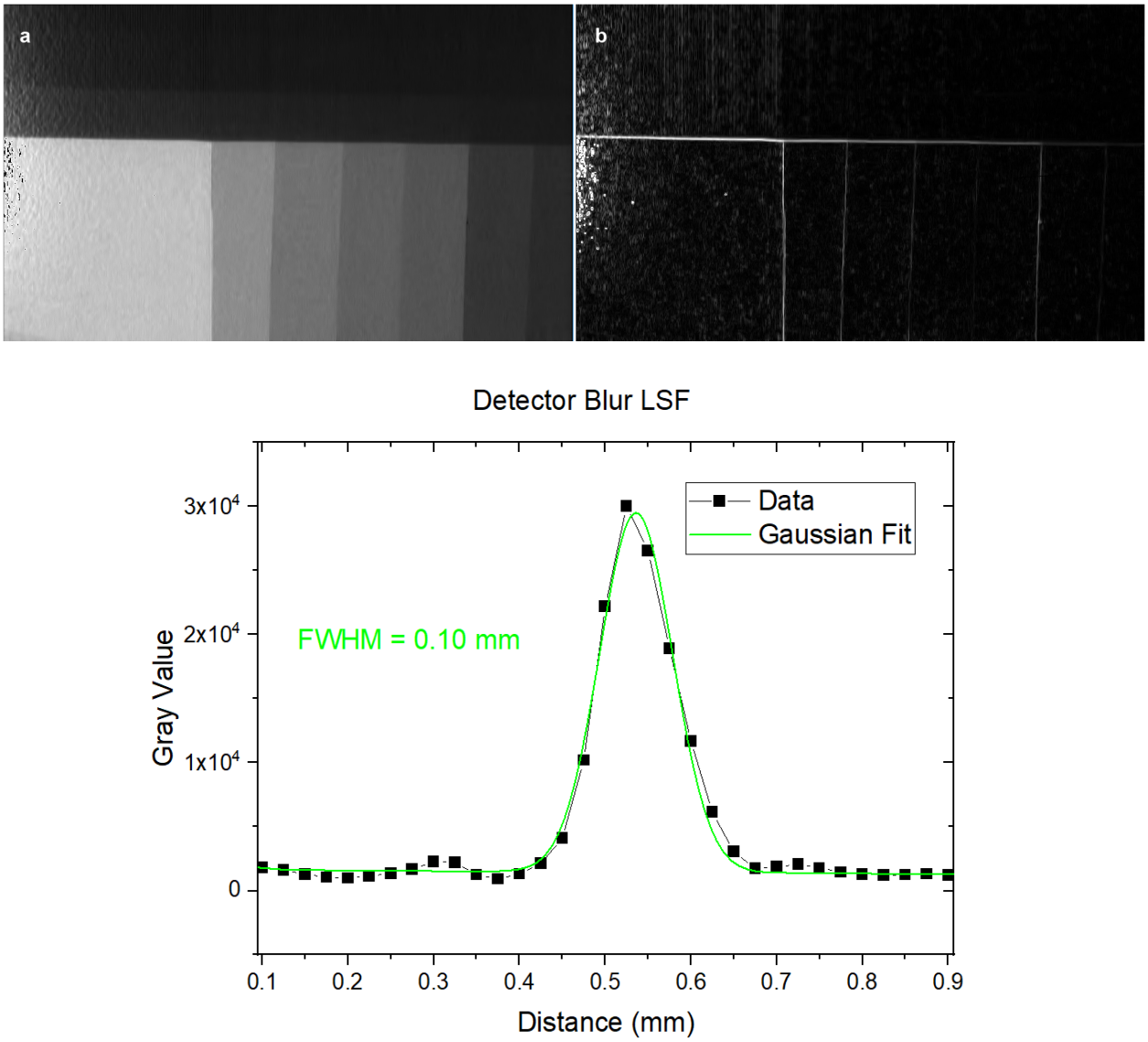

Figure 4-10. *Top: The (a) unprocessed and (b) Sobel-filtered step wedge radiograph from Shot 10862. Bottom: Lineout and fitting of the 10862 step wedge LSF.*

resolution target in Figure 4-7, and the penumbral image in Figure 4-11 all indicate that a backlighter-quality inductively driven X-pinch was generated on Shot 10862.

The Sobel-filtered penumbral image in Figure 4-11b facilitates a measurement of the LSF and therefore the size of the X-pinch source. As shown in Figure 4-12, the FWHM of the LSF is $\sim$100 µm as measured at the detector plane. Since this is effectively identical to the detector blur measurement in Figure 4-10, we can only say that the X-pinch hot spot on this shot is likely to be smaller than the $\sim$10 µm resolution limit of the measurement. The formation of such a compact source is expected based on published X-pinch data [Pikuz et al., 2015a] and represents the realization of one of the key characteristics of X-pinches that makes them so attractive as a diagnostic X-ray source. In summary, Shot 10862 affirmatively answers the question of whether an IDXP can generate a backlighter-quality X-pinch source. Questions remain, however, as to

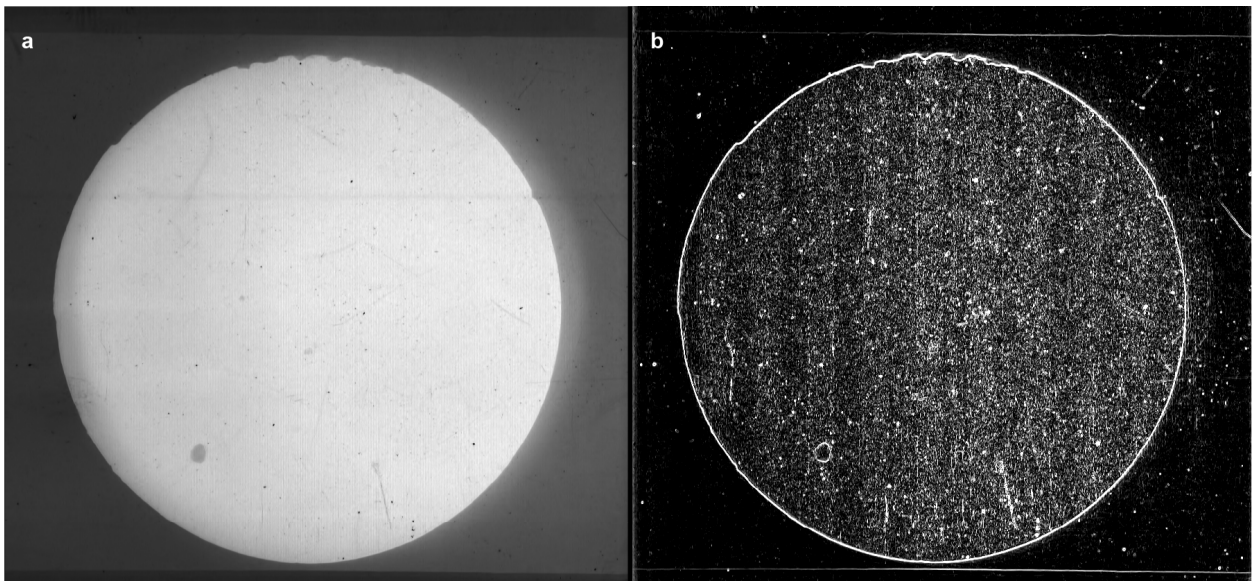

Figure 4-11. *Penumbral imaging from Shot 10862. (a) Raw penumbral image showing the sharp illuminated edge of the penumbral aperture. (b) Sobel-filtered image used to determine the LSF.*

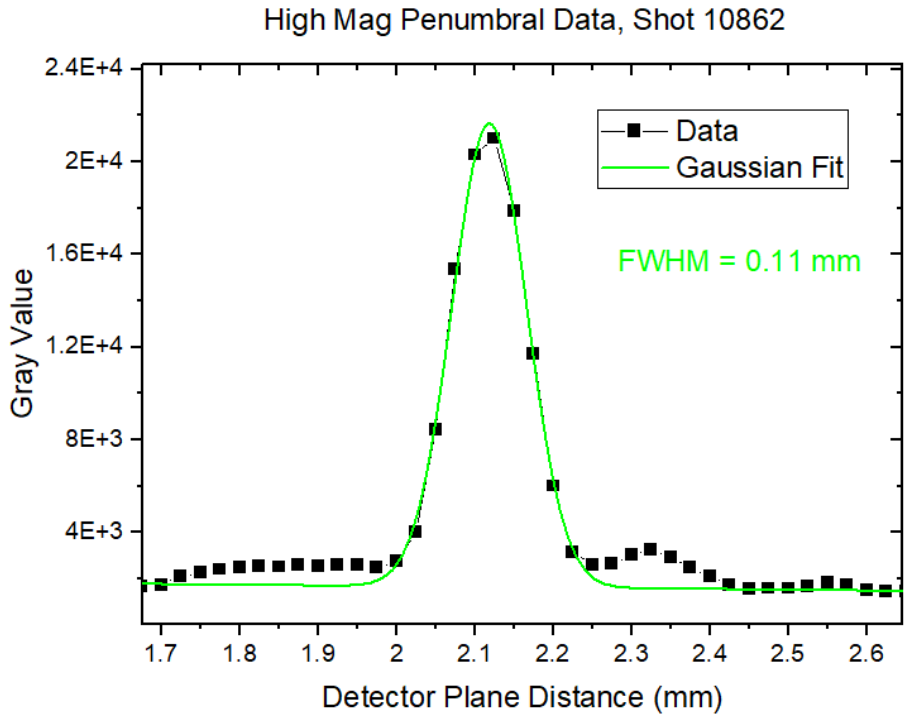

Figure 4-12. *LSF data and Guassian fit as extracted from the Sobel-filtered penumbral image for Shot 10862. The FWHM of the fit essentially matches the* 100 μm *blur of the detector. As such, we conclude that the source size is likely smaller than the detector limit.*

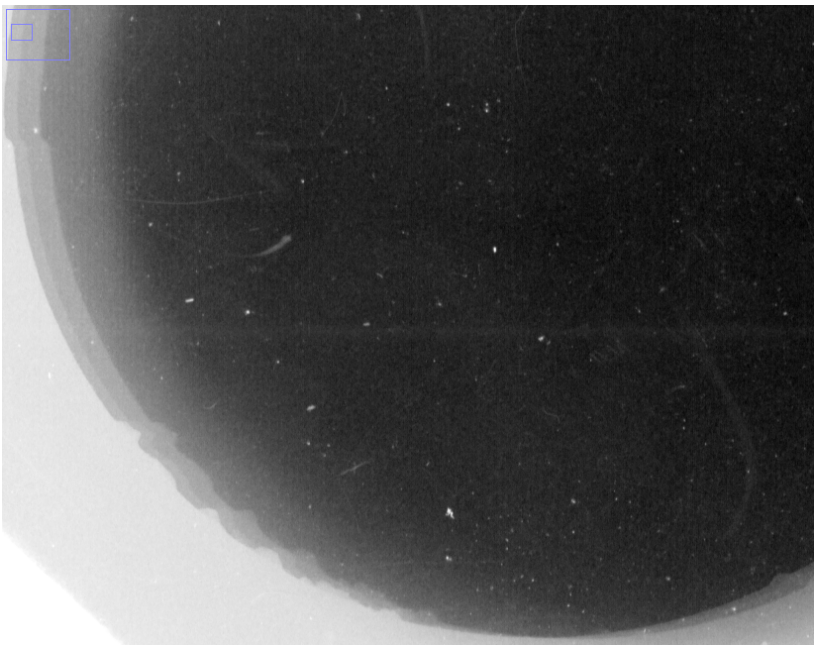

Figure 4-13. *Penumbral image from 10866 showing multiple superposed images of the Mo aperture. Each image is generated by a separate compact X-pinch source that formed along the length of the hybrid X-pinch wire during the experiment. An additional diffuse source is also visible.*

how this behavior can be achieved more reproducibly.

Interestingly there was a second shot, 10866, which generated multiple X-pinches that were each smaller than the resolution limit (i.e., consistent with the spot size measured above). The pinches were spatially separated along the hybrid X-pinch wire, which therefore generated multiple superposed images of the penumbral aperture (see Figure 4-13). Unfortunately, this is not a desirable radiographic phenomenon since overlying images are difficult to separate. Once again, the ability to field smaller A-K gaps would likely remedy this behavior by reducing the wire length over which X-pinch sources can form.

4.3.2. Step wedge radiography

A step wedge consisting of nine stacked layers of aluminum was fielded on all IDXP shots starting with 10837. An orthogonal four-layer copper step wedge was added on top of the aluminum layers starting on 10840. A photo of the step wedge as installed is shown in Figure 4-14 (see Fig 4-2 for further details of the step wedge location). While giving some data on maximum penetrating ability, the copper data will not be included in much of this analysis because of the smaller number of steps and the fact that there was little transmission beyond the third step. It is, however, useful as a background measurement. The entire step wedge is built on top of 20 mils (508 μm) of Kapton which is uniformly present between the step wedge and the image plate just below. The exact details of the step wedge layers are given in Table 4-3. The corresponding transmission curves and penetration scale lengths for the aluminum portion of the step wedge are shown in Figure 4-15. The penetration scale length is the *e*-folding distance for the penetration of

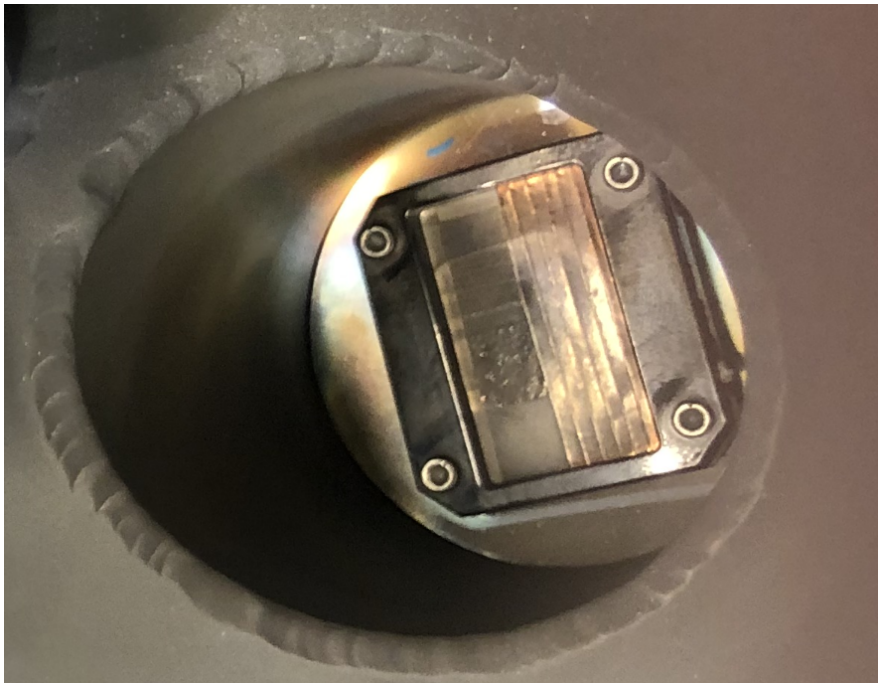

Figure 4-14. *Photo of the aluminum and copper step wedge installed in the chamber.*

Layer	Material	Thickness	Total
0	Kapton	508 µm	
1	Aluminum	12.7 µm	12.7 µm
2	Aluminum	12.7 µm	25.4 µm
3	Aluminum	12.7 µm	38.1 µm
4	Aluminum	12.7 µm	50.8 µm
5	Aluminum	100 µm	150.8 µm
6	Aluminum	100 µm	250.8 µm
7	Aluminum	100 µm	350.8 µm
8	Aluminum	100 µm	450.8 µm
9	Aluminum	100 µm	550.8 µm
10	Copper	76.2 µm	76.2 µm
11	Copper	76.2 µm	152.4 µm
12	Copper	76.2 µm	228.6 µm
13	Copper	76.2 µm	304.8 µm

Table 4-3. *Step wedge composition. Note that the Kapton covers the entire image plate and that the copper steps run orthogonally to the aluminum steps forming a 2D grid of Al/Cu steps.*

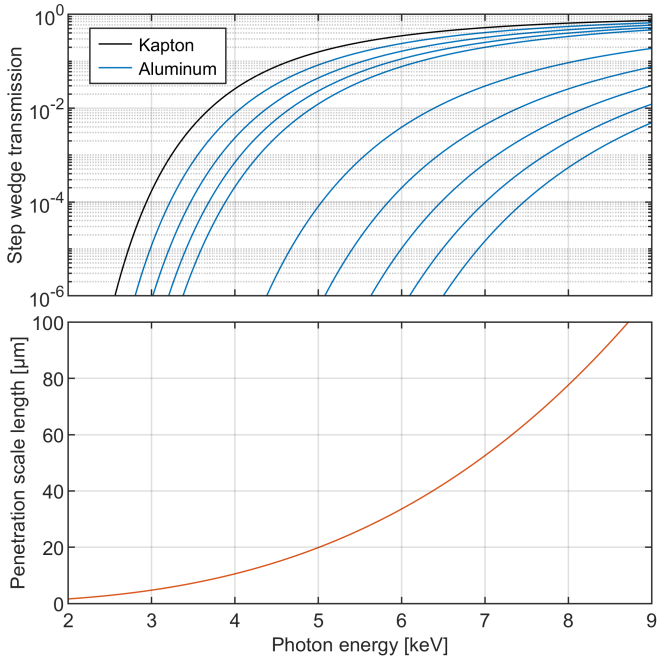

Figure 4-15. *Aluminum step wedge cumulative transmission curves and penetration scale lengths. Underlying data obtained from Henke et al. [1993].*

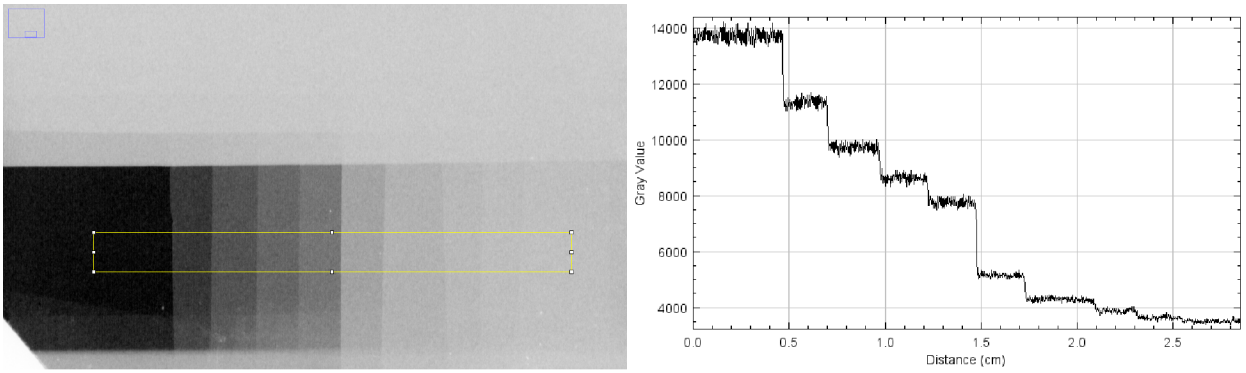

Figure 4-16. *Step wedge radiograph (left) with lineout from within yellow box (right).*

photons of a given energy. The Kapton substrate transmits very few photons ($<3\%$) below 4 keV, so the step wedge is largely insensitive below these energies. Given the thicknesses of the aluminum steps, the penetration scale lengths for >4 keV photons should be well resolved.

A step wedge is a very useful diagnostic in radiography because it allows a direct measurement of the transmission curve, which relates X-ray transmission to areal density (provided that cold opacities are appropriate). Beyond measuring physical features, this is the fundamental measurement one performs in radiography. The transmission curve is an integrated quantity which includes the source X-ray spectrum, detector energy response, and the material areal density. Therefore the transmission curve only offers an indirect view of the source spectrum. We will not attempt to unfold the X-ray spectrum here because, as will be shown, the source consists of multiple types and components so a simple model will not likely be successful.

An example IDXP step wedge radiograph is shown in Figure 4-16. In all the cases included in this analysis, the data values behind each step are very well isolated and measured to high precision (a few percent or better). This is appreciated because in many other radiographic situations, large amounts of blur or non-uniform irradiation result in gradients or non-flat exposures over a step which can introduce large error in the transmission curve.

Figure 4-17 shows the extracted transmission curves for the copper portion of the step wedge. One can see that the curve flattens out very quickly by the third step. There exists an apparently uniform background over the entire step wedge, the source of which has not been identified and the magnitude of which varies from shot to shot. The copper portion of the step wedge provides a measurement of this background for each shot.

The aluminum step wedge, on the other hand, provides more detailed transmission curves that carry information about the X-pinch source. The analysis of the aluminum step wedge data is as follows: The gray values are extracted behind each step and a two-term exponential is fitted to each curve using the following equation:

$$y = y_0 + A_1 e^{-x/t_1} + A_2 e^{-x/t_2} \tag{4.1}$$

An example showing the high-quality of the fit is shown in Figure 4-18. Similar high-quality fits were obtained for all of the shots that will be shown ($R^2 > 0.999$). The fit is especially useful for extracting the background or baseline level which can then be removed. New curves are

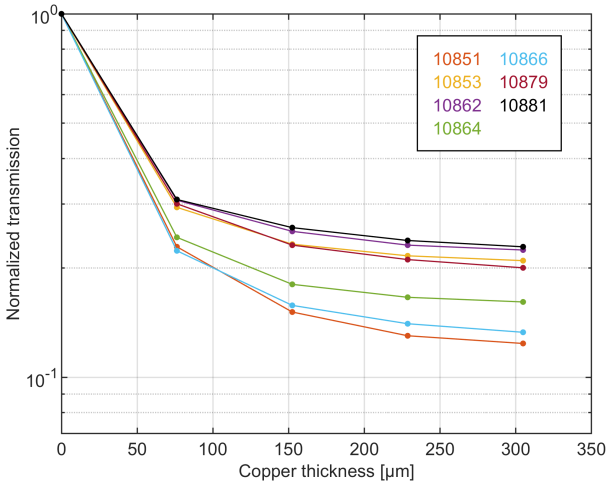

Figure 4-17. *Normalized transmission curves for the copper portion of the step wedge. Note that the background levels have not been subtracted.*

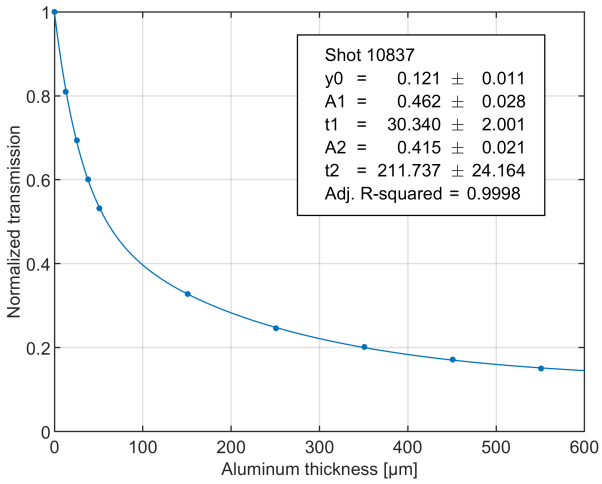

Figure 4-18. *Sample two-term exponential fit to the normalized aluminum step wedge gray values as a function of aluminum thickness.*

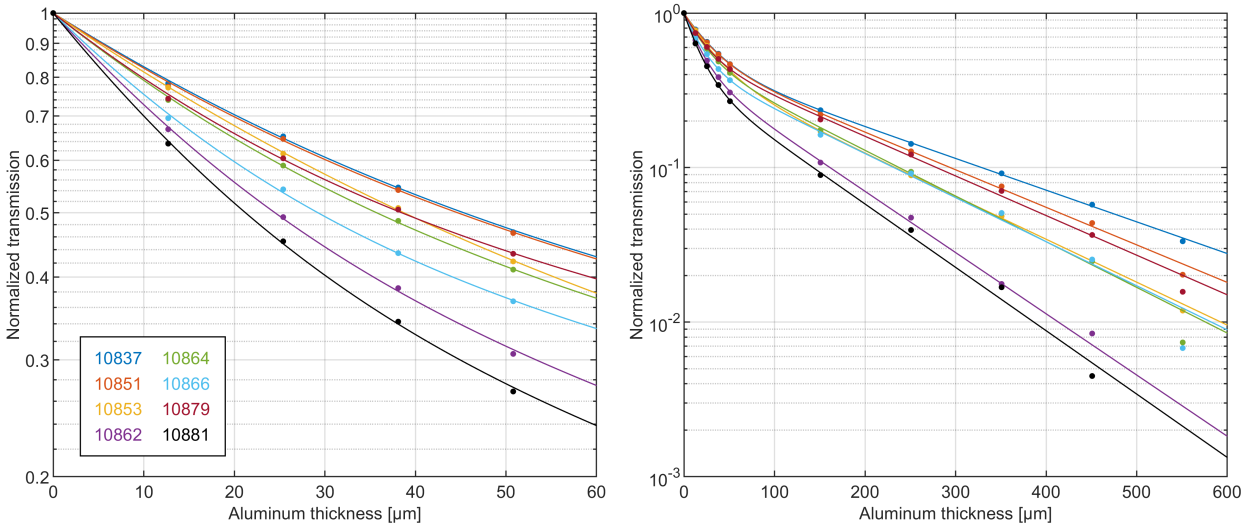

Figure 4-19. *Processed transmission curve data using a two-term exponential fit with background subtracted. The left panel highlights the transmission through the four thin aluminum steps in the step wedge, while the right panel shows the transmission through all nine steps. The three shots where strong pinching occurred (10862, 10866, and 10881) have the softest transmission curves.*

generated and renormalized to give a background-free transmission curve. The results are shown in Figure 4-19, where the left panel shows the transmission through the four thin steps of the step wedge and the right panel shows the transmission through all nine steps. It is evident from the shape of these curves why a two-term exponential provides a meaningful fit to the data.

From Figure 4-19 it is clear that there is significant shot-to-shot variation in the X-ray spectrum even after the background levels have been removed. However, one pattern does quickly emerge. For the three shots where strong pinching occurred from a radiographic perspective (10862,

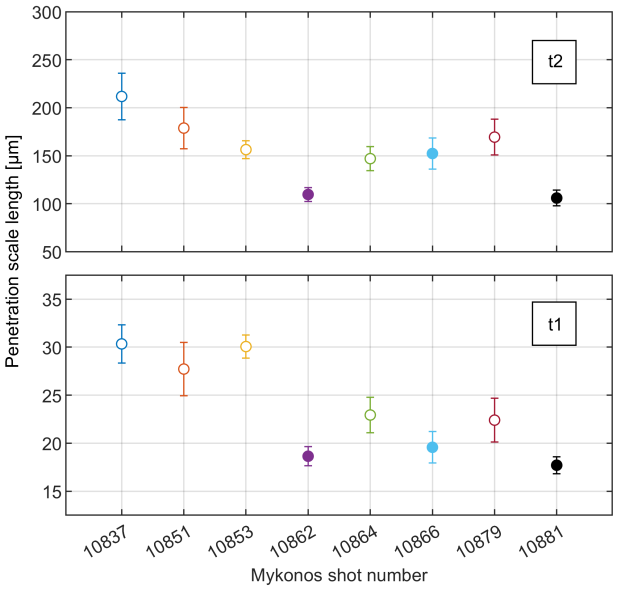

Figure 4-20. *Exponential scale factors t_1 and t_2 according to Equation 4.1 plotted against shot number. The shots with filled circles, 10862, 10866, and 10881, show strong pinching on the radiographic diagnostics.*

10866, and 10881), the spectrum is notably softer than on the other shots (i.e., the transmission tapers off more quickly). To examine this more quantitatively, Figure 4-20 plots the fitted penetration scale lengths t_1 and t_2 from the two-term exponential fit (Equation 4.1). These parameters relate the material thickness to a rate of change of transmission. The penetration scale lengths can be associated with an approximate photon energy via the curve shown in the bottom half of Figure 4-15. The shorter the penetration scale length, the softer the spectrum.

As Figure 4-20 shows, the two-term exponential fit reveals the existence of two highly disparate penetration scale lengths in the step wedge transmission curves. We associate the first of these two penetration scale lengths with the desirable, small-scale X-pinch hot spot (t_1) and the other penetration scale length with a harder, extended source (t_2) that is typically thin in the radial direction but elongated in the axial direction (along the direction of the wire). In some cases, the X-pinch hot spot was barely measurable but the extended source remains. From the data in Figure 4-20, a most interesting trend emerges. In the three shots with strongest pinching (filled circles), the t_1 penetration scale length is minimized at a value of $t_1 \sim 20$. If we compare this value to the curve shown in the bottom half of Figure 4-15 we find that $t_1 \sim 20$ is associated with a photon energy of $\sim$5 keV. Given that the step wedge transmits very few photons below $\sim$4 keV and a Mo X-pinch is expected to generate a continuum of 3–8 keV photons [Shelkovenko et al., 2001], the fact that the transmission curve is centered around 5 keV is fully consistent with the formation of the expected X-pinch hot spot.

In this chapter we have shown that the IDXP concept is capable of generating a radiography-quality X-ray burst from a sub-10 μm hot spot. While questions remain about the reproducibility of the X-pinch source, both with respect to its intensity and its timing within the current pulse, the fundamental question of whether a low-impedance driver such as an IDTL can power a backlighter-quality X-pinch has been definitively answered.

5. DEVELOPMENT OF AN EXTENDED CONVOLUTE POST FOR X-PINCH RADIOGRAPHY

While the inductively driven transmission line (IDTL) is the first X-pinch concept to be conceived that can be non-perturbatively fielded as part of the Z load hardware, an alternate method of driving an X-pinch with the potential for higher peak current ($\sim$1 MA) would be desirable for several reasons: Increased current will improve radiated energy in a given photon energy range and may enable higher photon energy sources through higher-atomic-number X-pinch materials. Additionally, increased current may provide some flexibility in terms of delaying the X-pinch timing. Development of an Extended Convolute Post (XCP) to drive an X-pinch is underway.

Extended convolute post geometry

The Z machine utilizes a double post-hole convolute to combine the currents from four self-magnetically insulated transmission lines into a single final transmission line, which supplies current to the load. The convolute geometry consists of posts that connect three anodes through holes in two cathodes (see Figure 5-1) with a twelve-fold azimuthal symmetry. The upper extent of each convolute post therefore carries current from the three lower transmission lines. Typically, the Z machine delivers approximately 20–28 MA of current to the load, with roughly one quarter of the current flowing through each of the outer transmission lines. As a result, each of the upper convolute posts carries roughly $1/12$ of $3/4$ of the load current, or 1.25–1.75 MA.

The extended convolute post (XCP) has been proposed as a method to drive an X-pinch with up to 1 MA of current. In the XCP geometry (see Figure 5-2), an upper convolute post extends up through a hole in the upper anode and a return current can is used to connect the post back down to the top anode. This geometry allows a secondary load, such as an X-pinch, to be connected in series with the main load (i.e., the current flowing through the XCP subsequently flows through the load as well). Note that this is a key difference from the IDXP, which is inductively coupled in parallel to the load rather than electrically coupled in series.

A consequence of the XCP geometry is that the inductance of that post is increased relative to the other convolute posts, which will reduce the current flowing through that post and increase the current flowing through the non-extended posts. The inductance of the upper convolute posts is collectively 0.5 nH [Pointon, 2008], so each individual post has an inductance of approximately 6 nH. Maintaining the same post diameter (15.875 mm), using a 4 mm anode-cathode gap in the extension, and extending the post by 65 mm adds an additional 5.3 nH to the post.

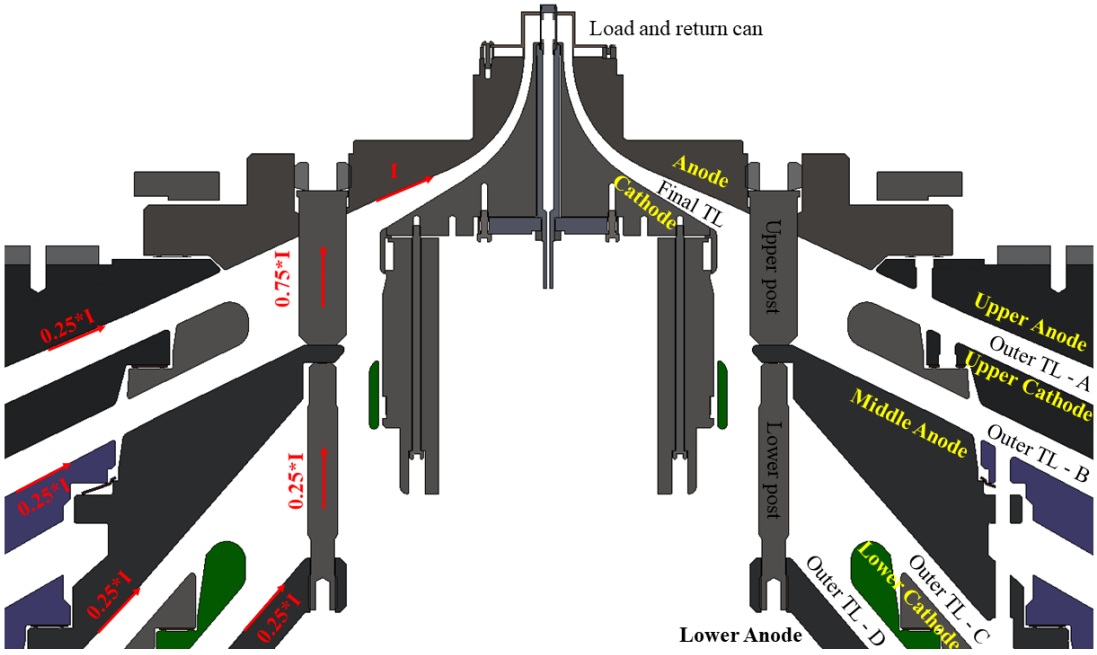

Figure 5-1. *An R-Z slice through a solid model of the Z-Machine double post-hole convolute. On the left, red arrows indicate the approximate distribution of current, with roughly 25% of the current flowing through each of the four outer transmission lines. Only the bottom transmission line passes current through the lower convolute posts, and all but the top transmission line pass current through the upper convolute posts. The total current (ignoring losses) is transmitted through the final transmission line to the load. On the right, the anodes, cathodes, convolute posts, and transmission lines are labeled.*

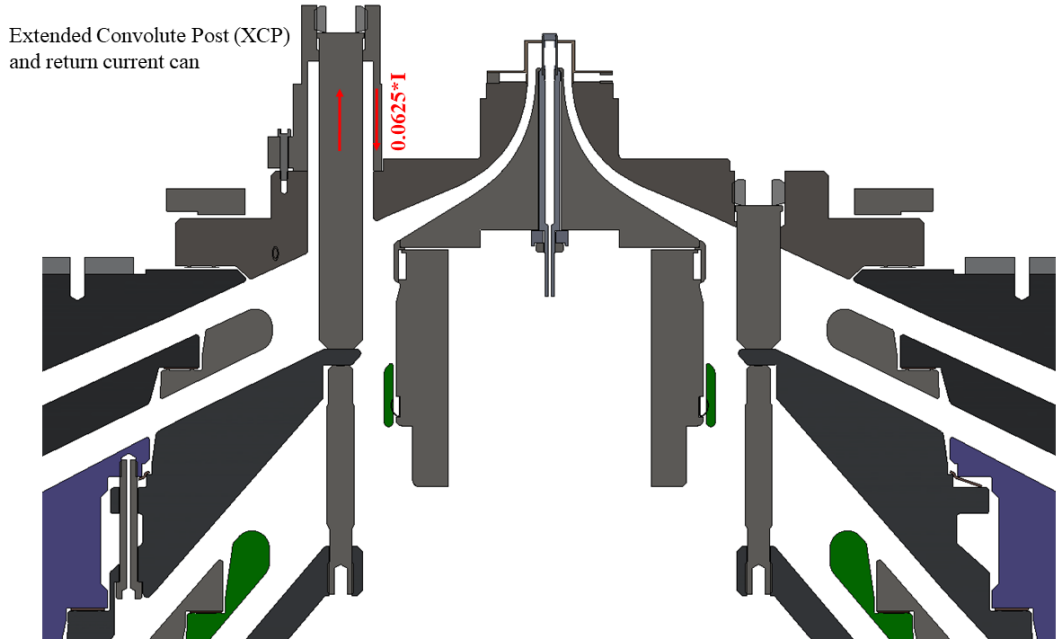

Figure 5-2. *An R-Z slice through a solid model of the Z-Machine double post-hole convolute with an extended convolute post (shown on the left). Red arrows on the extended convolute post show the current path, with roughly* $1/16$ *of the total current flowing through the extended post before being transmitted through the final transmission line to the main load.*

A rough estimate on the current through the XCP can be made by ignoring the other inductances in the system. The XCP is assumed to have an inductance of 11.3 nH and the other 11 posts are assumed to have an inductance of 6 nH each. The collective inductance of the upper convolute posts increases from 0.5 to 0.52 nH. For reference, the typical inductance of the final transmission line and load is between 2.5 and 7 nH, so this 0.02 nH change is expected to have a negligible impact on the current delivered to the load. Assuming a 24 MA current and an even split between the four outer transmission lines, each post nominally carries 1.5 MA. With the XCP, the current through the non-extended posts would increase to 1.56 MA and the current through the extended post would decrease to 0.83 MA. Note that to conduct 0.83 MA with a 100 ns rise time through 5.3 nH, the driving voltage only needs to be ~44 kV, which would put an electric field of only 110 kV/cm across the A-K gap.

Experimentally evaluating the extended convolute post

The XCP has been tested on two Z experiments: z3442 (Helical Instability) and z3464 (Dynamic Screw Pinch). In both experiments, the XCP was configured as a short circuit with a pair of B-dot monitors to measure the current flowing through the post. An example of the current flowing through the post is shown in Figure 5-3. In this experiment, the peak load current was 15.3 MA, and the XCP current was 0.9 MA, or roughly 1/16 of the load current.

An X-pinch load has been designed for use with the XCP and is scheduled to be tested on Z for the first time in December 2020. The objective of this test is to obtain an early-time radiograph of the target imploding. The system will be fielded in a point projection configuration with a modified version of the time-integrated pinhole diagnostic [McPherson et al., 2016] as the

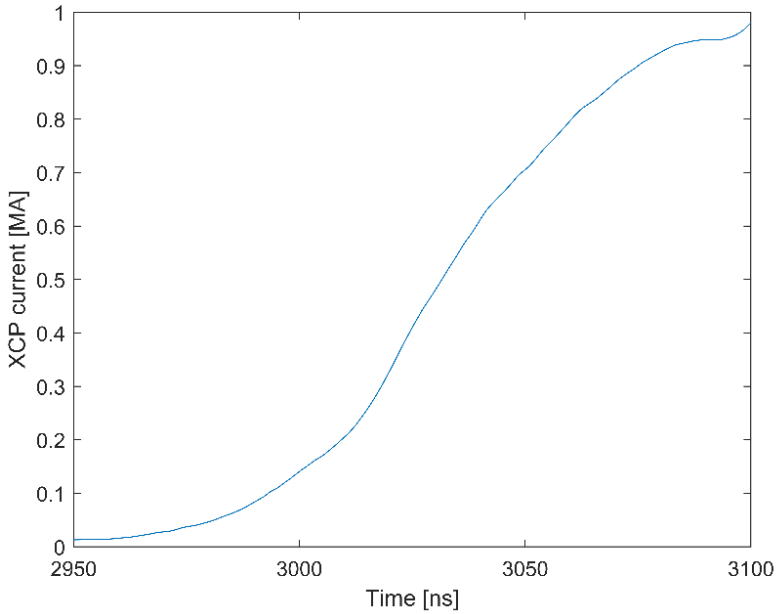

Figure 5-3. *The current measured on z3664 by the B-dot monitors located on the XCP.*

detector housing, with the detector located roughly 38 cm from the load creating a 6x magnification radiograph.

The design for the X-pinch is based on a configuration tested previously [Hoyt, 2015] on the 1 MA COBRA accelerator at Cornell. Those tests used a hybrid X-pinch with a 140 μm diameter titanium wire and a drive current of ∼0.7 MA to produce ∼2 J of Ti k-shell radiation (∼4.75 keV). Assuming similar X-pinch performance, the XCP will produce 2.6×10^{15} k-shell photons. The resolution element on the detector are 15 μm × 15 μm, so they occupy a solid angle of 8.6×10^{-11} sr. Typically, in chamber diagnostics in Z mitigate debris with 1.5 mm of Kapton, which has a transmission of 0.14% at 4.75 keV. As a result, roughly 310 photons per pixel are expected at the detector (note that reducing the debris mitigation to 1 mm of Kapton would increase this to roughly 3400 photons per pixel). For comparison, the 6.1 keV spherically-bent crystal imaging system used with the ZBL backlighter [Sinars et al., 2004] produces roughly 450 photons per 15 μm × 15 μm pixel [Schollmeier et al., 2017].

Future improvements to the extended convolute post X-pinch

X-pinches driven in series with the load are limited in their utility by the fact that they typically need to emit during the rise of the current pulse, and typically the majority of the interesting load dynamics occur after peak current on the Z machine. One method by which the X-pinch timing might be delayed is to use a wire array as a current switch [Burdiak et al., 2015]. Conceptually, the wire array would draw most of the current early in the pulse due to its relatively low inductance compared to the X-pinch. As the wire array moves under the $\mathbf{j} \times \mathbf{B}$ force, its inductance increases, driving more of the current through the X-pinch. This may allow the current flowing through the X-pinch to still be rising while the total current through the XCP is falling.

Another exciting possibility with an XCP X-pinch source is radiographic tomography of the load. The present radiographic capability on the Z facility has a fixed azimuthal position, so the two frames must come from approximately the same line of sight. Clearly this is beneficial in understanding the time evolution of a specific feature, but it limits diagnosis of the 3D nature of the implosions.

Given the twelve-fold azimuthal symmetry of the convolute, radiographs could be obtained at 30° steps around the target with XCP X-pinches. The impact of replacing convolute posts with additional XCPs on the system inductance and currents is documented in Table 5-1. Somewhat counterintuitively, in this simple model, fielding more XCPs results in an increase in the current through the standard posts as well as through the XCPs, but since the number of posts with a lower current is increasing, the total current through the convolute remains the same. With a fixed X-pinch wire diameter, multiple XCP X-pinches would emit at approximately the same time, resulting in nearly simultaneous images of the target from multiple angles. This would enable a tomographic reconstruction of the target. Alternatively, fielding different wire materials with appropriately chosen diameters could enable nearly simultaneous radiographs at different photon energies, albeit from different lines of sight. Another interesting option would be to use different X-pinch wire diameter of the same material to produce a time-sequence of the implosion, again from different lines of sight, as in Douglass and Hammer [2008].

Number of XCPs	Inductance of upper convolute posts [nH]	Current through standard posts [MA]	Current through XCPs [MA]
1	0.520	1.56	0.83
2	0.542	1.63	0.86
3	0.566	1.70	0.90
4	0.593	1.78	0.94

Table 5-1. *A rough approximation of the total inductance of the upper convolute posts, the current through the standard posts, and the current through the extended convolute posts as a function of the number of XCPs fielded. These calculations assume a total current of* 24 MA*, which is equally distributed between the four outer transmission lines. Losses are assumed to be negligible and the total current is assumed to be fixed despite the small increase in total inductance due to the XCPs.*

6. DEVELOPMENT OF IDTL-BASED INNER-MITL CURRENT MONITORS

While this report has focused extensively on high-current inductively driven transmission lines (IDTLs) that are designed to power diagnostic X-ray sources, we have also discovered that lower-current IDTLs can serve as high-fidelity inner MITL (magnetically insulated transmission line) current monitors. This stems from the fact that the IDTL current is in-phase with the generator current (see Section 2.1). As such, if the current coupling to the IDTL is truly lossless, then the B-dots in the IDTL can be used to measure the generator current. As was first mentioned in Section 2.2, a key feature of the B-dot voltage waveforms produced by IDTLs is that they are substantially cleaner than those from standard B-dots. In particular, they are largely free of insidious high-frequency oscillations that often pollute the standard B-dot signals (see Figure 2-3). The working hypothesis is that the B-dot sensors embedded in the IDTL are more protected from the harsh plasma and radiation environment in the inner MITL than are the standard B-dot sensors. As such, if we can design an IDTL that exhibits truly lossless current coupling, we may be able to produce a better inner-MITL current monitor than presently exists on Z.

A key aspect of developing a lossless IDTL was to iterate the design and compare the results to current measurements from various locations in the system. What we found was that it was necessary to grow the minimum A-K gaps in the IDTLs rather substantially to ensure lossless current coupling. Figure 6-1 shows three generations of IDTL current monitors. Between each generation we increased the minimum A-K gap first by one millimeter and then by an additional two millimeters. We also simplified the design as much as possible by terminating the drive loop horizontally into the side of the IDTL body rather than having it hook back upward. The third

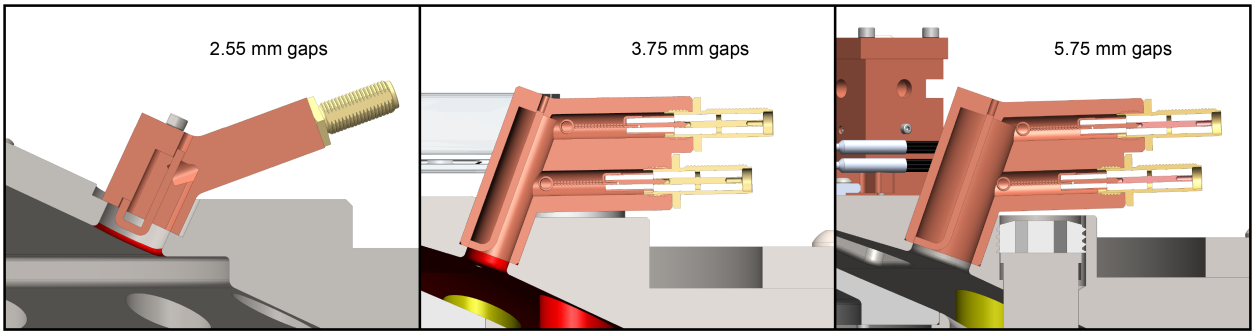

Figure 6-1. *Three generations of IDTL current monitors. Between each generation, the minimum A-K gap size was increased. The design was also streamlined such that the drive loop terminates horizontally into the side of the IDTL body.*

generation design with 5.75 mm gaps that is shown on the right in Figure 6-1 is the present workhorse IDTL current monitor that is routinely fielded on Z. More details on the early phases of IDTL current monitor development are available in Myers et al. [2018].

We now present data from several different Z experiments with a range of load inductances to illustrate the challenge of making inner-MITL current measurements and to show the promise of both IDTLs and XCPs as alternate inner-MITL current monitors. Figure 6-2 shows the location of the inner MITL within the final $\sim$15 cm of power flow hardware on Z. Since current can be lost in both the convolute (green) and in the inner MITL (yellow) [Hutsel et al., 2018], it is crucial to separately measure the current that makes it through to the inner MITL and then on to the load region (red). The latter is accomplished using load current velocimetry techniques [Porwitzky and Brown, 2018] that are beyond the scope of this report. Inner MITL measurements, on the other hand, are acquired using the standard B-dot sensors shown on the left side of Figure 6-2. In each standard sensor, a two-turn wire loop is suspended inside an azimuthally localized pocket in the anode. As described in Section 2.2, these sensors are calibrated on a test stand such that each raw signal can be integrated to obtain a current waveform [Wagoner et al., 2008].

The challenge of measuring the inner MITL current on Z can be separated into "cold" and "warm" effects. Cold effects such as calibration anomalies are present regardless of the strength of the current, while warm effects such as particle bombardment and radiation occur only in the harsh power flow environment created at $>$20 MA on Z. Figure 6-3 illustrates the range of cold and warm effects that are routinely observed on Z inner MITL B-dot signals. The first column shows data from a lossless, short-circuit experiment. The recorded inner MITL B-dot signal is clean (top), but the corresponding integrated current waveform unphysically overshoots the available generator current by 1.7 MA or $\sim$7% (bottom). Note that the generator current is measured by electrical sensors embedded in the vacuum insulator stack at a radius of $\sim$1.7 m [Wagoner et al., 2008]. The specific generator current waveform plotted here is the stack current translated losslessly through the outer MITLs to the outer edge of the convolute [Jennings et al., 2010]. The source of the presumed measurement error that causes the inner-MITL measurements to overshoot the available generator current—an effect that has been consistently observed across many Z experiments [Gomez et al., 2017]—has not been identified.

On imploding physics experiments where the inductance inside of the convolute is necessarily higher, warm effects meaningfully impact the inner MITL B-dot signals. The middle column of Figure 6-3 shows the performance of a standard B-dot sensor on a moderate-inductance experiment. Here, the raw signal (top/yellow) exhibits strong oscillations that can poison the integrated current waveform. These oscillations are observed during nearly every short-pulse experiment on Z. The inner MITL current in this example (bottom/yellow) runs under the available generator current (blue), but it also runs unphysically below the velocimetry-based load current (red). This suggests that warm effects cause the standard B-dot sensor to undershoot rather than overshoot its expected current. Finally, the third column in Figure 6-3 shows the performance of a standard B-dot sensor in a high-inductance experiment. The raw signal exhibits wild oscillations and cuts out early. The resulting current waveform fails to track even the shape of the generator current or the load current. Given the overshoot observed on low-inductance experiments and the undershoot observed on higher-inductance experiments, more resilient

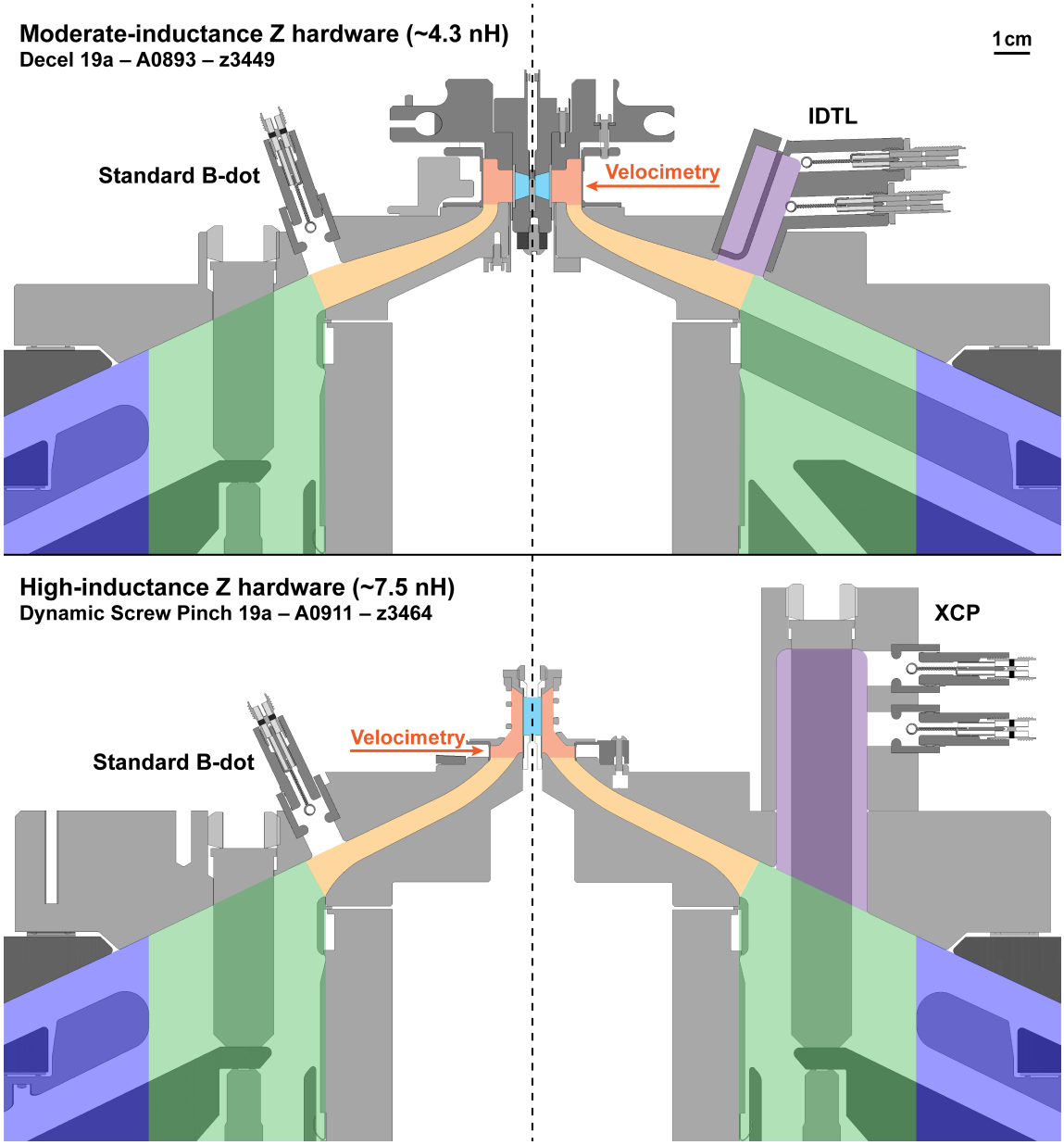

Figure 6-2. *Two examples of Z load hardware and current diagnostics. Four different power flow regions are highlighted: (1/blue) the outer MITLs where Z's current is distributed across four parallel levels (only the top two are visible here); (2/green) the 3D convolute region where the parallel outer MITL currents are combined; (3/yellow) the inner MITL, which carries the combined current from the convolute to the load; and (4/red) the load region where megabar magnetic pressures implode targets of interest (light blue). The left half of each hardware set shows a standard inner-MITL B-dot sensor where a loop of wire is suspended inside a pocket in the anode. The right half of the figure shows two developmental inner-MITL B-dot sensors. In the top panel, an inductively driven transmission line (IDTL) uses an L-shaped wire to draw a small amount of current up into a secondary cavity (purple) where two B-dot loops measure the current. In the bottom panel, an extended convolute post (XCP) carries ~6% of the total Z current up into a protected cavity (purple) where two standard B-dot sensors measure the current. Finally, each hardware set includes load current velocimetry diagnostics that measure the velocity of a magnetically driven flyer plate in order to infer the load current delivered to within* $\sim$1 cm *of the target [Porwitzky and Brown, 2018].*

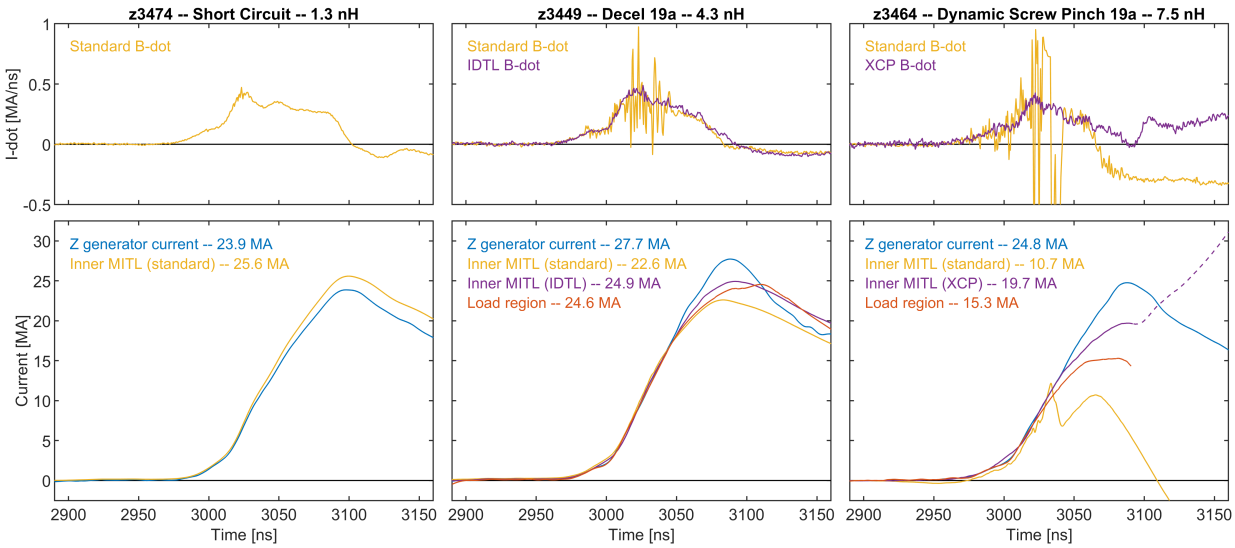

Figure 6-3. *Inner MITL B-dot data from Z experiments with low, moderate, and high inductance. Each column plots the raw B-dot signals (top) and integrated current waveforms (bottom) from a single Z experiment. For each experiment, the inner MITL current waveforms (yellow) are compared to the available generator current (blue) and, where possible, the velocimetry-based load current (red). Signals from two recently developed inner MITL B-dot sensors (the IDTL and the XCP) are shown in purple the middle and right experiments, respectively. See the text for further details.*

inner-MITL current monitors would greatly improve our ability to quantify driver-target coupling across a wide range of Z experiments.

The final set of information in Figure 6-3 shows the inner MITL current measurements from the two alternate current monitors developed as part of this project: IDTLs and XCPs. The IDTL and XCP signals are shown in purple in the middle and right columns of Figure 6-3, respectively. Each of these current monitors draw a small amount of current into a secondary cavity to allow more protected B-dot sensors to measure the magnetic field (see Figure 6-2 for the sensor geometries). Both types of sensors produce substantially cleaner raw signals, and their integrated current waveforms remain causal with respect to the generator and load currents. These results demonstrate that changes to the current monitor geometry can substantially improve inner MITL B-dot sensor performance.

In total, nearly 100 IDTLs have been fielded on Z, including roughly a dozen of the third-generation IDTL current monitor design shown in Figure 6-1. We are actively working to assemble a large data set of IDTL measurements spanning a range of load inductances and inner MITL geometries that will ultimately facilitate a definitive assessment of the utility of IDTLs as inner-MITL current monitors. We also note that the inner-MITL current monitor results presented in this section helped to motivate an LDRD proposal that was submitted to the Assured Survivability and Agility for Pulsed Power (ASAP) Mission Campaign in FY20.

7. ANTICIPATED OUTCOMES AND IMPACTS

During this project we achieved three key experimental objectives that each advanced the technical readiness of the inductively driven X-pinch (IDXP) concept:

1. We demonstrated the non-perturbative coupling of more than 200 kA of current to short-circuit inductively driven transmission lines (IDTLs) on Z. This amount of IDTL current is sufficient to drive a diagnostic X-ray source such as an X-pinch. See Chapter 2 for details.
2. We demonstrated comparable current coupling ($\sim$150 kA) to Z-surrogate short-circuit IDTLs on Mykonos. Note that the difference in coupled current between Mykonos and Z arises from a difference in the self inductance of the respective IDTL designs. The magnetic energy coupled to the IDTL in each case is nearly identical ($\sim$300 J). See Chapter 3 for details.
3. Using the same Z-surrogate Mykonos IDTL platform, we demonstrated that an inductively driven hybrid molybdenum X-pinch can generate a radiography-quality X-ray burst that emanates from a sub-10 μm hot spot. To our knowledge, this is the first demonstration that a low-impedance driver like an IDTL can power an X-pinch. See Chapter 4 for details.

We believe that these achievements have advanced the technology readiness level (TRL) [Mitchell, 2007] of the IDXP concept from TRL 2 (concept formulated) to TRL 4 (key elements demonstrated in laboratory environment).

In spite of the tremendous progress made on the IDXP concept during this project, substantial hurdles remain before the IDXP can become a production diagnostic that is routinely fielded on Z. These hurdles can be summarized as a series of open questions:

1. Does the IDXP source still function when transferred from Mykonos to Z?
2. Does the IDXP generate enough X-ray fluence to achieve acceptable signal-to-noise with the heavy detector filtration that is required on Z?
3. Is the intensity of the IDXP source reproducible enough to be relied up for Z experiments? Can it be improved?
4. Is the timing of the IDXP source reproducible enough to be relied upon for Z experiments? Can it be improved?

These questions could be answered through additional IDXP experiments both on Mykonos and on Z. The key function of additional Mykonos experiments would be to hone the IDXP source by

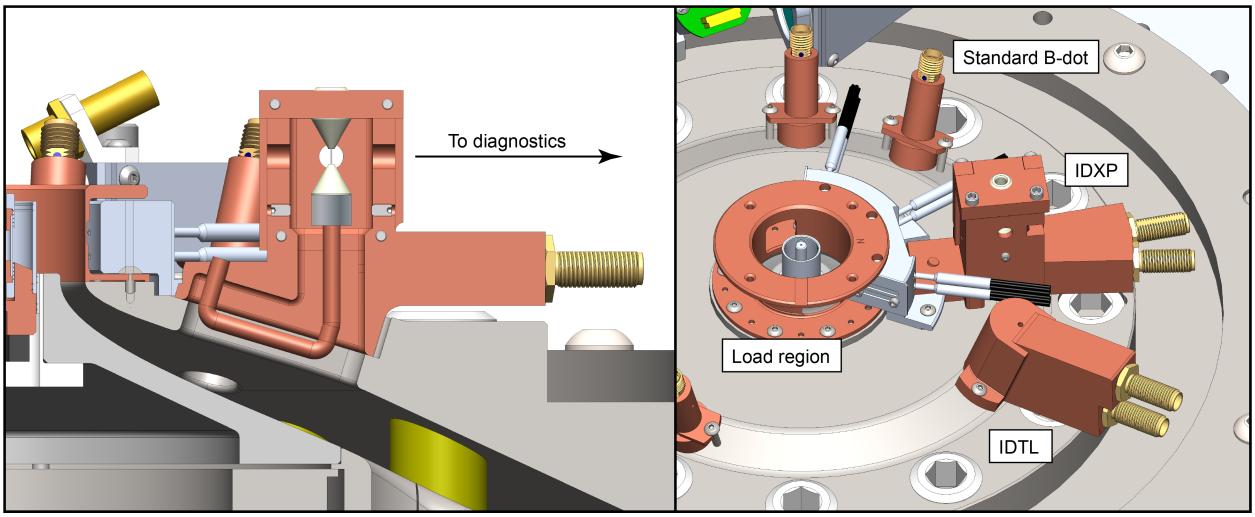

Figure 7-1. *Schematic of first IDXP ride-along experiment on Z. The left image shows that the lower portion of the IDXP including the drive loop resembles the high-current IDTLs described in Chapter 2, while the upper hybrid X-pinch portion of the IDXP is nearly identical to the Mykonos configuration described in Chapter 4. The right image shows the location of the IDXP relative to the load and to an IDTL-based current monitor.*

better quantifying its reproducibility and by testing, for example, improved electrode conditioning protocols. These experiments could also seek to quantify the IDXP source photometrics by pursuing additional X-ray diagnostics such as an X-ray spectrometer. The Z experiments, on the other hand, would focus on *in situ* characterization of the performance of the IDXP source. Fortunately, the first IDXP ride-along experiment on Z has already been designed and procured as part of this project.

Figure 7-1 shows a schematic of the first IDXP designed for Z. The lower portion of the IDXP including the shape of the drive loop is modeled after the successful high-current IDTL experiments on Z that were presented in Chapter 2. Note that, as on Mykonos, the minimum A-K gap has been expanded from 3 mm to 3.3 mm relative to the original high-current IDTL experiments on Z. The upper portion of the IDXP is nearly identical to the successful Mykonos hybrid X-pinch design described in Chapter 4.

Rather than attempting to generate an image through the load region with this first test, the X-rays produced by the IDXP source will be viewed by two X-ray diagnostics located directly behind the IDXP. The first is a set of three silicon X-ray diodes fielded in the tungsten housing of a time-integrated pinhole camera (TIPC) [McPherson et al., 2016]. As on Mykonos, these diodes will record the IDXP X-ray pulse. The second X-ray diagnostic is a second TIPC housing configured to image a pinhole array onto an image plate. While this measurement will be acquired at low magnification, it will provide an initial test of whether the IDXP source can backlight pinholes in the Z environment. The experiment on which this first IDXP ride-along will be fielded is not presently scheduled, but we hope to see it fielded soon.

In addition to the rapid development of the IDXP concept, this project supported the development of multiple spinoff concepts including the extended convolute post (XCP) and IDTL-based

current monitors. The XCP is particularly exciting because it generates substantially more secondary load current than IDTLs and therefore offers more flexibility in how one times and configures the X-pinch load. Since we have successfully demonstrated that the XCP carries nearly 1 MA of current, it has been advanced from TRL 0 (idea) to TRL 3 (concepts demonstrated analytically or experimentally) during this project. An XCP with an X-pinch included will be fielded for the first time in the coming months. See Chapter 5 for details.

Finally, the development of IDTL-based current monitors was also substantially advanced during this project. As described in Chapter 6, the wide-bore IDTL design that was first fielded midway through this project has routinely generated inner-MITL current measurements of higher fidelity than the standard inner-MITL B-dot sensors that are fielded on Z. This work led to the development and submission of a follow-on LDRD proposal to the Assured Survivability and Agility for Pulsed Power (ASAP) Mission Campaign in FY20. While not ultimately funded, this proposal helped to flesh out the challenges facing inner-MITL current measurements on Z and the key role that IDTLs and even XCPs might play in resolving these issues. Given that the development of the IDTL current monitor concept began under a previous project [Myers et al., 2018], we assess that the technology readiness of this concept was advanced from TRL 4 (key elements demonstrated in laboratory environment) to TRL 5 (key elements demonstrated in relevant environments) during this project.

REFERENCES

T. Ao, M. Schollmeier, P. Kalita, P. D. Gard, I. C. Smith, J. E. Shores, C. S. Speas, and C. T. Seagle. A spherical crystal diffraction imager for Sandia's Z Pulsed Power Facility. *Rev. Sci. Instr.*, 91(4):043106, 2020. doi:10.1063/1.5132323.

T. J. Awe, R. D. McBride, C. A. Jennings, D. C. Lamppa, M. R. Martin, D. C. Rovang, S. A. Slutz, M. E. Cuneo, A. C. Owen, D. B. Sinars, K. Tomlinson, M. R. Gomez, S. B. Hansen, M. C. Herrmann, J. L. McKenney, C. Nakhleh, G. K. Robertson, G. A. Rochau, M. E. Savage, D. G. Schroen, and W. A. Stygar. Observations of modified three-dimensional instability structure for imploding z-pinch liners that are premagnetized with an axial field. *Phys. Rev. Lett.*, 111:235005, 2013. doi:10.1103/PhysRevLett.111.235005.

F. N. Beg, K. Krushelnick, P. Lichtsteiner, A. Meakins, A. Kennedy, N. Kajumba, G. Burt, and A. E. Dangor. Table-top X-pinch for x-ray radiography. *Appl. Phys. Lett.*, 82(25):4602–4604, 2003. doi:10.1063/1.1584782.

F. N. Beg, R. B. Stephens, H.-W. Xu, D. Haas, S. Eddinger, G. Tynan, E. Shipton, B. DeBono, and K. Wagshal. Compact X-pinch based point x-ray source for phase contrast imaging of inertial confinement fusion capsules. *Appl. Phys. Lett.*, 89(10):101502, 2006. doi:10.1063/1.2335959.

G. C. Burdiak, S. V. Lebedev, A. J. Harvey-Thompson, G. N. Hall, G. F. Swadling, F. Suzuki-Vidal, E. Khoory, S. N. Bland, L. Pickworth, P. de Grouchy, J. Skidmore, L. Suttle, and E. M. Waisman. Characterisation of the current switch mechanism in two-stage wire array Z-pinches. *Phys. Plasmas*, 22(11):112710, 2015. doi:10.1063/1.4936278.

G. W. Collins, M. P. Valdivia, T. O. Zick, J. Kim, D. M. Haas, A. C. Forsman, R. B. Stephens, and F. N. Beg. Investigation into the dynamics of laser-cut foil X-pinches and their potential use for high repetition rate operation. *Appl. Phys. Lett.*, 105(2):024101, 2014. doi:10.1063/1.4889748.

J. D. Douglass and D. A. Hammer. COBRA-STAR, a five frame point-projection x-ray imaging system for 1MA scale wire-array Z pinches. *Rev. Sci. Instr.*, 79(3):033503, 2008. doi:10.1063/1.2884707.

Edmund Optics. Clear optical path USAF target 38mm dia. URL `https://www.edmundoptics.com/p/clear-optical-path-usaf-target-38mm-dia/15279`.

Carl Ekdahl. Characterizing flash-radiography source spots. *J. Opt. Soc. Am. A*, 28(12): 2501–2509, 2011. doi:10.1364/JOSAA.28.002501.

M. R. Gomez, S. A. Slutz, A. B. Sefkow, D. B. Sinars, K. D. Hahn, S. B. Hansen, E. C. Harding, P. F. Knapp, P. F. Schmit, C. A. Jennings, T. J. Awe, M. Geissel, D. C. Rovang, G. A. Chandler, G. W. Cooper, M. E. Cuneo, A. J. Harvey-Thompson, M. C. Herrmann, M. H. Hess, O. Johns, D. C. Lamppa, M. R. Martin, R. D. McBride, K. J. Peterson, J. L. Porter, G. K. Robertson, G. A. Rochau, C. L. Ruiz, M. E. Savage, I. C. Smith, W. A. Stygar, and R. A. Vesey. Experimental demonstration of fusion-relevant conditions in Magnetized Liner Inertial Fusion. *Phys. Rev. Lett.*, 113:155003, 2014. doi:10.1103/PhysRevLett.113.155003.

M. R. Gomez, R. M. Gilgenbach, M. E. Cuneo, C. A. Jennings, R. D. McBride, E. M. Waisman, B. T. Hutsel, W. A. Stygar, D. V. Rose, and Y. Maron. Experimental study of current loss and plasma formation in the *Z* machine post-hole convolute. *Phys. Rev. Accel. Beams*, 20:010401, 2017. doi:10.1103/PhysRevAccelBeams.20.010401.

M. R. Gomez, S. A. Slutz, C. A. Jennings, D. J. Ampleford, M. R. Weis, C. E. Myers, D. A. Yager-Elorriaga, K. D. Hahn, S. B. Hansen, E. C. Harding, A. J. Harvey-Thompson, D. C. Lamppa, M. Mangan, P. F. Knapp, T. J. Awe, G. A. Chandler, G. W. Cooper, J. R. Fein, M. Geissel, M. E. Glinsky, W. E. Lewis, C. L. Ruiz, D. E. Ruiz, M. E. Savage, P. F. Schmit, I. C. Smith, J. D. Styron, J. L. Porter, B. Jones, T. R. Mattsson, K. J. Peterson, G. A. Rochau, and D. B. Sinars. Performance scaling in Magnetized Liner Inertial Fusion experiments. *Phys. Rev. Lett.*, 125:155002, 2020. doi:10.1103/PhysRevLett.125.155002.

Rafael C. Gonzalez and Richard E. Woods. *Digital image processing*. Prentice Hall, 3 edition, 2008.

B. L. Henke, E. M. Gullikson, and J. C. Davis. X-ray interactions: photoabsorption, scattering, transmission, and reflection at E=50-30000 eV, Z=1-92. *At. Data Nucl. Data Tables*, 54(2): 181–342, 1993. URL `https://henke.lbl.gov/`.

C. L. Hoyt. *Noncollective X-ray Thomson Scattering Diagnostic Development Based on a Titanium Hybrid X-pinch X-ray Source*. PhD thesis, Cornell University, 2015.

T. M. Hutchinson, T. J. Awe, B. S. Bauer, D. H. Dolan, J. R. Pillars, B. T. Hutsel, E. P. Yu, A. W. Klemmer, and S. E. Kreher. Photonic Doppler velocimetry of ohmically exploded aluminum surfaces. *Phys. Plasmas*, 27(5):052705, 2020. doi:10.1063/1.5140477.

B. T. Hutsel, B. S. Stoltzfus, E. W. Breden, W. E. Fowler, P. A. Jones, D. W. Justus, F. W. Long, D. J. Lucero, K. A. MacRunnels, M. G. Mazarakis, J. L. Mckenney, J. K. Moore, T. D. Mulville, J. L. Porter, M. E. Savage, and W. A. Stygar. Millimeter-gap magnetically insulated transmission line power flow experiments. In *2015 IEEE Pulsed Power Conference (PPC)*, pages 1–5, 2015. doi:10.1109/PPC.2015.7296902.

B. T. Hutsel, P. A. Corcoran, M. E. Cuneo, M. R. Gomez, M. H. Hess, D. D. Hinshelwood, C. A. Jennings, G. R. Laity, D. C. Lamppa, R. D. McBride, J. K. Moore, A. Myers, D. V. Rose, S. A. Slutz, W. A. Stygar, E. M. Waisman, D. R. Welch, and B. A. Whitney. Transmission-line-circuit model of an 85-TW, 25-MA pulsed-power accelerator. *Phys. Rev. Accel. Beams*, 21:030401, 2018. doi:10.1103/PhysRevAccelBeams.21.030401.

C. A. Jennings, J. P. Chittenden, M. E. Cuneo, W. A. Stygar, D. J. Ampleford, E. M. Waisman, M. Jones, M. E. Savage, K. R. LeChien, and T. C. Wagoner. Circuit model for driving three-dimensional resistive mhd wire array *Z*-pinch calculations. *IEEE Trans. Plasma Sci.*, 38 (4):529–539, 2010. doi:10.1109/TPS.2010.2042971.

D. H. Kalantar and D. A. Hammer. Observation of a stable dense core within an unstable coronal plasma in wire-initiated dense Z-pinch experiments. *Phys. Rev. Lett.*, 71:3806–3809, 1993. doi:10.1103/PhysRevLett.71.3806.

P. F. Knapp, M. R. Martin, D. H. Dolan, K. Cochrane, D. Dalton, J.-P. Davis, C. A. Jennings, G. P. Loisel, D. H. Romero, I. C. Smith, E. P. Yu, M. R. Weis, T. R. Mattsson, R. D. McBride, K. Peterson, J. Schwarz, and D. B. Sinars. Direct measurement of the inertial confinement time in a magnetically driven implosion. *Phys. Plasmas*, 24(4):042708, 2017. doi:10.1063/1.4981206.

S. V. Lebedev, F. N. Beg, S. N. Bland, J. P. Chittenden, A. E. Dangor, M. G. Haines, M. Zakaullah, S. A. Pikuz, T. A. Shelkovenko, and D. A. Hammer. X-ray backlighting of wire array Z-pinch implosions using X pinch. *Rev. Sci. Instr.*, 72(1):671–673, 2001. doi:10.1063/1.1315647.

M. G. Mazarakis, W. E. Fowler, K. L. LeChien, F. W. Long, M. K. Matzen, D. H. McDaniel, R. G. McKee, C. L. Olson, J. L. Porter, S. T. Rogowski, K. W. Struve, W. A. Stygar, J. R. Woodworth, A. A. Kim, V. A. Sinebryukhov, R. M. Gilgenbach, M. R. Gomez, D. M. French, Y. Y. Lau, J. C. Zier, D. M. VanDevalde, R. A. Sharpe, and K. Ward. High-current linear transformer driver development at Sandia National Laboratories. *IEEE Trans. Plasma Sci.*, 38 (4):704–713, 2010. doi:10.1109/TPS.2009.2035318.

L. Armon McPherson, David J. Ampleford, Christine A. Coverdale, Jeffrey W. Argo, Albert C. Owen, and Deanna M. Jaramillo. High energy X-ray pinhole imaging at the Z facility. *Rev. Sci. Instr.*, 87(6):063502, 2016. doi:10.1063/1.4953004.

Midwest Tungsten Service. Tungsten 3D printer M6 extruder nozzle. URL `https://midwesttungsten.com/tungsten-3d-printer-m6-extruder-nozzle/`.

John A. Mitchell. Measuring the maturity of a technology: Guidance on assigning a TRL. Technical Report SAND2007-6733, Sandia National Laboratories, 2007.

C. E. Myers, D. C. Lamppa, M. Kossow, L. M. Lucero, M. Jobe, J. K. Moore, M. R. Gomez, C. A. Jennings, P. F. Knapp, and B. Jones. Developing an inductively driven transmission line to power X-pinch radiation sources on Z. Technical Report SAND2018-10743R, Sandia National Laboratories, 2018.

S. A. Pikuz, B. A. Bryunetkin, G. V. Ivanenkov, A. R. Mingaleev, V. M. Romanova, I. Yu. Skobelev, A. Ya. Faenov, S. Ya. Khakhalin, and T. A. Shelkovenko. Radiative properties of hot dense X-pinch. *J. Quant. Spectrosc. Radiat. Transfer*, 51(1):291–302, 1994. doi:10.1016/0022-4073(94)90091-4.

S. A. Pikuz, T. A. Shelkovenko, V. M. Romanova, D. A. Hammer, A. Ya. Faenov, V. A. Dyakin, and T. A. Pikuz. High-luminosity monochromatic x-ray backlighting using an incoherent plasma source to study extremely dense plasmas (invited). *Rev. Sci. Instr.*, 68(1):740–744, 1997. doi:10.1063/1.1147689.

S. A. Pikuz, T. A. Shelkovenko, and D. A. Hammer. X-pinch. Part I. *Plasma Phys. Reports*, 41 (4):291–342, 2015a. doi:10.1134/S1063780X15040054.

S. A. Pikuz, T. A. Shelkovenko, and D. A. Hammer. X-pinch. Part II. *Plasma Phys. Reports*, 41 (6):445–491, 2015b. ISSN 1562-6938. doi:10.1134/S1063780X15060045.

T. D. Pointon. Inductance analysis of the new 9 post convolute and increased MITL gaps for Z. Memorandum, Sandia National Laboratories, 2008.

Andrew Porwitzky and Justin Brown. Uncertainties in cylindrical anode current inferences on pulsed power drivers. *Phys. Plasmas*, 25(6):063102, 2018. doi:10.1063/1.5026983.

M. E. Savage, K. R. LeChien, M. R. Lopez, B. S. Stoltzfus, W. A. Stygar, D. S. Artery, J. A. Lott, and P. A. Corcoran. Status of the Z pulsed power driver. In *2011 IEEE Pulsed Power Conference*, pages 983–990, 2011. doi:10.1109/PPC.2011.6191629.

M. S. Schollmeier, P. F. Knapp, D. J. Ampleford, E. C. Harding, C. A. Jennings, D. C. Lamppa, G. P. Loisel, M. R. Martin, G . K. Robertson, J. E. Shores, I. C. Smith, C. S. Speas, M. R. Weis, J. L. Porter, and R. D. McBride. A 7.2 keV spherical x-ray crystal backlighter for two-frame, two-color backlighting at Sandia's Z Pulsed Power Facility. *Rev. Sci. Instr.*, 88(10):103503, 2017. doi:10.1063/1.4994566.

T. A. Shelkovenko, S. A. Pikuz, D. A. Hammer, Y. S. Dimant, and A. R. Mingaleev. Evolution of the structure of the dense plasma near the cross point in exploding wire X pinches. *Phys. Plasmas*, 6(7):2840–2846, 1999. doi:10.1063/1.873241.

T. A. Shelkovenko, D. B. Sinars, S. A. Pikuz, and D. A. Hammer. Radiographic and spectroscopic studies of X-pinch plasma implosion dynamics and x-ray burst emission characteristics. *Phys. Plasmas*, 8(4):1305–1318, 2001. doi:10.1063/1.1351553.

T. A. Shelkovenko, S. A. Pikuz, J. D. Douglass, R. D. Mcbride, J. B. Greenly, and D. A. Hammer. Multiwire *X*-pinches at 1-MA current on the COBRA pulsed-power generator. *IEEE Trans. Plasma Sci.*, 34(5):2336–2341, 2006. doi:10.1109/TPS.2006.878362.

T. A. Shelkovenko, S. A. Pikuz, A. D. Cahill, P. F. Knapp, D. A. Hammer, D. B. Sinars, I. N. Tilikin, and S. N. Mishin. Hybrid X-pinch with conical electrodes. *Phys. Plasmas*, 17(11): 112707, 2010. doi:10.1063/1.3504226.

T. A. Shelkovenko, S. A. Pikuz, and D. A. Hammer. A review of projection radiography of plasma and biological objects in X-pinch radiation. *Plasma Phys. Reports*, 42(3):226–268, 2016a. ISSN 1562-6938. doi:10.1134/S1063780X16030065.

T. A. Shelkovenko, S. A. Pikuz, C. L. Hoyt, A. D. Cahill, L. Atoyan, D. A. Hammer, I. N. Tilikin, A. R. Mingaleev, V. M. Romanova, and A. V. Agafonov. A source of hard X-ray radiation based on hybrid X pinches. *Phys. Plasmas*, 23(10):103303, 2016b. doi:10.1063/1.4964771.

D. B. Sinars, S. A. Pikuz, T. A. Shelkovenko, K. M. Chandler, and D. A. Hammer. Temporal parameters of the X-pinch x-ray source. *Rev. Sci. Instr.*, 72(7):2948–2956, 2001. doi:10.1063/1.1379961.

D. B. Sinars, S. A. Pikuz, T. A. Shelkovenko, K. M. Chandler, D. A. Hammer, and J. P. Apruzese. Time-resolved spectroscopy of Al, Ti, and Mo X pinch radiation using an X-ray streak camera. *J. Quant. Spectrosc. Radiat. Transfer*, 78(1):61–83, 2003. doi:https://doi.org/10.1016/S0022-4073(02)00180-2.

D. B. Sinars, G. R. Bennett, D. F. Wenger, M. E. Cuneo, D. L. Hanson, J. L. Porter, R. G. Adams, P. K. Rambo, D. C. Rovang, and I. C. Smith. Monochromatic x-ray imaging experiments on the Sandia National Laboratories Z facility. *Rev. Sci. Instr.*, 75(10):3672–3677, 2004. doi:10.1063/1.1779607.

D. B. Sinars, S. A. Pikuz, J. D. Douglass, R. D. McBride, D. J. Ampleford, P. Knapp, K. Bell, D. Chalenksi, M. E. Cuneo, J. B. Greenly, D. A. Hammer, B. R. Kusse, A. Mingaleev, T. A. Shelkovenko, and D. F. Wenger. Bright spots in 1 MA X pinches as a function of wire number and material. *Phys. Plasmas*, 15(9):092703, 2008. doi:10.1063/1.2982496.

D. B. Sinars, R. D. McBride, S. A. Pikuz, T. A. Shelkovenko, D. F. Wenger, M. E. Cuneo, E. P. Yu, J. P. Chittenden, E. C. Harding, S. B. Hansen, B. P. Peyton, D. J. Ampleford, and C. A. Jennings. Investigation of high-temperature bright plasma X-ray sources produced in 5-MA X-pinch experiments. *Phys. Rev. Lett.*, 109:155002, 2012. doi:10.1103/PhysRevLett.109.155002.

Matthew Suggit, Giles Kimminau, James Hawreliak, Bruce Remington, Nigel Park, and Justin Wark. Nanosecond x-ray Laue diffraction apparatus suitable for laser shock compression experiments. *Rev. Sci. Instr.*, 81(8):083902, 2010. doi:10.1063/1.3455211.

Topaz DeNoise. URL `https://topazlabs.com/denoise-ai-2/`.

T. C. Wagoner, W. A. Stygar, H. C. Ives, T. L. Gilliland, R. B. Spielman, M. F. Johnson, P. G. Reynolds, J. K. Moore, R. L. Mourning, D. L. Fehl, K. E. Androlewicz, J. E. Bailey, R. S. Broyles, T. A. Dinwoodie, G. L. Donovan, M. E. Dudley, K. D. Hahn, A. A. Kim, J. R. Lee, R. J. Leeper, G. T. Leifeste, J. A. Melville, J. A. Mills, L. P. Mix, W. B. S. Moore, B. P. Peyton, J. L. Porter, G. A. Rochau, G. E. Rochau, M. E. Savage, J. F. Seamen, J. D. Serrano, A. W. Sharpe, R. W. Shoup, J. S. Slopek, C. S. Speas, K. W. Struve, D. M. Van De Valde, and R. M. Woodring. Differential-output *B*-dot and *D*-dot monitors for current and voltage measurements on a 20-MA, 3-MV pulsed-power accelerator. *Phys. Rev. ST Accel. Beams*, 11:100401, 2008. doi:10.1103/PhysRevSTAB.11.100401.

S. M. Zakharov, G. V. Ivanenkov, A. A. Kolomenskii, S. A. Pikuz, A. I. Samokhin, and J. Ullschmeid. Wire X-pinch in a high-current diode. *Sov. Tech. Phys. Lett.*, 8:456, 1982.

APPENDIX A. RETURN-POST X-PINCHES ON MYKONOS

Prior to executing the first hybrid IDXP experiments, we fielded hybrid X-pinches on Mykonos in a more traditional return-post configuration. This enabled us to connect to the long history of return-post X-pinches on 1 MA facilities [Pikuz et al., 2015a, Douglass and Hammer, 2008] and to test (1) several options for hybrid X-pinch electrodes; and (2) an initial set of X-ray diagnostics without the added complexity of an IDXP. For these experiments, we modified one of the hardware sets developed for the Mykonos electro-thermal instability (ETI) platform (see., e.g., Hutchinson et al. [2020]) so that it could accommodate a return-post X-pinch. As shown in the top left of Figure A-1, a large, configurable aluminum return can is connected to the existing ETI anode. One of the return posts is replaced with two half-posts that each hold a conical hybrid X-pinch electrode. The electrodes and the half-posts are hollowed out to allow the single hybrid

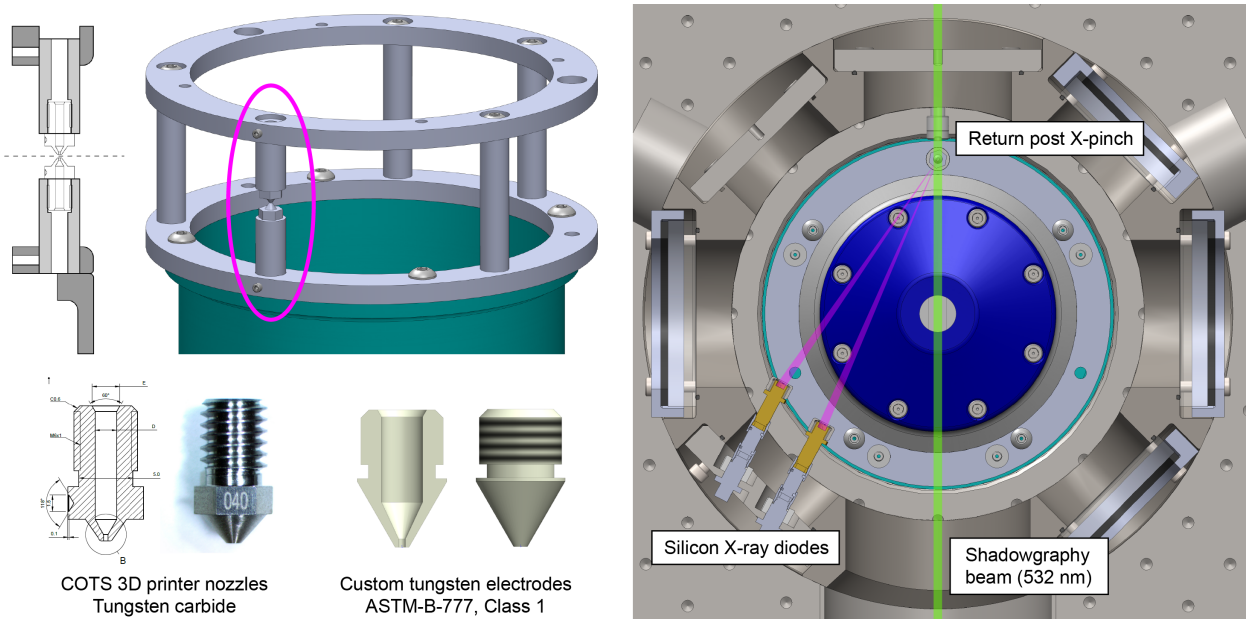

Figure A-1. *Top left: Configurable return can for the Mykonos ETI hardware that accommodates a return-post X-pinch. Bottom left: The two types of conical hybrid X-pinch electrodes that were investigated in the ETI X-pinch experiments. Right: Diagnostic suite implemented on these experiments. The core diagnostics are B-dots (not shown), shadowgraphy, and silicon diodes. Radiographic imaging (also not shown) was attempted, but the diagnostic was insufficiently developed to return data.*

X-pinch wire to pass vertically through the configuration. These experiments were typically fielded with two solid return posts and one X-pinch return post. The diagnostic configuration for these experiments is shown in the right half of Figure A-1. In addition to B-dots (not shown), shadowgraphy and silicon diodes are the core diagnostics used here. Note that the shadowgraphy beam passes through a 5/8" transverse hole in the main load, which is a 1" stainless steel rod. In total we conducted ∼20 experiments using this ETI X-pinch hardware configuration, with 16 of them containing hybrid X-pinches. The others were short-circuit null tests.

The bottom left of Figure A-1 shows the two types of conical hybrid X-pinch electrodes that were tested in the ETI X-pinch setup. The first is a commercial off-the-shelf (COTS) 3D printer nozzle from Midwest Tungsten Service (MTS). The second is a custom tungsten electrode modeled after the original Cornell design [Shelkovenko et al., 2010]. All of the electrodes used here had a 400 µm diameter central hole for the X-pinch wire. Both stainless steel and tungsten carbide versions of the MTS electrodes were tested over a series of eight Mykonos experiments. None of these experiments generated an X-pinch. The three that came closest to pinching were conducted with 35 µm molybdenum wire and tungsten carbide MTS electrodes. Figure A-2 shows single-frame shadowgraphy images from these three experiments. These images indicate that the electrode surfaces expanded dramatically during each shot. As such, we increased the initial A-K

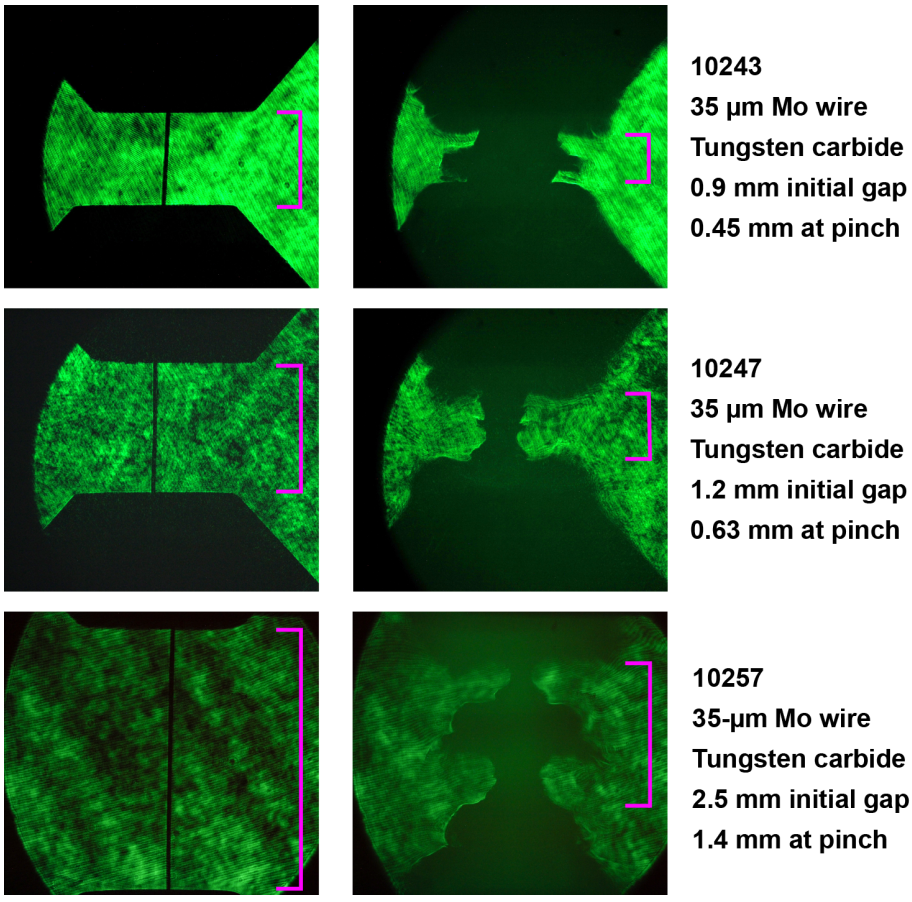

Figure A-2. *Single-frame shadowgraphy from three* 35 µm *Mo return-post X-pinch experiments that used COTS tungsten carbide MTS electrodes. Substantial electrode plasma formation is evident.*

gap from 0.9 mm to 1.2 mm to 2.5 mm. While the necking in the exploded wire is enhanced as the gap increases, none of these shots produced an X-ray burst.

At this juncture we opted to switch from the COTS MTS electrodes to the custom electrodes shown in Figure A-1, which are made from a machinable tungsten alloy (ASTM-B-777, Class 1) rather than tungsten carbide. It remains unclear why the experiments with the COTS electrodes failed to generate an X-pinch. The three most likely causes are (1) material differences between tungsten carbide and the ASTM-B-777, Class 1 tungsten alloy; (2) geometric differences between the two electrode designs; and (3) a lack of electrode conditioning. These experiments were conducted before we identified the importance of bead blasting, so it is possible that bead blasting or other electrode conditioning techniques would resolve the issues. Note that we subsequently purchased additional MTS electrodes that have the same geometry as the COTS tungsten carbide electrodes but are instead manufactured from the ASTM-B-777, Class 1 alloy. While these were not tested as part of this project, comparing the performance of these COTS-like electrodes in future experiments would decouple the material question from the geometry question.

In total, we conducted eight return-post X-pinch experiments using the custom tungsten electrodes shown in the bottom left of Figure A-1. Six of the eight experiments produced X-pinches. Only sanding was used for electrode conditioning between shots. Furthermore, the first seven of these experiments were conducted with the same set of electrodes, so it is possible that electrode conditioning from repeated use played a role here given that we saw X-pinch performance evolve over the first few shots.

A three-shot wire mass scan using 25, 30, and 35 µm Mo wire was conducted as part of the custom-electrode return-post X-pinch experiments. The mass values are listed in Table A-1 and the resulting X-ray diode traces are shown in Figure A-3. As expected, the pinch time shifts later as the mass increases. A doubling of the mass corresponds to a ∼30 ns shift in the pinch time.

Material	Diameter	Linear mass
Mo	15 µm	18 µg/cm
Mo	25 µm	50 µg/cm
Mo	30 µm	72 µg/cm
Mo	35 µm	98 µg/cm

Table A-1. *Molybdenum wire linear mass as a function of wire diameter. We include the three diameters used in the return-post X-pinch mass scan as well as the* 15 µm *diameter that was used in nearly all of the IDXP experiments.*

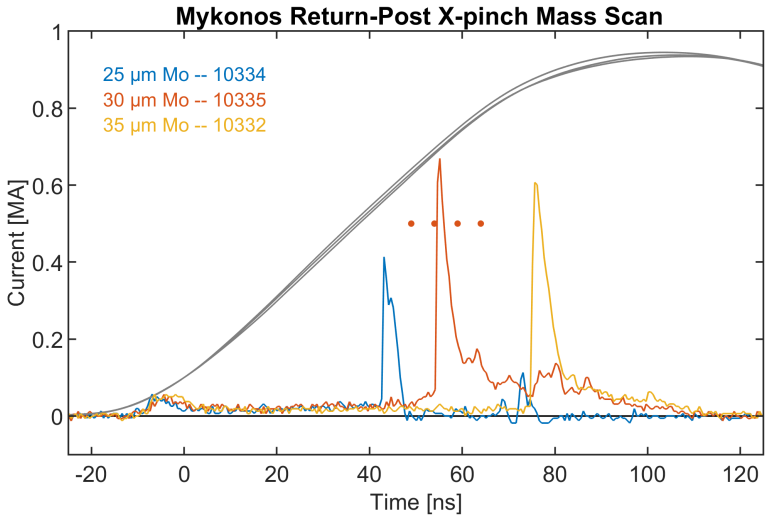

Figure A-3. *X-ray diode traces from a return-post X-pinch wire mass scan. The machine currents are shown in black, and the red dots indicate the shadowgraphy frame timing on Shot 10335.*

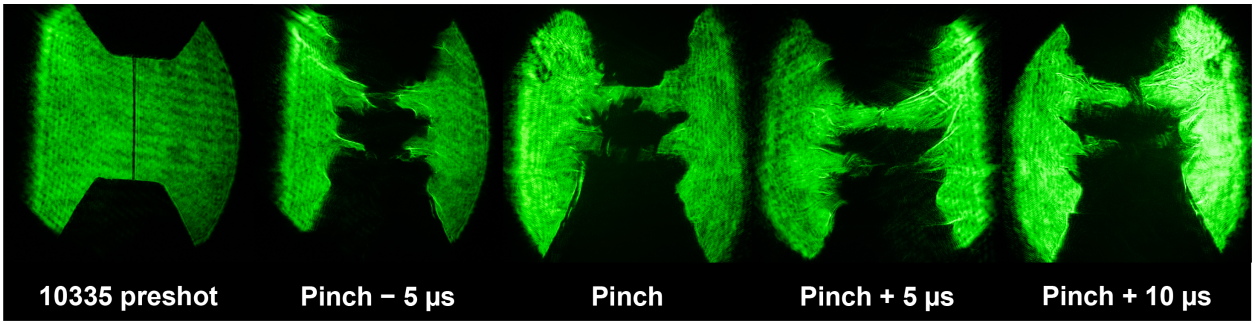

Figure A-4. *Four-frame shadowgraphy sequence from Shot 10335. The timing of the shadowgraphs relative to the X-ray emission can be seen in Figure A-3.*

Note also that the lowest mass pinch (10334, 25 μm Mo) occurs only halfway through the current pulse and exhibits what appears to be a multi-pinch behavior with the X-ray yield spread out over a broad diode pulse.

One interesting detail is that the return-post X-pinches were able to pinch ∼5 times more mass than the IDXPs, which suggests that substantially more current was delivered to the return-post X-pinch than the IDXP. Limited data from a Rogowski coil that was fielded on the return-post X-pinch (not shown) suggests that ∼300 kA of current was delivered to the X-pinch post. If the mass that can be pinched scales as the drive pressure and therefore I^2, then ∼5 times the mass corresponds to ∼2.2 times the current in the X-pinch. This gives ∼140 kA for the 15 μm wires used in the IDXPs, which is very close to the actual IDXP current.

Pinching in the custom-electrode return-post X-pinch experiments was also observed with the shadowgraphy system. Figure A-4 shows a four-frame shadowgraphy sequence captured during the pinch on Shot 10335 (see Figure A-3 for the shadowgraphy frame timing relative to the pinch). A localized gap in the wire forms at the time of the pinch. Over the subsequent 10 ns, that gap grows and then recloses as a dense tendril of plasma traverses the gap.

Given the success of the X-pinches in the return-post configuration (and the lower burden to conduct these experiments relative to IDXP experiments), it would be very interesting to revisit this platform to test whether additional electrode conditioning improves reproducibility, decrease plasma formation, and potentially permits the fielding of smaller A-K gap hybrid X-pinches. This information could then feed into future IDXP experiments on Mykonos or on Z.

We also did not devote sufficient time to developing radiographic diagnostics on the ETI X-pinch experiments. With the radiographic diagnostics that we subsequently developed on the IDXP experiments, we expect that high-quality radiographs can also be generated in the ETI X-pinch configuration with relatively little effort. This capability would be of great utility to the ETI experiments in that one could X-ray backlight an exploding aluminum barbell to observe the electro-thermal instability evolution at higher densities than has presently been done.

APPENDIX B. INDUCTIVELY DRIVEN TWO-WIRE X-PINCHES

In addition to the 21 inductively driven *hybrid* X-pinch experiments listed in Table 4-1, we also conducted two inductively driven *two-wire* X-pinch experiments during this project (10872 and 10874). Two-wire X-pinches have been studied more intensively than hybrid X-pinches [Pikuz et al., 2015a], so we attempted these shots to test whether the performance and/or reproducibility of two-wire IDXPs was superior to our hybrid IDXP experiments. In short, it was not evident that the two-wire X-pinches performed better than their hybrid counterparts. This conclusion should be caveated with the fact that we only conducted two experiments.

To accommodate two-wire X-pinches, we replaced the conical electrodes in two of the IDXP bodies (S/Ns 117 and 118) with brass electrodes similar to those sketched on the left side Figure B-1. The large upper electrode threads into a widened hole in the L-shaped lid of the IDXP, while the smaller lower electrode slides over the drive loop as before. The flat electrode surfaces are separated by 7–8 mm. The configuration is wired by threading a thick (typically

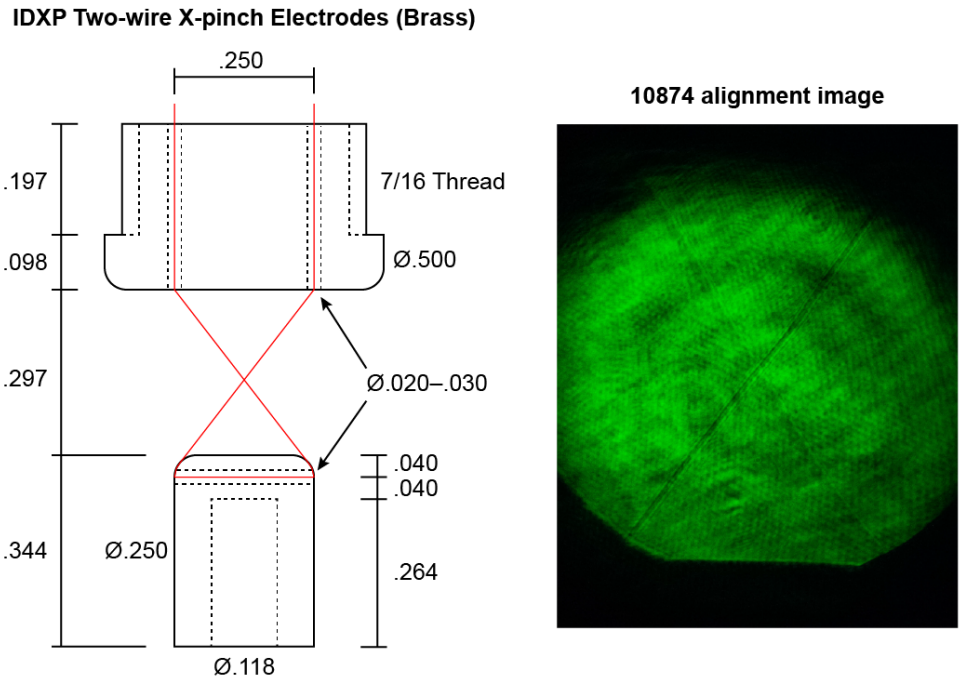

Figure B-1. *Left: Sketch of the brass electrodes used in the two inductively driven two-wire X-pinch experiments. Dimensions are in inches. Right: Pre-shot alignment image of one of the two-wire IDXPs.*

35 μm Mo) fish wire down through the left hole in the top electrode, through the transverse hole in the lower electrode and back up through the right hole in the upper electrode. The result is a U-shaped wire configuration with the lid still slightly separated from the IDXP body. Next, the thin wire that will serve as the final X-pinch wire (typically 13 μm Mo) is then tacked to the fish wire with superglue and pulled through the configuration. The thin wire is then temporarily weighted on both ends above the top electrode. Next, the lid is twisted onto the body so that the thin wire crosses over itself and forms the required X shape. Finally, the configuration is rotated to allow the temporary wire weights to pull the wires tight. The two protruding wires are taped to the outside of the IDXP body and the temporary weights are cut away. A pre-shot alignment image of one of the two-wire IDXPs is shown on the right in Figure B-1.

The linear mass in the X-pinch for the two-wire IDXPs compares to the hybrid IDXPs as follows:

$$\begin{aligned} m_{\text{hybrid}} &= \left(10.2\,\text{g/cm}^3\right) \cdot \frac{\pi}{4}\left(15\,\mu\text{m}\right)^2 \simeq 18\,\mu\text{g/cm} \\ m_{\text{2-wire}} &= \left(10.2\,\text{g/cm}^3\right) \cdot \frac{\pi}{2}\left(13\,\mu\text{m}\right)^2 \simeq 27\,\mu\text{g/cm} \end{aligned} \tag{B.1}$$

Note that while the wire in the two-wire X-pinches is thinner, the linear mass goes up because there are two wires that contribute to the linear mass. We expected that the 50% increase in linear mass would not be fatal to the two-wire IDXP experiments, and it was not.

The current coupling, X-ray diode, and resolution target data from the two two-wire IDXP experiments (10872 and 10874) are shown in Figure B-2. First, we note that these experiments fell in the range of shots where the close-in PCD was fielded, which we believe perturbed at least some of these experiments by encouraging the formation of spurious X-ray sources (see Section 4.1 for more details). The X-ray diode waveforms for the first two-wire IDXP experiment (10872) show that the two-wire configuration appeared to pinch nicely before the formation by a broad, spurious X-ray source. This spurious X-ray source is very similar to what was observed on hybrid IDXP Shot 10876 (see Figure 4-4). The fact that we saw two similar spurious X-ray sources develop in two entirely different IDXP configurations (two-wire versus hybrid) is one of the reasons we suspect that the hardware associated with the close-in PCD perturbed the experiments. The accompanying resolution target image is heavily blurred by the spurious X-ray source (see Figure B-2). Finally, the penumbral image (not shown here) hints at the generation of a sharp edge from the X-pinch, but that edge is overwhelmed by the diffuse emission from the second X-ray source.

The second two-wire IDXP experiment (10874) did not develop a spurious X-ray source, but it did generate a broader X-ray peak that likely contains multiple pinch events. This broader X-ray peak is associated with the largest inductive dip that was observed on the IDTL B-dots on Mykonos. This indicates that the inductance of the two-wire configuration evolved substantially during the pinch. Regardless, the resolution target image confirms that multiple pinches were created with at least one of them widely separated from the main emission (note the up-and-to-the-right shadows in the image). The penumbral image (not shown here) also indicates the existence of multiple widely separated, diffuse sources.

Perhaps with further testing of the two-wire IDXP configuration we could determine whether this configuration is also capable of producing backlighter-quality X-ray sources. As it stands, we

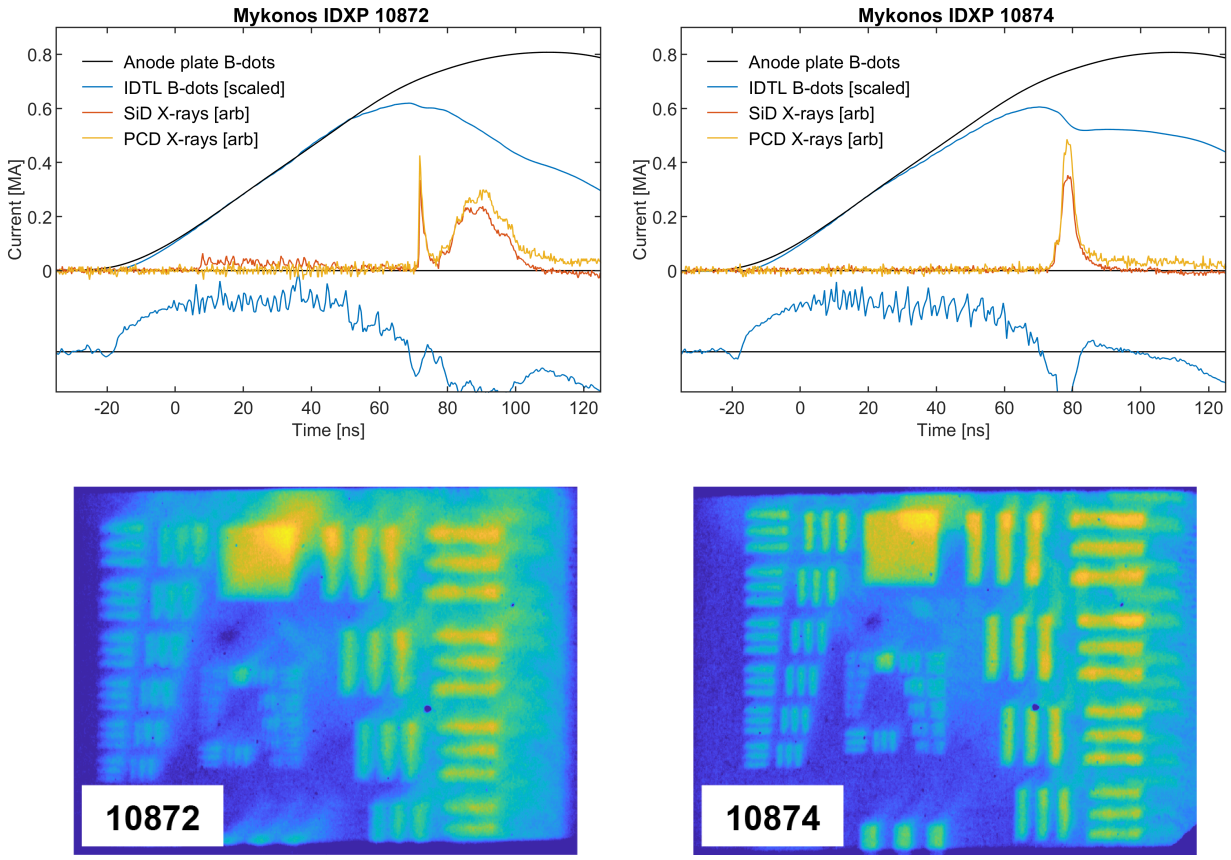

Figure B-2. *Top: Current coupling and X-ray diode data from the two two-wire IDXP experiments. Bottom: The point-projection resolution target images from these two experiments.*

only had the time to conduct two experiments, neither of which generated immediately promising results. We do not suspect that the 50% increase in linear mass was a problem in these experiments given the consistent and desirable timing of the two-wire pinches (∼72 ns). We do note that the ∼70° crossing angle of the two wires in the IDXP is larger than the ∼50° crossing angle shown, for example, in Shelkovenko et al. [2010]. While this is still within the 45–90° acceptable range identified in Pikuz et al. [2015a], this is a variable that could be explored in future two-wire IDXP experiments.

DISTRIBUTION

Hardcopy—External

Number of Copies	Name(s)	Company Name and Company Mailing Address

Hardcopy—Internal

Number of Copies	Name	Org.	Mailstop
1	D. Chavez, LDRD Office	1911	0359

Email—Internal [redacted]

Name	Org.	Sandia Email Address
Clayton E. Myers	1683	cemyers@sandia.gov
Matthew R. Gomez	1683	mrgomez@sandia.gov
Derek C. Lamppa	1659	dclampp@sandia.gov
Timothy J. Webb	1681	tjwebb@sandia.gov
David A. Yager-Elorriaga	1683	dayager@sandia.gov
Brian T.Hutsel	1651	bthutse@sandia.gov
Christopher A. Jennings	1684	cjennin@sandia.gov
Patrick F. Knapp	1683	pfknapp@sandia.gov
Michael Kossow	1692	mkossow@sandia.gov
Larry M. Lucero	1659	lmlucer@sandia.gov
Robert J. Obregon	1659	rjobreg@sandia.gov
Adam M. Steiner	1651	amstei@sandia.gov
David J. Ampleford	1683	damplef@sandia.gov
Daniel B. Sinars	1600	dbsinar@sandia.gov
Technical Library	01177	libref@sandia.gov

Sandia National Laboratories

Sandia National Laboratories is a multimission laboratory managed and operated by National Technology & Engineering Solutions of Sandia LLC, a wholly owned subsidiary of Honeywell International Inc., for the U.S. Department of Energy's National Nuclear Security Administration under contract DE-NA0003525.